Study of turbulence in a reversed field pinch plasma by microwave imaging reflectometry

Shi Zhongbing

Doctor of Philosophy

Department of Fusion Science

School of Physical Sciences

The Graduate University for Advanced Studies

2009(School Year)

I would like to dedicate this thesis to my loving parents. ...

Acknowledgements

Time flies as an arrow. Nearly three years passed. This thesis is completed as the turbulence study by MIR in TPE-RX. Here I'd like to thank all the persons who have helped me during this work.

At first, I express my deepest thanks to my advisor, Professor Yoshio Nagayama, for his guidance, encouragement and continuous patience to help my research during these three years. His physical intuition and foresight have been a constant and dependable guide throughout this entire work. Without his help, I can't finish this work. I would like to thank the opportunity to the turbulence study by MIR.

Special thanks to professor Y. Hirano, Dr. H. Koguchi, K. Yambe, H. Sakakita, S. Kiyama and others in TPE-RX group for their supports, many useful suggestions and comments for the experiments with MIR in TPE-RX.

An essential contributions of the analysis methods in chapter 4 and 5 were supported by professor Y. Hamada, and Dr. M. Clive. I thank them for the numerous fruitful discussions and helps.

I am deeply grateful to Dr. S. Yamaguchi, T. Yoshinaga, and D. Kuwahara for their helpful discussions and supports in the experiments in LHD and TPE-RX. It is pleasure to acknowledge my tutor H. Tsuchiya for his helps when I have some living troubles.

I wish to express my sincere gratitude to professor A. Fujisawa, K. Ichiguchi, K. Tanaka, T. Tukuzawa, H. Sugama, T. Ido, A. Ishizawa, V.P. Budaev, M. Skoric, H. Yamada and others for the hours they spent answering my questions.

I am deeply grateful to professor H. Sanuki, S. Sudo, and O. Motojima for their kind helps and encouragements. I wish to express my appreciation to all members of LHD experimental group, NIFS and the Graduate University for Advanced Studies (SOKENDAI) staffs for their supports.

Many people in my host institute: Southwestern Institute of Physics (SWIP) have helped and inspired me, especially professor Ding Xuantong, Liu Zetian, Yao Lianghua, Yang Qinwei, and Liu Yong. Special thanks to my Chinese boss, professor Ding Xuantong for his helps at the time I was a master-doctor student in SWIP and later in NIFS.

Finally, my family and friends have been a great source of encouragement at all times. My great thanks to my parents, my sister and my wife for their continuous supports given to me during my study in SWIP, Chengdu, China and NIFS, Toki, Japan.

Publications

★List of My Papers

1. Z. B. Shi, Y. Nagayama, S. Yamaguchi, Y. Hamada and Y. Hirano. *Data analysis techniques for microwave imaging reflectometry*. Plasma and Fusion Res. Vol.3, S1045, (2008)

2. Zhongbing Shi, Yoshio Nagayama, Daisuke Kuwahara, Tomokazu Yoshinaga, Masaharu Sugito and Soichiro Yamaguchi. *Two-dimensional numerical simulation of microwave imaging reflectometry*. To be published in J. Plasma and Fusion Res. Series, (2009)

3. Z. B. Shi, Y. Nagayama, S. Yamaguchi, D.Kuwahara, T.Yoshinaga, M. Sugito, Y. Hirano, H. Koguchi, S. Kiyama, H. Sakakita, K. Yambe and C. Michael. *Maximum entropy analysis of 2D density turbulence measured by MIR in TPE-RX*. To be published in Plasma and Fusion Res. Vol.4, (2009)

★List of My Presentations and Proceedings

1. JSPF 25th Annual Meeting, Dec. 2-5, 2008. Uchinomiya. Oral: *Two-dimensional local turbulence measured by microwave imaging reflectometry in TPE-RX*

2. 7th nuclear fusion energy conference, June 19-21, 2008. Aomori. Poster: *Turbulence near the reversed surface measured by microwave imaging reflectometry in TPE-RX*

3. The 4th Japan-Korea diagnostics seminar, Aug. 25-27, 2008, Pohang, Korea. Poster: *Observation of MHD Turbulences in RFP Plasma by microwave imaging reflectometry in TPE-RX*

4. 14th International Congress on plasma physics (ICPP2008), Sept. 8-12, 2008. Hakata, Kyushu. Poster: *Two-dimensional Numerical Simulation of microwave imaging reflectometry*

5. 18th International Toki Conference, Dec. 8-12, 2008. Toki. Poster(proceedings): *2D density turbulence measured by microwave imaging reflectometry in TPE-RX*

6. 49th Annual Meeting of the Division of Plasma Physics (APS-DPP07), Nov. 11-18, 2007. Orlando, USA. Poster: *Density Fluctuation Measurement with the Microwave Imaging Reflectometry on TPE-RX*

7. JSPF 24th Annual Meeting, Nov. 27-30, 2007. Hemeji. Poster and oral: *Microwave Imaging Reflectometry Study on TPE-RX*

8. 17th International Toki Conference, Oct. 15-19, 2007. Toki. Poster(proceedings): *Analysis of Density Fluctuation by Microwave Imaging Reflectometry*

Abstract

The physics of turbulence is a key to understand the plasma confinement. In reversed-field pinch (RFP), turbulence plays an important role to sustain the plasma configuration. However, experimental study of the turbulence is not sufficient especially around the reversed field surface. Microwave imaging reflectometry (MIR) is a powerful technique to measure the two-dimensional (2D) density turbulence localized at the cutoff surface directly.

For this purpose, the MIR system in 20 GHz with large aperture imaging optics and a 4×4 Yagi-Uda antenna array has been developed to measure the turbulence around $r_{cut}/a = 0.7 \sim 0.9$ in a large RFP device, TPE-RX. The MIR signal $Ae^{i\phi}$ is detected by the quadrature detectors, with which the amplitude A and IQ signals (cosine and sine components of the phase ϕ) of the reflection wave can be obtained. In this system, the spatial resolution is 3.7 cm and the temporal resolution is 1μs.

Since this is the first MIR system as a turbulence diagnostics, comparison between the simulation and a laboratory test of MIR system has been carried out. A numerical model based on the Huygens-Fresnel equation is used to simulate the MIR signal. Main results in this test and simulation are as follows: (1) the phase ϕ corresponds to the displacement of the cutoff surface in the radial direction; (2) the amplitude A corresponds to the reflection power, which is modulated by the shape of the cutoff surface; (3) the coherence length of the complex IQ signals is longer than that of the amplitude signals; (4) MIR is valid with the condition $4k_{\perp}dL/D < 1$ to measure the motion of the cutoff surface. Here L, D, $k_{\perp}$ and d denote distance between cutoff and lens, diameter of the lens, perpendicular wavenumber and radial displacement of the cutoff, respectively. The fluctuations measured in TPE-RX mainly distribute in the range of $4k_{\perp}dL/D < 0.8$ which suggests present MIR system can make a clear image of the cutoff surface in plasma.

In the RFP plasma, the generalized ohm's law is written as $\eta j_{\parallel} = E_{\parallel} + < \widetilde{v} \times \widetilde{B} >_{\parallel}$, where $\parallel$ denotes parallel to the magnetic field (it is poloidal at the reversal surface). In the standard plasma, the poloidal current is driven by the electromotive forces $< \widetilde{v} \times \widetilde{B} >_p$, which is produced by the fluctuations in the plasma (dynamo action). In the pulsed poloidal current drive (PPCD) plasma, the additional external field in the poloidal direction is generated and the poloidal current can be directly driven by this external electric field. As a result, the fluctuations may be suppressed with PPCD.

In this work, the developed turbulence techniques are as follows: (1) the cross correlation, (2) the wavelet, (3) the maximum entropy method (MEM), (4) the fluctuation

distributions (PDF, skewness and kurtosis), and (5) the bicoherence. By using these techniques, the turbulence in the standard and PPCD plasmas has been studied. The results are as follows:

In the standard plasma, MIR signal has many small time scale structures with $\tau < 10$ μs. The high frequency fluctuations have the features of electrostatic turbulence: (1) broad and turbulent spectrum, (2) high correlation between MIR and potential, and (3) propagation in the electron drift direction. In the PPCD plasma, the spectrum has a low frequency peak, and the high frequency fluctuations have been suppressed.

The nonlinear interaction among the toroidal modes of $n = -73, 0, 73, 146$ ($\delta n = \pm 37$) has been studied. Here $n = 146$ is the Nyquist modenumber which corresponds to the toroidal wavelength of $\lambda = 7.4$ cm. In the standard plasma, the nonlinear interaction is mainly dominated by the coupling among the modes $n = -73$, $n = 73$, and $n = 0$. The strength of the nonlinear interaction is increased as the reversal parameter F ($F = B_t(a)/ < B_t >$) is increased in the negative direction. In the PPCD plasma, the nonlinear interaction is weak as the high n modes are not observed.

The intermittency is increased as the $|F|$ is increased in the standard plasma. The intermittency of MIR signal corresponds to the bursts in the negative direction, which has small-scale structure with high fluctuation amplitude. Simulation of MIR signal suggests that the intermittency is caused by a blob-like structure, which scatters the reflection wave and leads to the rapid decrease of the reflection power. These structures enhance the transport and decrease the confinement. In the PPCD plasma, the intermittency is not observed and the confinement is improved as the soft-X-ray is increased by the factor of 100.

In conclusion, this work is the first demonstration of MIR as the turbulence diagnostics. This is the first observation of the turbulence around the field reversal surface in RFP plasma. This work demonstrates how the dynamo and intermittent structures cause bad confinement.

Contents

Chapter 1

Introduction

1.1 Introduction

In these days, turbulence is interested in many physicists as turbulence plays an important role in the plasma physics. It is considered that turbulence contributes to the anomalous transport and decreases the overall confinement in the fusion devices. Turbulence can cause self-organization phenomena such as the dynamo in reversed-field pinch (RFP) and the stiffness of the temperature profiles in magnetically confined systems. The physics of the dynamo has been studied for many years in RFP devices, such as in TPE-RX and MST. The transport barriers such as the H-mode, the internal transport barrier (ITB) and the internal diffusion barrier(IDB) have been observed in many devices, such as in LHD.

The physics of turbulence is a key to understand plasma. The turbulent plasma has many active modes which are nonlinearly coupled. These modes have random behaviors, which provide rich structures and long-range correlations. Presence of large number of modes and long-range correlations makes turbulence a very difficult problem that largely unsolved for more than hundred years.

Since the turbulence has many different structures which are always rapidly changing in spatial and temporal domains, experimental study of the turbulence should provide a relatively quick two-dimensional (2D) or three-dimensional (3D) visualization of the turbulence flow. Many 2D diagnostics for turbulence measurement have been developed

in recent two decades. Among them, microwave imaging reflectometry (MIR) has a remarkable ability to measure the 2D/3D density fluctuation localized at the cutoff surface directly [1; 2].

The reversed-field pinch (RFP) plasma provides a very good example of turbulence to study because the MHD turbulence in RFP is strong and also plays an important role to sustain the RFP configuration (dynamo activity) [3]. On the other hand, the electrostatic turbulence plays an important role in the edge transport [4]. The RFP has a MHD turbulence suppression technique: the pulsed poloidal current drive (PPCD), with which the plasma is sustained without the help of the dynamo related fluctuations [5]. The experimental study of the turbulence is not sufficient especially around the reversed field surface. Therefore, the study of turbulence between with PPCD and without PPCD operations around the reversed-field surface may clarify the physics behind RFP turbulence.

1.2 Microwave imaging reflectometry

The microwave reflectometry is a powerful tool to measure the electron density fluctuations, because of its relatively simple implementation and its high sensitivity to the behaviours of the cutoff surface. Some excellent reviews of this technique are given in references [1; 6–9] and the references herein. However, the interpretation of reflectometry data from fluctuations remains an outstanding issue, due to the effects of interference between components of the reflected waves.

In the case of small amplitude fluctuations and a one-dimensional (1D) plane stratified plasma permittivity with the first order fluctuation approximation

$$\varepsilon = \varepsilon_0(r) + \widetilde{\varepsilon}(r) \tag{1.1}$$

where $\widetilde{\varepsilon}(r) \ll \varepsilon_0(r)$, the fluctuating component of the measured phase is given by the approximation of geometric optics, as

$$\widetilde{\phi} = \int_0^{r_c} \frac{\widetilde{\varepsilon}(r)}{\sqrt{\varepsilon_0}} dr \tag{1.2}$$

and the phase fluctuation is proportional to the density fluctuation ($\widetilde{\phi} \propto L_n \widetilde{n}/n \propto \widetilde{r}_{cutoff}$) with the assumption of $k_r < k_0/(k_0 L_\varepsilon)^{1/3}$, where $L_\varepsilon = 1/(d\varepsilon_0/dr)_{r=r_c}$ and $L_n =$

$n/(dn/dr)_{r=r_c}$. ε is the plasma permittivity which is determined by the characteristic modes of propagation. In the case of the O-mode:

$$\varepsilon = 1 - \frac{\omega_{pe}^2}{\omega^2} \tag{1.3}$$

In the case of X-mode:

$$\varepsilon = 1 - \frac{\omega_{pe}^2}{\omega^2}\frac{\omega^2 - \omega_{ce}^2}{\omega^2 - \omega_{pe}^2 - \omega_{ce}^2} \tag{1.4}$$

where, $\omega_{pe} = \sqrt{4\pi n_e e^2/m_e}$ and $\omega_{ce} = |e|B/m_e$ are the plasma frequency and the electron cyclotron frequency, respectively. The cutoff frequencies of O-mode and X-mode are ω_{pe} and $\omega_r = \omega_{ce}/2 + \sqrt{\omega_{pe}^2 + \omega_{ce}^2/4}$, respectively. Figure 1.1 shows the principle of the 1D reflectometer. The phase fluctuation is dominated by the change in permittivity close to the cutoff layer, due to the factor $1/\sqrt{\varepsilon_0(r)}$ in the integral, which becomes very large near the cutoff layer. Therefore, reflectometry provides the localized fluctuation measurement directly.

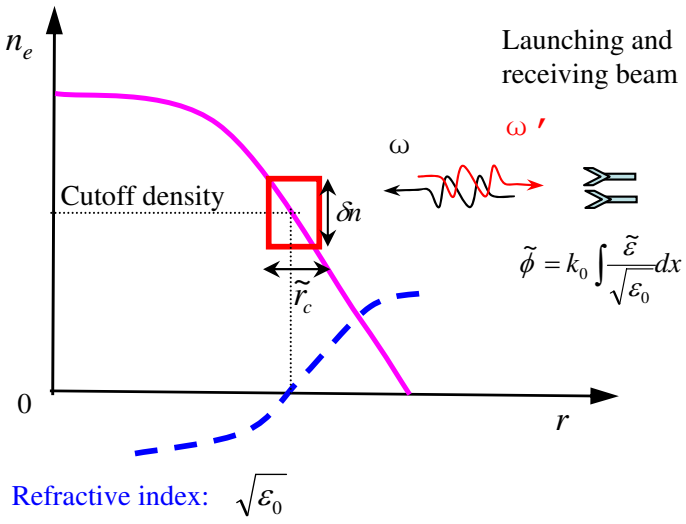

Figure 1.1: The principle of the reflectometer

However, the turbulent structures are often multi-dimensional, and exhibit rapidly variations in radial, poloidal and toroidal directions. The difference between 1D and 2D fluctuations in a standard reflectometry is illustrated in figure 1.2 [2]. In the case of 1D fluctuations, the cutoff surface moves back and forth in the radial direction, resulting in the phase changes in the reflected wave. In the case of 2D fluctuations, the backward field contains components from multiple fragmented wave fronts, resulting in a complicated

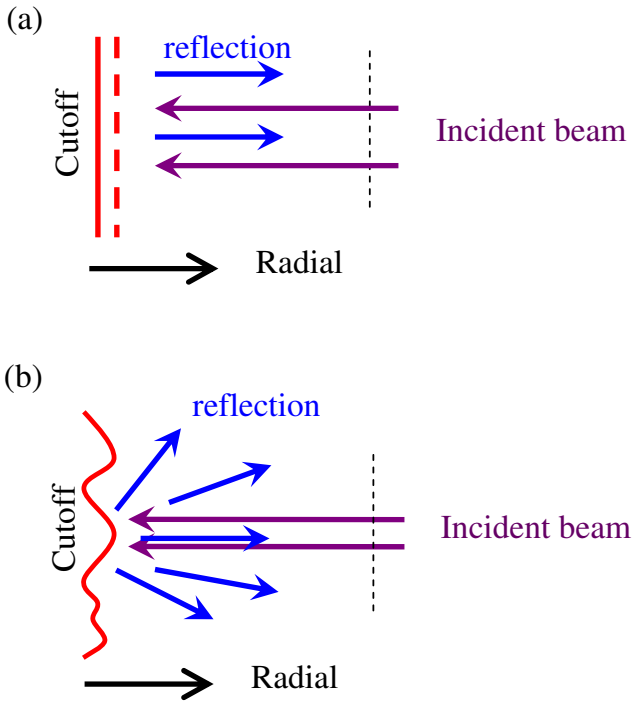

Figure 1.2: Comparison of (a) 1D and (b) 2D fluctuations in the reflectometry

interference pattern at the detector plane, and the simple relation between phase and density fluctuations is breakdown [1; 2; 10].

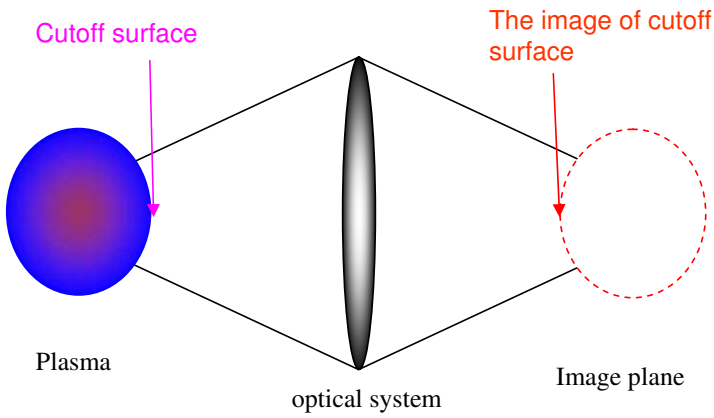

Figure 1.3: Schematic view of the MIR

To correct the disturbed wave front, the optical imaging technique can be used in the reflectometry. This so called the microwave imaging reflectometry (MIR) [1; 2]. Figure 1.3 shows the schematic view of the MIR. A wide aperture optical system is used to form an image of the reflected surface onto a 2D detector array located at the image plane. The time evolution of 2D image of the density fluctuation at the cutoff surface can be captured at the image plane, just like a movie.

The feasibilities of MIR for the turbulence measurement have been investigated in theories and experiments [1; 2; 11–14] intensively. So far, the MIR diagnostics are under development in several fusion devices, such as TEXTOR, LHD, DIII-D and ASDEX-U. Some encouraging results have been obtained in TEXTOR and LHD [11; 12]. For example, in TEXTOR, the MIR signals obtained by the phase detectors have the characteristic of a circular arc in the in-focus conditions, while the phase is filled in the complex plot in the case of out-of-focus [15]. The 2D features of edge harmonic oscillation (EHO) have been observed by using MIR with amplitude signals in LHD [16]. However, the turbulence study by using MIR has not been reported yet.

In the MIR, we obtain the signal $A\exp(i\phi)$, where A is the amplitude and ϕ is the phase. The amplitude signal is obtained by using a diode detector which has been used in many reflectometry systems because of simple technique and low costs. However,

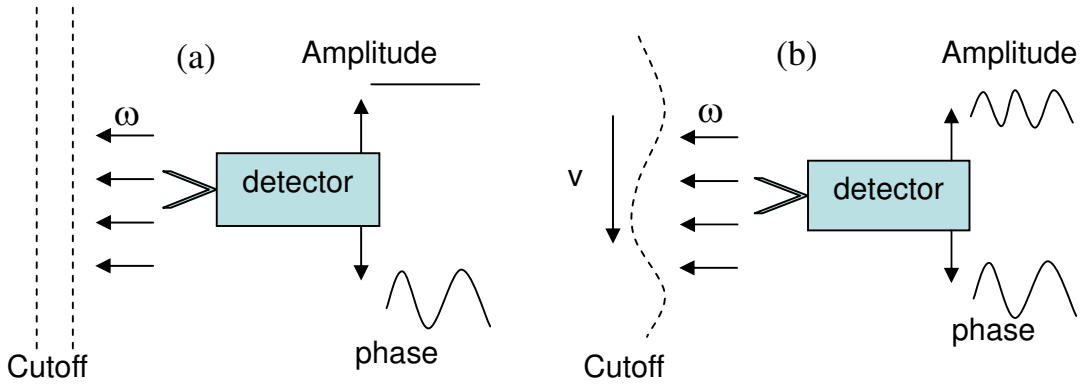

Figure 1.4: The diagrammatic view of the reflected signals in the case of (a) fluctuation in radius direction, (b) wave propagates in perpendicular direction

simulations suggest that the phase directly corresponds to the movement of the cutoff surface, not the reflected amplitude. Figure 1.4 shows the responses of the amplitude and the phase signals to the movement of the cutoff surface. The amplitude is constant if the cutoff surface only moves in the radial direction. The amplitude signal is only sensitive to the waves propagating in the perpendicular direction. The phase is measured by a quadrature detector, from which the cosine and sine components of the phase (I and Q signals) can be obtained (Note: phase measurement is complicated than the amplitude). The phase is $\phi = \arctan(Q/I)$. Therefore, we can have six signals, as: A, I, Q, $I + iQ$, $A(I + iQ)$, and ϕ. Interpretations of these data are hard. Different experiments and simulations may have different conclusions. Mazzucato [1] and Rhodes [17] prefer the amplitude signals, while Conway [18] and Schirmer [19] prefer the complex phase signals.

1.3 Features of reversed field pinch

Reversed field pinch (RFP) is one of the toroidal magnetic confinement systems for plasmas. Several reviews have been published [3; 20; 21]. RFP is characterized by the reversed toroidal magnetic field outside the reversal radius in respect to the direction inside of it ($B_\varphi(a) < 0$). The reversed field is maintained by driving the plasma current I_p, through the so called dynamo effect. The magnitude of the maximum poloidal

magnetic field is comparable to that of the toroidal magnetic field ($B_\theta \approx B_\varphi$). The pitch of the magnetic field lines gradually changes from the magnetic axis toward the plasma boundary without having a pitch minimum, which is favorable to confine relatively high beta (β) plasma with normal conducting toroidal coils.

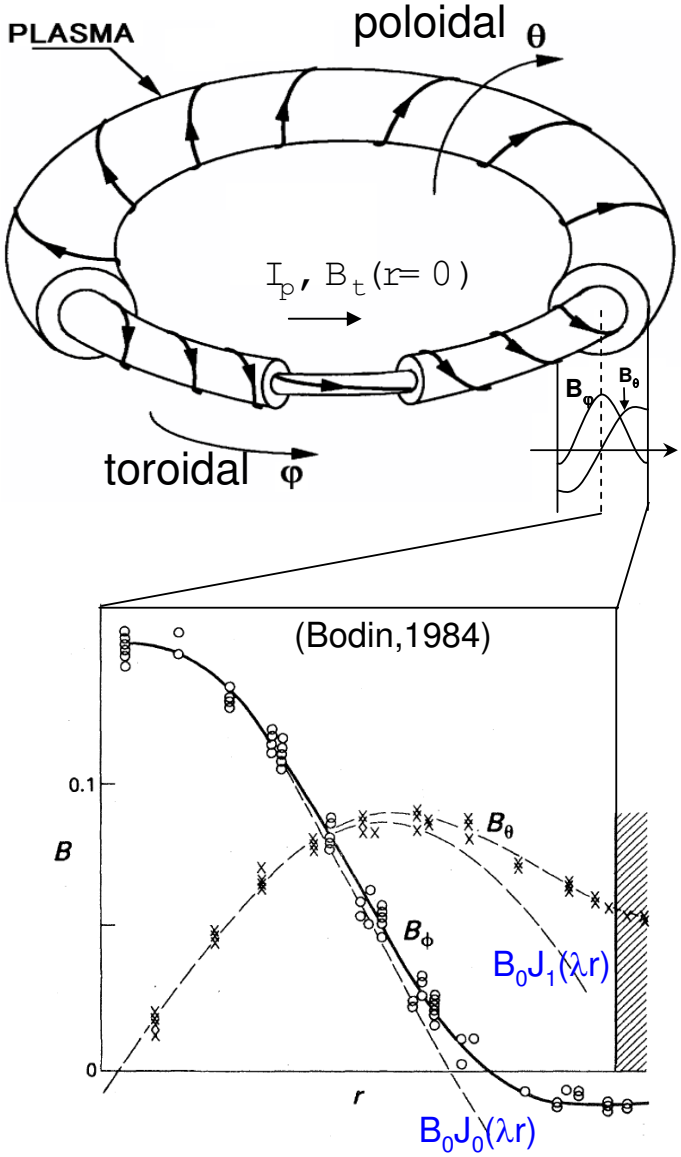

Figure 1.5: The magnetic field profiles in a RFP configuration

The reversed field is generated naturally, as a result of relaxation process. The relaxation of a plasma with small but finite resistivity is considered, and the final relaxed state (or Taylor state) is obtained by minimizing the magnetic energy with respect to

the single constraint that the total magnetic helicity

$$K_0 = \int_V \overrightarrow{A} \cdot \overrightarrow{B} d\tau \tag{1.5}$$

is invariant. The vector potential $\overrightarrow{A}$ is given by $\overrightarrow{B} = \nabla \times \overrightarrow{A}$, and the integral is taken over the whole volume of the system. Phyiscally, helicity is a linkage of flux. The relaxed stated equilibrium for a system which conserves the toroidal flux Φ is given by

$$\nabla \times \overrightarrow{B} = \mu \overrightarrow{B} \tag{1.6}$$

where μ is constant in space. For a large aspect ratio torus of circular cross-section the solution to this equation is given by the Bessel function.

$$B_r = 0, \qquad B_\theta = B_0 J_1(\mu r), \qquad B_\varphi = B_0 J_0(\mu r) \tag{1.7}$$

Figure 1.5 shows the typical magnetic field profiles in the RFP configuration. The measured magnetic field profiles agree well with the theory [3; 22]. There is a small discrepancy in the outer region as μ decreases towards the wall and is not constant in the experiments. The modified Bessel function model has been developed with the assumption of $\mu = \mu_0(1 - (r/a)^\alpha)$, where μ_0 is the value on the axis, and α can be fitted to the measured profiles [23].

The solution of equation 1.7 includes a constraint condition. That is, μ and the minor radius a of the flux conserving boundary are related to the pinch parameter Θ. It is given as:

$$\Theta = \frac{B_\theta(a)}{< B_\varphi >} \tag{1.8}$$

The reversal parameter F is defined as

$$F = \frac{B_\varphi(a)}{< B_\varphi >} \tag{1.9}$$

It possesses field reversal in the case of $F < 0$. In general, the high Θ corresponds to the deep F.

Both the reversal parameter F and the pinch parameter Θ are used to describe the features of RFP plasmas, such as the field reversal and fluctuations. Experiments and simulations suggest the field reversal when Θ exceeds 1.2 [23] (or when $F < 0$). The fluctuation becomes more coherent and the magnetic fluctuation amplitude is increased as the Θ is increased [24].

1.4 Standard and PPCD plasmas in RFP

In RFP, the duration of the plasma is much longer than the classical magnetic field diffusion time, because the dynamo sustains the RFP configuration and governs the transport in the standard RFP operation (without additional current drive such as PPCD) [3; 25]. One of the important issues relating to RFP plasma is the underlying physics of dynamo activity. This problem has been studied for several decades, and it is believed that the dynamo activity is driven by instabilities and turbulences [22; 26–29]. The nonlinear MHD theory applied to the standard RFP plasma predicts the turbulent structures in the dynamo actions arising from spatial fluctuations in the flow ($\widetilde{v}$) and magnetic fields ($\widetilde{B}$). These fluctuations form an equilibrium electromotive force $E_M \parallel = < \widetilde{v} \times \widetilde{B} >_{\parallel}$, where $\parallel$ denotes parallel to the magnetic field (it is mainly poloidal at the edge region), $<>$ denotes the average over an equilibrium flux surface. The electromotive force $E_M \parallel$ can drive the poloidal plasma current, which generates the reversed toroidal field. As a result, the plasma configuration is sustained by the electromotive force. Here we define the plasma sustained by the $E_M \parallel$ as the standard plasma.

However, these fluctuations (in dynamo action) may cause strong particle and energy transport in plasma. It is difficult to improve the plasma confinement in the standard operation. It is reported that more than 90% of the RFP magnetic fluctuations are dominated by the core-resonant tearing (or resistive kink) instabilities with the poloidal mode number of $m = 1$ and several toroidal mode numbers of $n \sim 2R/a$ [23]. Since the tearing fluctuation is driven by the current density gradient, the current drive in the outer region of the plasma can change the current profile. This eliminates the magnetic fluctuation and improves the confinement. So far, the current drives, such as the electrostatic poloidal current drive (EPCD), the RF poloidal current drive (RFCD), the lower-hybrid current drive (LHCD) and the pulsed poloidal current drive (PPCD) have been demonstrated in MST and other RFP devices [5; 30; 31]. Among them, PPCD is the widely used one.

In the PPCD operation, an external poloidal electric field is generated. Since the magnetic field is mostly poloidally directed in the outer region of the plasma, the external electric field generated by PPCD is parallel to the edge magnetic field. The parallel mean-field Ohm's law include the electromotive force should be written as [32]

$$\eta j_{\parallel} = E_{\parallel} + E_{M\parallel} \tag{1.10}$$

where, η is the electric resistivity. $j_{\parallel}$ is the parallel equilibrium current, $\tilde{v}$, $\tilde{B}$ are the fluctuating fluid velocity and magnetic field, respectively. <> denotes the average over an equilibrium flux surface. $E_{\parallel}$ and $E_{M\parallel}$ are the external electric field and the electromotive force parallel to the magnetic field, respectively. Since the external electric field $E_{\parallel}$ can drive the poloidal current, the plasma configuration can be sustained without the help of dynamo ($E_{M\parallel}$) in the PPCD operation.

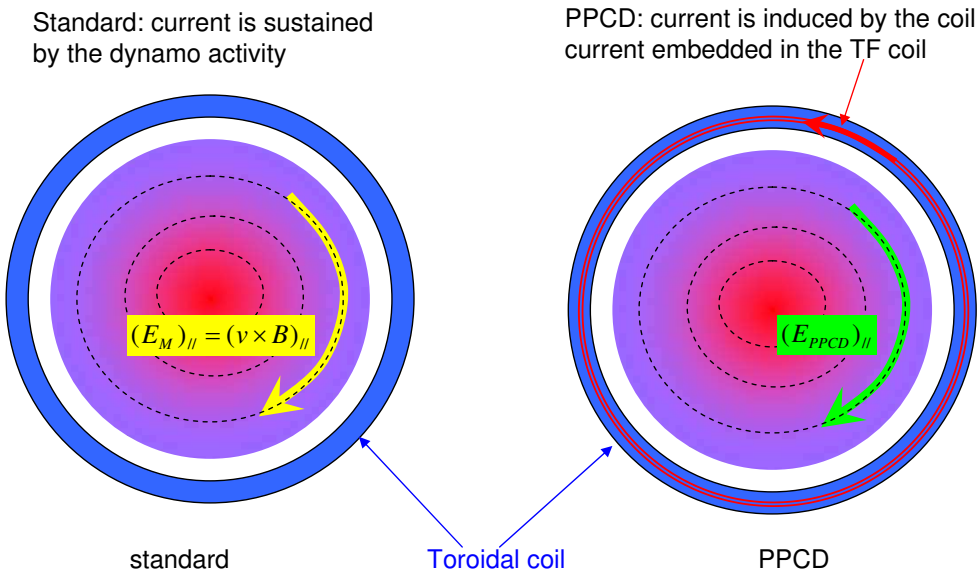

Figure 1.6: The operations of the standard and the PPCD

Figure 1.6 shows the comparison of the operations in the standard and the PPCD plasmas. In the standard plasma, the poloidal current is driven by the parallel electromotive force $E_{M\parallel}$, which may be as a consequence of the nonlinear interaction between MHD fluctuations. In the PPCD plasma, the external electric field is generated by the current in the coil embedded in the toroidal field (TF) coil. This external electric field can drive the poloidal current, so that the reversal field can be sustained without the help of the electromotive force driven by fluctuations. As a result, the turbulence may be suppressed in the PPCD operation. The details of the waveforms in the PPCD and the standard plasmas are explained in chapter 2.

Experiments with PPCD operation have been performed in MST, TPE-RX and RFX [5; 30; 31]. The reductions of the magnetic fluctuations and transport coefficient have been observed [30]. About ten-fold improvement of the confinement time has been

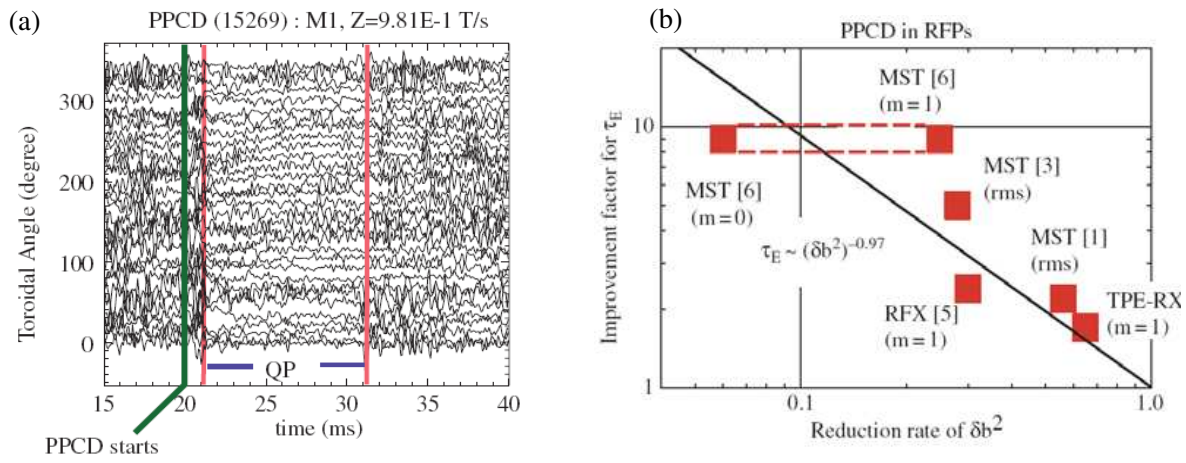

Figure 1.7: (a) Magnetic fluctuation (dB_r/dt) in the PPCD plasma in TPE-RX, (b) Improvement factor of τ_E versus reduction rata of δb^2 in the PPCD experiments.

obtained in MST [33]. An example of the reductions of the magnetic fluctuations and the improvement of the confinement in the PPCD operation are shown in figure 1.7.

1.5 Review of turbulence in RFP

The RFP configuration relies on currents flowing in the plasma for the generation of both toroidal and poloidal components of the magnetic field. A highly sheared magnetic configuration can be obtained. The RFP stability theory gives the q profile which differs significantly from that of tokamaks. Figure 1.8 shows the schematic view of q profiles and possible resonances in RFP. The q value monotonically decreases from the center value (typically $q(0) \sim 0.1$). It becomes negative in the edge region. In general, the $m = 1$ modes are the most unstable ones. Hence there are many potentially unstable modes $(m, n) = (1, n)$ with resonant surfaces in the central part of the plasma. The radial density of resonances is increased with the radius. The high n modes are rather densely packed near reversal surface. This configuration may be unstable with respect to neighboring modes corresponding to smaller or larger toroidal mode numbers n.

Various candidates for the RFP instabilities have been discussed: tearing instabilities, pressure-driven g-modes and drift-wave turbulence [34–38]. The reviews of these theories

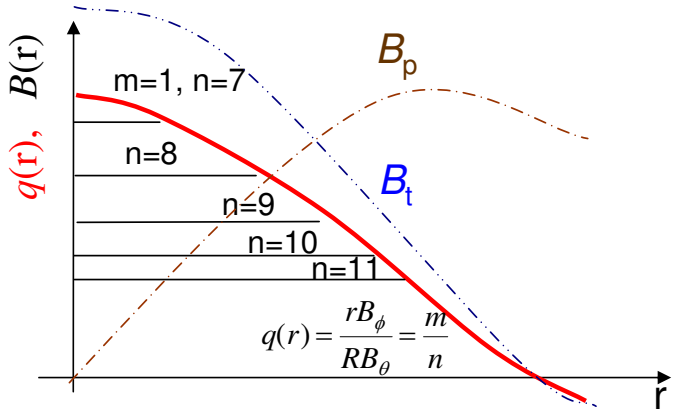

Figure 1.8: Schematic view of q profiles and possible resonances ($m = 1$ modes) in RFP.

are as follows.

The current driven tearing instability may occur in any sheared magnetic configuration [34]. The growth rate of the tearing mode is as a function of Δ', as

$$\gamma \simeq \eta^{3/5}(\Delta')^{4/5}(kB_0')^{2/5} \tag{1.11}$$

where, $\Delta' = \lim_{\delta\to 0}[\psi_1'(x_s+\delta) - \psi_1'(x_s-\delta)]/\psi_1(x_s)$, $\psi(x_s)$ is the magnetic flux function at the resonance surface, given by $\mathbf{B}_\perp = \mathbf{e}_z \times \nabla\psi$. In the framework of incompressible MHD, tearing mode is unstable only if $\Delta' > 0$.

In the case of plane sheet pinch, Δ' can be simplified as

$$\Delta' = \frac{2}{a}(\frac{1}{ka} - ka) \tag{1.12}$$

The tearing mode is unstable ($\Delta' > 0$) for the long wavelength $ka < 1$, and stable ($\Delta' < 0$) for the short wavelength $ka > 1$.

A more general analysis gives a maximum growth rate $\gamma_{max}(k) \sim \eta^{1/2}$ at $k \sim \eta^{1/4}$. For still smaller k, decreases again. Therefore, the tearing instability is limited to low mode number [35].

In the RFP, q decreases with radius. The low n modes with $n \sim 1/q_{max}$ which have the resonances close to the axis are most unstable, while high n modes with resonances close to the field reversal radius are stable. High mode numbers are primarily driven by the plasma pressure gradient instead of the parallel current [34].

The pressure driven modes are generalizations of the Rayleigh-Taylor process. These modes are also called interchange modes, since they correspond simply to an interchange of the positions of neighboring flux tubes together with their plasma content.

The growth rate of the ideal pressure driven modes is given by

$$\gamma = (\frac{g\rho_0'}{\rho_0}\frac{k_\perp^2}{k^2})^{1/2} \simeq (\frac{g}{L_\rho})^{1/2} \tag{1.13}$$

where, $L_\rho = \rho_0/\rho_0'$ is the density scale length. $k_\perp$ is the wave vector component perpendicular to the gravity g. The growth rate is largest for small-scale modes $kL_\rho \gg 1$.

If we consider the effect of finite resistivity, the dispersion relation of the interchange instabilities is changed as

$$\gamma^2 \simeq \frac{2\kappa p_0'}{\rho_0} - \frac{k_\parallel^2 \upsilon_A^2}{1+\eta k_\perp^2/\gamma} \tag{1.14}$$

where, $\kappa = -r(1-q^2)/(R^2q^2)$ is the cylindrical curvature. If the average curvature $\overline{\kappa} > 0$, there are always unstable modes. In the case of RFP, $|q| \ll 1$, the the pressure-driven interchange modes are always destabilizing.

Since the growth rate of interchange instabilities is increased with wavenumber, the magnetic perturbation $\psi_1 = \mathbf{B}_0\cdot\nabla\phi/(\gamma+\eta k_\perp^2)$ becomes small as wavenumber is increased. Contrary to the long-wavelength tearing modes, the small-scale pressure-driven modes has $\mathbf{B}_0 \cdot \nabla\phi + \eta j_1 \simeq 0$, which means that the magnetic perturbation ψ_1 produced by the current j_1 can be neglected. Therefore, the small-scale pressure-driven modes are dominated by the electrostatic fluctuations.

Figure 1.9 shows the growth rates of the tearing and interchange instabilities as a function of the wavenumber k with the assumptions of $D_s \sim 1.0$, $S = 10^6$ [35]. It gives the k spectrum of the growth rate of all pressure-driven modes transiting from tearing parity modes to interchange parity modes as k increases. Since, the growth rate at high k modes is stabilized by the finite Larmor radius effects, the global low k pressure-driven modes may be more important for the RFP plasma.

The quasi-linear theory of MHD dynamics suggests the nonlinear interactions (mode to mode to coupling) which is shown in figure 1.10 [23; 36]. Consider two $m = 1$ modes, $(1, n)$ and $(1, n+1)$ with neighboring values of n, where mode interaction is expected to be strong. Two types of coupling processes can be distinguished. Exciting the linearly stable $(2, 2n+1)$ mode implies the generation of smaller spatial scales, since such modes are rather strongly localized radially. This process corresponds to the direct turbulent

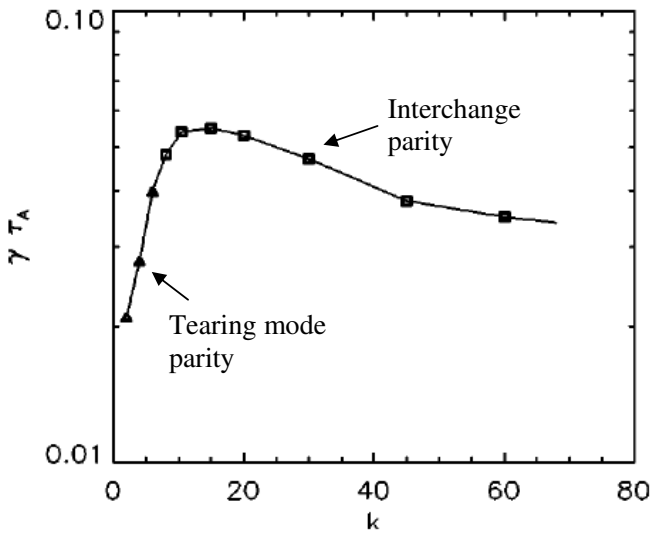

Figure 1.9: The growth rate as a function of wavenumber of ideal pressure-driven modes at $D_s \sim 1.0$, $S = 10^6$. Triangles denote modes with a radial structure with tearing mode parity; box denote interchange parity

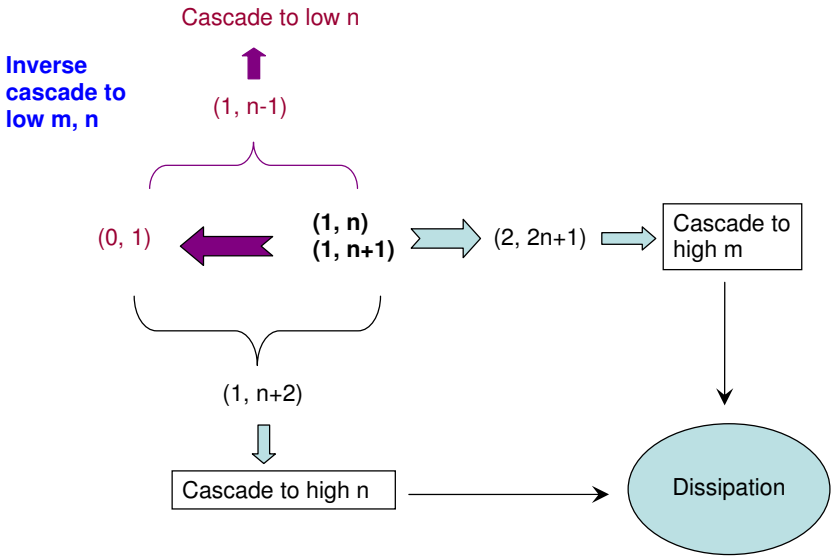

Figure 1.10: Diagram of the mode to mode coupling

energy cascade to small dissipative scales. By contrast the coupling to the stable, $(0,1)$ mode is non-dissipative since this mode has a global radial distribution. By further coupling to the $(1,n+2)$ and the $(1,n-1)$ modes this process leads to a broadening of the n-spectrum of the $m=1$ modes. The couplings to the $m=0$ modes are either direct interactions of the different $m=1$ modes with the $(0,0)$ components or $(0,n)$ modes which are particularly important for the dynamo effect since they are all resonant at the field reversal point.

It should be noted that both the tearing and interchange instabilities only have the purely growing. They don't have the real eigenfrequency. The drift waves have the complex frequency $\omega = \omega_r + i\gamma$, with $\gamma \ll \omega_r$ usually.

The drift wave instabilities occur in a plasma of non-uniform density maintained in equilibrium by a strong and essentially straight magnetic field. The dispersion relation of the drift waves is given by [39]

$$\omega^2 - \omega_* \omega - k_\parallel^2 C_s^2 = 0 \tag{1.15}$$

where, $\omega_* = -k_\perp \kappa T_e/(eB_0 L_n)$ is the diamagnetic frequency, $L_n = n_e/n_e'$ is the density gradient length, $C_s = (T_e/m_i)^{1/2}$ is the velocity of ion sound wave.

The growth rate of the drift wave is given by

$$\gamma = \frac{\eta k_\perp^2}{\mu_0} \frac{\omega^2(\omega^2 - k_z^2 C_s^2)}{k_z^2 v_A^2 (\omega^2 + k_z^2 C_s^2)} \tag{1.16}$$

The drift wave is unstable when $|\omega| > |k_z C_s|$. There are two branches of the drift waves: electron branch and ion branch (see Fig. 1.11). Experimentally, we are usually interested in the electron drift wave in the limit of $\omega_* \gg k_z C_s$. The electron drift wave has the frequency of

$$\omega \approx \omega_* \tag{1.17}$$

and the drift wave propagates in the electron drift direction.

Experimental studies of the turbulence in the RFP plasmas have been performed by magnetic probes, electrostatic probes, spectroscopy, reflectometer, heavy ion beam probe (HIBP) and Gas-puff imaging (GPI), which view the plasma fluctuations from the core to edge region [25; 29; 40–45]. Since the magnetic fluctuation is very strong in the RFP plasmas ($\sim 1\%$, it is about $10 \sim 100$ times higher than that in tokamaks), two main interpretations of the RFP turbulence have been suggested: the MHD turbulence

	Magnetic instability	**Electrostatic instability**
Core region (r/a<0.7)	•Low n tearing modes •Around m=1, n=2*R*/*a* [Biskamp,1993]	•Weak electrostatic turbulence [HIBP, Lei, PRL2002, Ji, RPL1991]
Around reversal surface	• m=0 and high (m=1) n tearing modes	• Electrostatic
Edge region (0.85<r/a<1.1)	• High n tearing modes (very weak, may not be measured)	• Strong electrostatic [Antoni, PRL1998]
Instabilities	• Resistive g-modes [Sarff,IAEA1994] • Tearing instabilitiy: current driven • Interchange instability: pressured driven [Agostini, PPCF2008]	• Electrostatic turbulence [Antoni, PRL1998; Rempel, PRL1991] • Drift wave turbulence [Antoni, PPCF1997]
Features of fluctuations	• Narrow spectral profile, • The modes are dominated by the m=1, 0 modes. • The fluctuation power is rapidly decreased as the mode number is increased. • Low frequency (f < 100 kHz)	• Broad spectral profile • High frequency (f > 100 kHz) [Li, EPS1994, Li, POP1995].
Nolinear interaction	• **Core**: low n tearing modes coupling. [Assadi, PRL1992] • **Edge**: high n tearing modes coupling. [Bunting, EPS1977] • Magnetic reconnection and MHD turbulence [Rusbridge, Plasma Phys.1977]	• Strong edge electrostatic turbulence • Correlation between magnetic and electrostatic fluctuations: (1) **Strong**, Tsui NF1992, Brunsell, POP1994, Li, POP1995. (2) **Weak**: Rempel,PRL1991, Ji, RPL1991
Diagnostics	• Magnetic probes (r/a~1.0) • Complex edge probe (r/a~1.05)	• Langmuir probes (r/a~1.0) • GPI (r/a=0.95~1.0) • HIBP (r/a=0.2~0.7) • Spectroscopy • Reflectometer (r/a~0.95)

Table 1.1: Review of fluctuations in RFP.

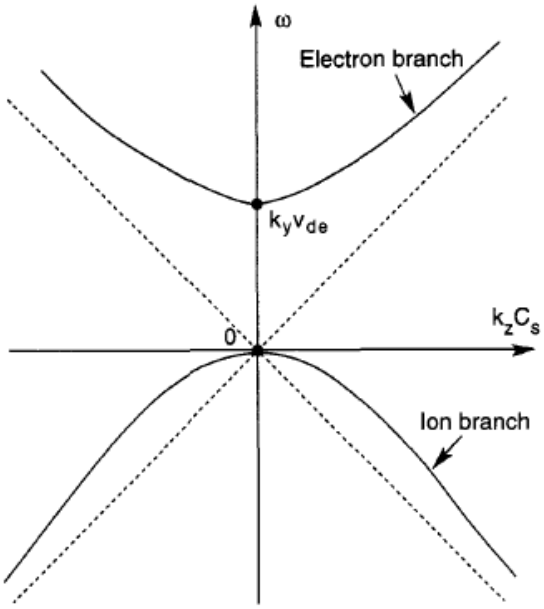

Figure 1.11: Electron and ion branches of the drift-wave dispersion relation. Both branches approach asymtotes $\omega = \pm k_z C_s$

and the electrostatic turbulence. Both these interpretations have experimental data supporting them.

The summary of the fluctuations in RFP plasmas studied by experiments and simulations is shown in table 1.1. The fluctuations in the core region and the edge region have been experimentally studied by HIBP, GPI, magnetic probes and electrostatic probes in RFP. These results suggest the MHD instabilities ($m = 1$, low n tearing modes) are dominant in the core region. Around the reversal surface, there are many densely packed high n tearing modes ($m = 1$) and the resonance surface of the $m = 0$ tearing modes. In the edge region, the results obtained by electrostatic probes and reflectometer suggest that the electrostatic fluctuations can account for significant particle losses [46; 47].

The features of electrostatic fluctuations exhibit broad band features with $\Delta f/f \sim 1$, $\Delta k_\perp/k_\perp \sim 1$ and a wide spectrum of toroidal and poloidal periodicity numbers [48]. The observed mode number spectrum of the electrostatic turbulence ($\Delta n \sim 150$) is about two times wider than that of magnetic fluctuation ($\Delta n \sim 60$) in MST [46]. The observed frequency ranges of the electrostatic fluctuation are high (typically $f > 100$ kHz) and broad [42].

So far, the study of the turbulence in RFP plasma is lack of experiment, especially the turbulence around the reversed-field surface due to the inaccessibility of the diagnostics and the complicated fluctuations (high magnetic and electrostatic fluctuations, as a result, some approximations in MHD theory may be violated). These fluctuations may highly interact with each other, lead to a very difficult problem. Nevertheless, the study of the fluctuations near the reversal surface may be very important to clarify the turbulence physics in RFP.

1.6 Object of this work

The RFP turbulence in the core region and edge region has been studied by magnetic probes, electrostatic probes, GPI and HIBP. However, around the reversed-field surface, the turbulence has not been well understood until now (see table 1.1). This work presents the first turbulence measurement around the reversed field surface in the RFP plasma in TPE-RX. This measurement is established by using MIR because MIR is the local measurement of the electron density fluctuation. It aims to contribute to a better understanding of the RFP turbulence, as well as the development of MIR system and turbulence analysis techniques.

For this purpose, the MIR system with the microwave frequency of 20 GHz (O-mode, the cutoff density is 0.51019 m-3) and the large aperture imaging optics has been developed for the experiments in a large RFP device TPE-RX ($R = 1.72$ m, $a = 0.45$ m). By using MIR system, the 2D (4×4) image of density fluctuations have been observed in the region of $r_{cut} = 0.7 \sim 0.9$. In this system, the toroidal and poloidal spatial resolutions are 3.7 cm, and the temporal resolution is 1μs. However, interpretation of the MIR signal is still an important issue. In order to investigate the principles of MIR measurement, a 2D simulation model based on Huygens-Fresnel equation is developed to simulate the MIR signal. The simulation and the test results are compared, and a valid clear image condition is obtained. The turbulence in the plasmas with and without PPCD has been compared by various analysis techniques, which have been developed in this work. The features of RFP turbulence around the reversed field surface have been clarified.

1.7 Structures of this work

This work is organized as follows: Chapter 2 contains a description of the experiments with MIR in TPE-RX RFP. The features of MIR signals are presented. In chapter 3, a 2D numerical simulation model has been developed to simulate the MIR signal. The simulation agrees well with the laboratory test when the displacement of the cutoff surface in radial direction is much smaller than the wavelength of the launching wave. MIR is valid with the condition $4kdL/D < 1$ to measure the fluctuation. Some turbulence analysis techniques, such as cross-correlation analysis, wavelet analysis and maximum entropy method (MEM), are described in chapter 4 and 5. The features of these analysis techniques have been discussed. In chapter 6, we clarify the characteristics of the RFP turbulence by using MIR diagnostics. PPCD suppresses the $m = 0$ tearing modes and electrostatic-like turbulence. Without PPCD operation, the plasma has characteristic of high intermittency and high nonlinear interaction among the magnetic and electrostatic-like fluctuations at deep F. Simulation of MIR signal suggests the intermittency is caused by the blob structure, which enhances the transport and decreases the confinement. The conclusion and discussion are given in the chapter 7.

Chapter 2

The Experiments in TPE-RX

2.1 TPE-RX reversed-field pinch

TPE-RX is one of the largest reversed-field pinch (RFP) devices in the world. This is in the National Institute of Advanced Industrial Science and Technology (AIST), Tsukuba, Japan. The major radius is $R = 1.72$ m and minor radius is $a = 0.45$ m [30; 49] (see figure 2.1). It is characterized by a multilayered shell system in a conductive all-metallic vacuum vessel which provides relatively high I_p/N values (10^{-19}Am; $N = \pi a^2 < n_e >$, the number of electron per unit toroidal length, derived using the line-averaged electron density $< n_e >$). The plasma equilibrium is provided by thick aluminum shell with the thickness of 50 mm . A thin copper shell, which has two layers with the thickness of 0.8 mm each, effectively stabilizes the fast growing MHD modes in an order of millisecond by its close distance to the plasma surface. The all-metal first wall (vacuum chamber) also provides MHD mode stabilization and the fast equilibrium control in a short time scale less than millisecond. TPE-RX can operate in the standard (normal or without PPCD) and with the pulsed poloidal current drive (PPCD). To improve the energy confinement time, a six-pulsed PPCD operation has been developed in TPE-RX [50]. The confinement time has been improved by order of magnitude [51]. In general, PPCD operation starts at 18 ms and ends at 35 ms. The duration time of the standard plasma is about 100 ms and the duration time of the PPCD plasma is about 35 ms.

Several diagnostics are used in the experiments besides the microwave imaging re-

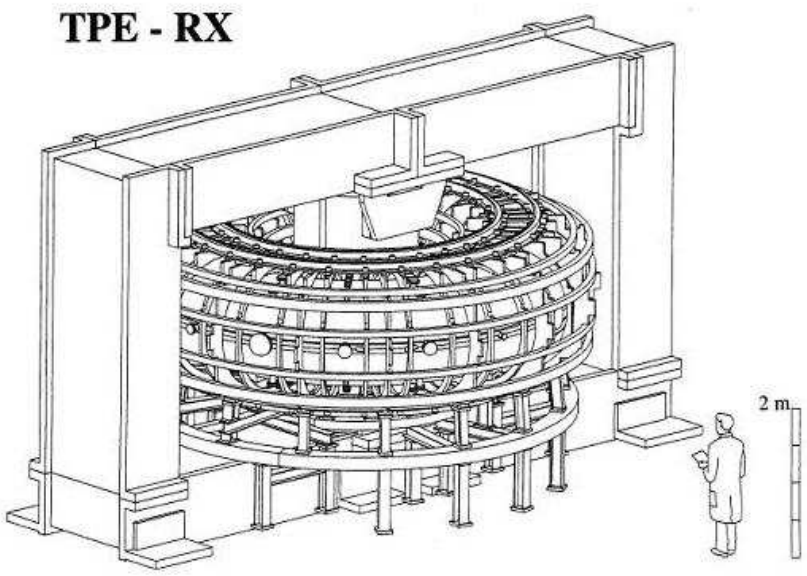

Figure 2.1: Overview of TPE-RX

flectometry (MIR). The plasma density is measured by a dual-chord interferometer [52]. One channel views the plasma center ($r/a = 0$) and the other channel views the normalized radius $r/a = 0.69$. The soft-X-ray intensity is measured by two surface barrier diodes (SBD) arrays (the vertical array has 13 parallel lines of sight with impact parameters lying between $r/a = -0.8$ and $r/a = 0.8$, the horizontal array has 11 lines of sight lying between $r/a = -0.61$ and $r/a = 0.61$) located in the poloidal section. The local toroidal magnetic field is measured with a toroidal array of 32 pairs of pickup coils (named as extensive magnetic measurement system: MMS), which equally distributed around the inboard and outboard sides of the equatorial plane of torus [53]. Therefore, the modes with even or odd poloidal mode numbers can be separated. Since the $m = 0$ and $m = 1$ modes are usually dominant in RFP plasmas, the even mode is called the $m = 0$ mode and the odd mode is called the $m = 1$ mode. A complex edge probe system (CEP) has been developed to measure the high frequency magnetic fluctuations and the floating potentials [51; 54]. The CEP is installed at $r/a \sim 1.0$ inside the vacuum vessel. It is composed of three magnetic coils which can measure the toroidal, poloidal and radial magnetic fields ($\widetilde{B_t}, \widetilde{B_p}, \widetilde{B_r}$) with 1.0 MHz frequency bandwidth, and six pins to measure floating potentials. The layout of the MIR and other diagnostics in TPE-RX is

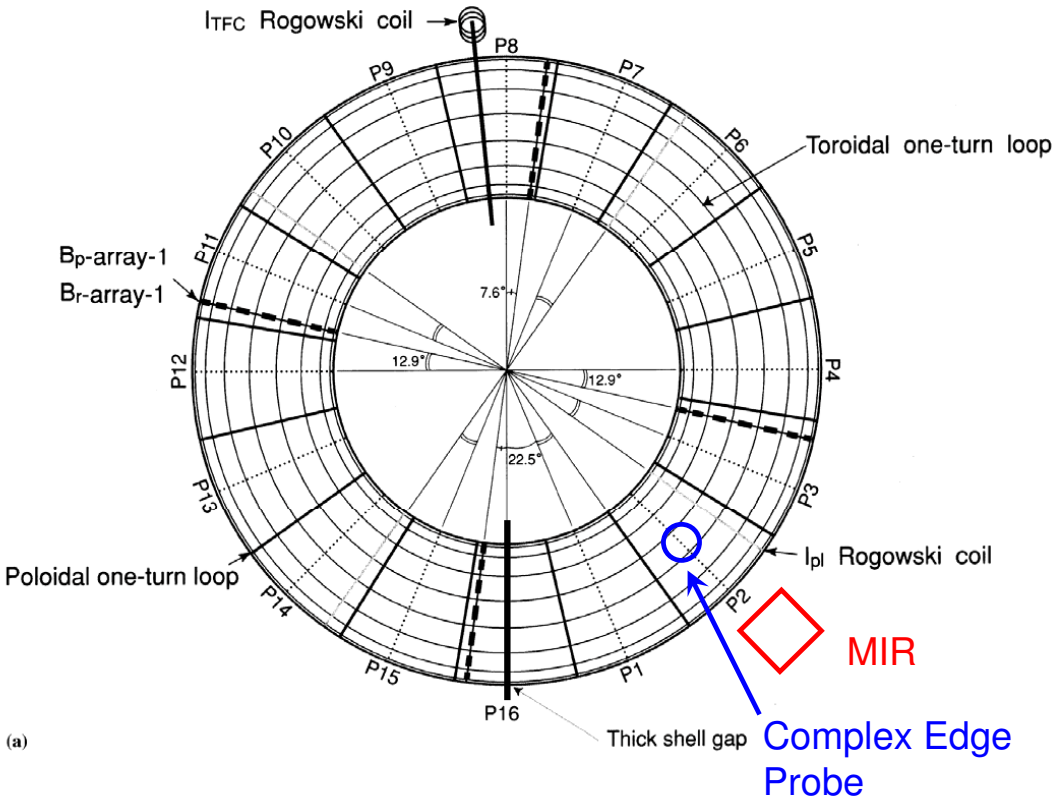

Figure 2.2: Layout of the diagnostics in TPE-RX

shown in figure 2.2. MIR and CEP are arranged at the same port (Port 2). MIR views the equator plane, while CEP is arranged at the top of port.

Plasma parameters	range
Plasma current, Ip	200-350 kA
Electron density, ne	(0.5-1) x 10^{19} m^{-3}
Pinch parameter, $\Theta = B_t(a)/\langle B_t \rangle$	1.4 ~ 1.8 (standard) 1.4 ~ 3.0 (PPCD)
Reversal parameter, $F=B_p(a)/\langle B_t \rangle$	-0.1 ~ -0.6 (standard) -0.1 ~ -2.0 (PPCD)

Table 2.1: Range of the main plasma parameters used in MIR experiments.

Table 2.1 shows the range of the main plasma parameters with MIR measurements in this work. The experiments used in the analysis have the plasma current (I_p) of 200 $\sim$ 300 kA and electron density (n_e) of (0.5 $\sim$ 1.0) $\times 10^{19}$ m^{-3}. The pinch parameter ($\Theta = B_p(a)/ < Bt >$) and the reversal parameters ($F = B_t(a)/ < Bt >$) are $\Theta = 1.4 \sim 1.8$ and $F = -0.1 \sim -0.6$ in standard plasma, respectively. Since the edge toroidal field is generated by the external driven field in PPCD plasma, they are $\Theta = 1.4 \sim 3.0$ and $F = -0.1 \sim -2.0$, respectively.

2.2 MIR system in TPE-RX

Figure 2.3 shows the schematic diagram of the MIR system in TPE-RX [52]. It consists of a optical system and a 2D receiver system. The quartz window of the TPE-RX viewing port is located at $r = 67$ cm. The RF wave illuminating from the horn antenna

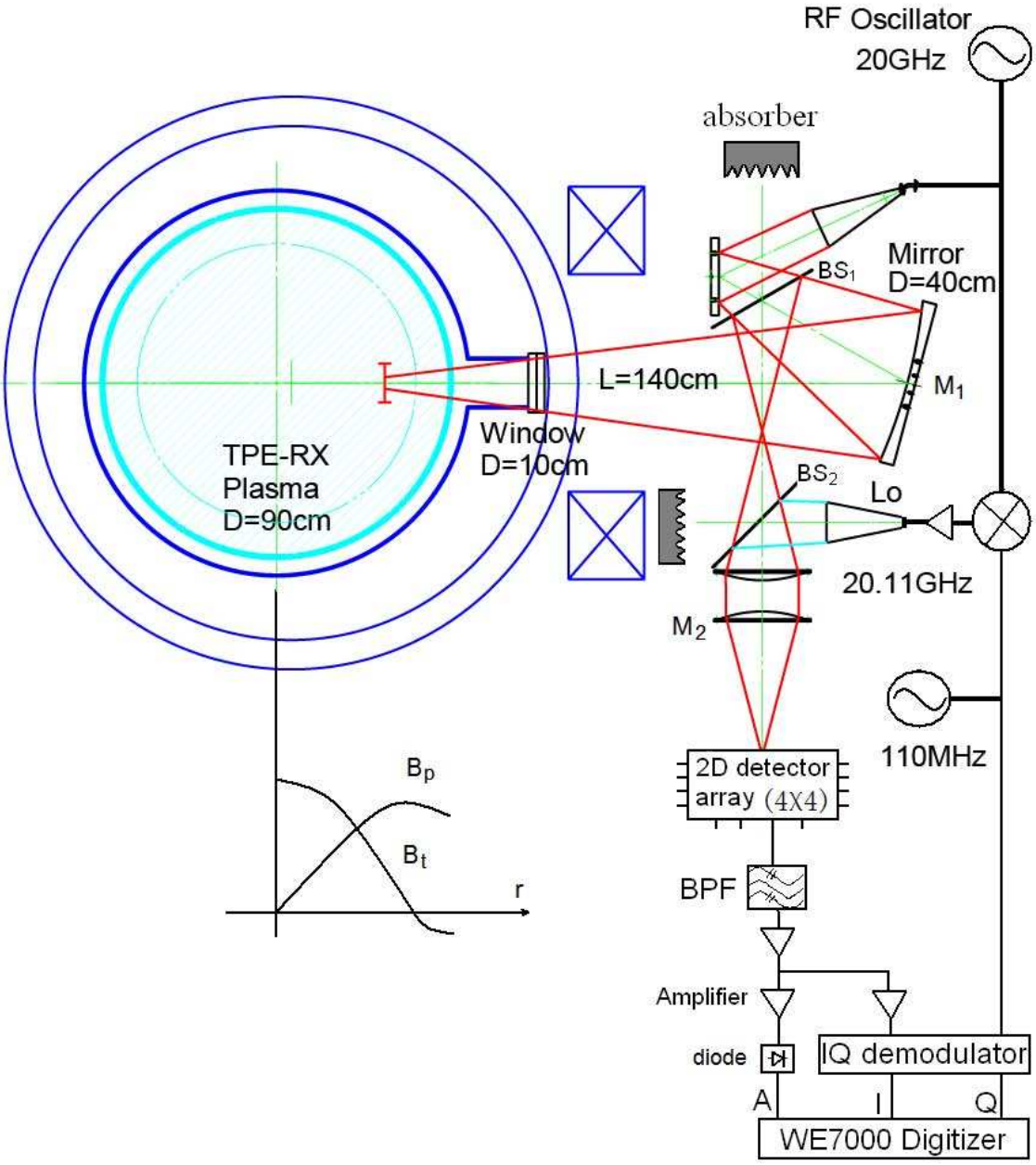

Figure 2.3: Schematic diagram of the MIR system in TPE-RX

is reflected by the first plain mirror (M_1). The RF wave passes through the first beam splitter (BS_1) to the main mirror (M_2). The main mirror, which is an elliptic concave mirror with the size of 40 cm in diameter at $r = 140$ cm, makes a parallel illumination beam in the plasma. The reflected wave is collected by the main mirror and is separated from the illumination beam by the first beam splitter (BS_1). The local oscillation (LO) wave and the reflected wave are mixed at the second beam splitter (BS_2). These beam splitters are 3 mm thick Plexiglas plates. The image of the plasma fluctuation is made on the detector surface by the Teflon lens (L_1). The optical system has been designed and tested carefully. Good agreement between the measured beam profiles and those obtained by a ray tracing simulation was confirmed.

The receiver system consists of a planer Yagi-Uda antenna, a balun, a beam lead type Schottky barrier diode, band pass filter (BPF), intermediate frequency (IF) amplifier and phase-detector. The Yagi-Uda antenna array is made on the Teflon printed circuit board (PCB) with the thickness of 0.18 mm. On the design of the antenna system, a computer code for electro-magnetic field is employed. The 4 by 4 2D antenna and detector circuits are made by the microstrip line technology. The detector system has high sensitivity to the small fluctuation. 4 elements of the antennas are set on a PCB with a distance of 12 mm, and 4 PCBs are stacked with a distance of 15 mm. The spatial resolution of the detector array in the plasma is about 3.7 cm. The schematic diagram of 4×4 2D antenna array in the MIR system is shown in figure 2.4. The circled digits in the picture represent the detector number. The setup of the detector position can be changed in the experiments.

A Gunn oscillator generating the microwave with frequency of 20 GHz is used. Since the magnetic field is very low (~ 0.1 Tesla) in TPE-RX and it is mainly poloidal at the edge, the RF wave illuminates in the O-mode and the cutoff frequency is determined by the electron density $n_{e-cut} \approx \omega_p^2/81 = 0.5 \times 10^{19}$ m^{-3}. The LO wave with the frequency of 20.11 GHz is made by mixing the RF wave (20 GHz) and the low frequency wave (110 MHz) at an up-converter. By mixing the reflected wave and the LO wave, the 2D mixer array makes intermediate frequency (IF) signal of 110 MHz. This IF signal contains the amplitude A and the phase ϕ of the density fluctuation $A\exp(i\phi)$ in plasma. The amplitude is obtained by rectifying the IF signal with a diode detector. The phase is obtained by comparing the IF wave and the mixed signal by the IQ demodulator. I and Q signals correspond to the in-phase $I = A\cos(\phi)$ and the quadrature $Q = A\sin(\phi)$ components of the density fluctuation, respectively. The phase is given as

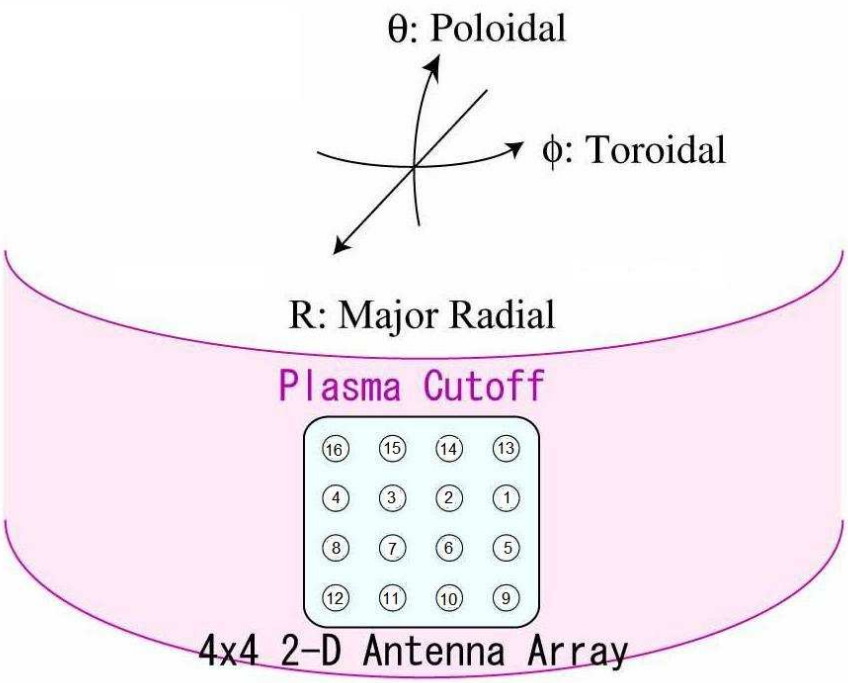

Figure 2.4: Schematic diagram of 2D antenna array in the MIR system. The circled digits represent the detector number

$\phi = \arctan(Q/I)$. The data is sampled at 1 MHz (standard plasma) or 2 MHz (PPCD plasma) by the digitizer.

2.3 Experimental results

2.3.1 Estimation of the cutoff surface

The plasma density is measured by a double-chord CO2/HeNe laser interferometer in TPE-RX, whose impact parameters, normalized by a, are $r/a = 0$ and 0.69. The density profile is estimated by fitting the experimental data with the following relation [52].

$$n_e(r,t) = n_e(0,t)(1-r^4)(1+C(t)r^4) \tag{2.1}$$

where, $n_e(0,t)$ is the core density, $C(t)$ is the profile factor. The profile factor $C > 1$ represents the hollow density and $C < 1$ represents the peaked density profile. Both $n_e(0,t)$ and $C(t)$ are determined by the two measured chord values.

Figure 2.5 shows the (a) time evolution of the density profile in the PPCD plasma (shot No. # 52971), (b) time evolution of live averaged density n_{el} and the normalized cutoff radius of MIR r_{cut}, and (c) density profiles at t = 10, 16, 21, 26, and 30 ms. The PPCD operation starts at 18 ms and ends at 35 ms. The plasma density profile becomes hollow and the plasma density increases during PPCD. The large oscillations in the line-averaged density may be caused by the mechanical oscillation. Although the density has a large error, the normalized cutoff radius of MIR (20 GHz) keeps at near $r/a = 0.7 \sim 0.9$ during the flat top of the discharge due to the very flat or hollow density profile. It should be noted that the flat or hollow density profile is often observed in PPCD and standard plasmas. As a result, the normalized cutoff radius is mainly located in the region from $r/a = 0.6$ to 0.9. This region is near the reversed field surface. The strong turbulence is expected due to the densely packed $m = 1$ modes (high n modes) and high electrostatic turbulence [4; 23]. On the other hand, it is very useful for the calibration of the optical aberration in the MIR optical system.

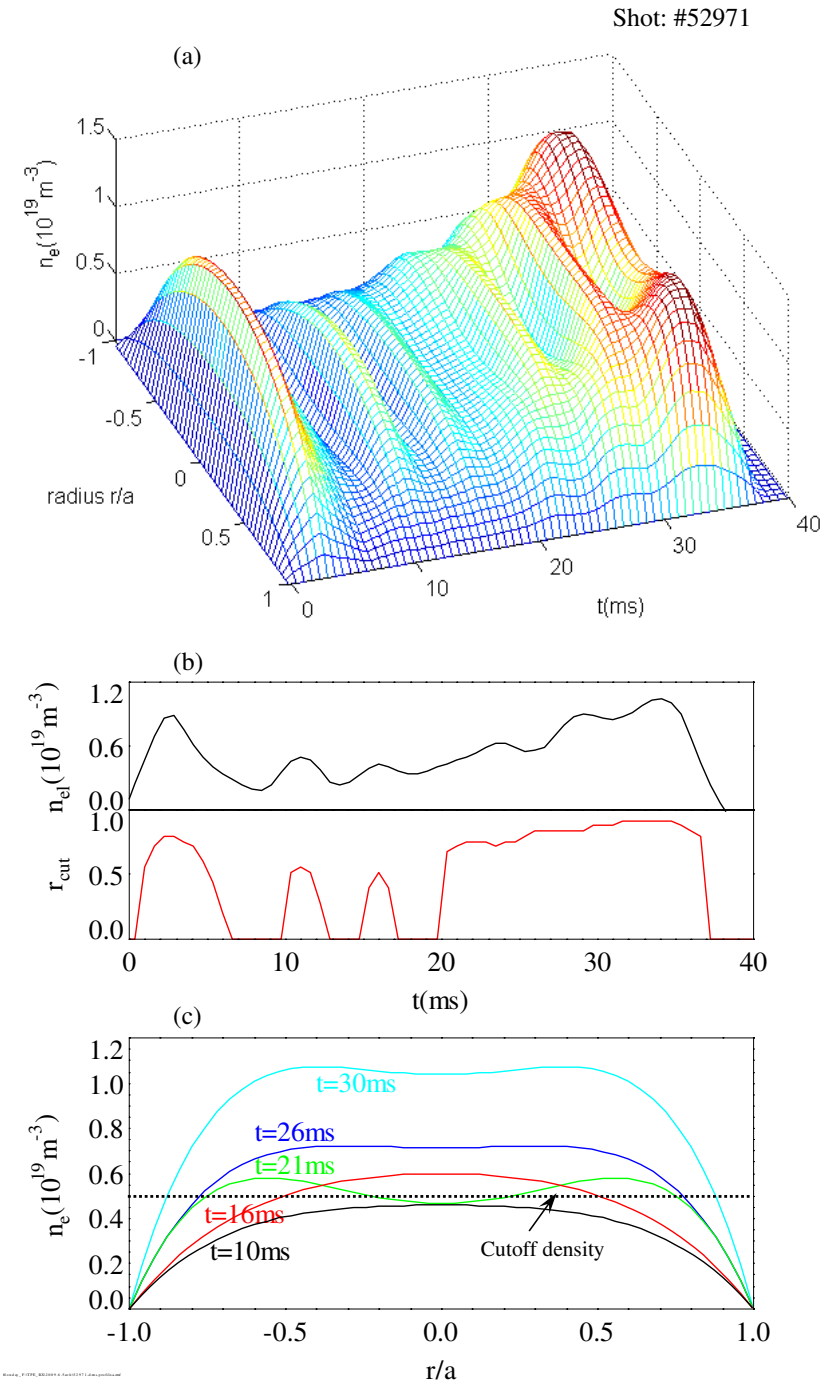

Figure 2.5: (a) Time evolution of the density profile in a PPCD plasma, (b) time evolution of live averaged density and cutoff radius of MIR, (c) density profiles at t = 10, 16, 21, 26, 30 ms.

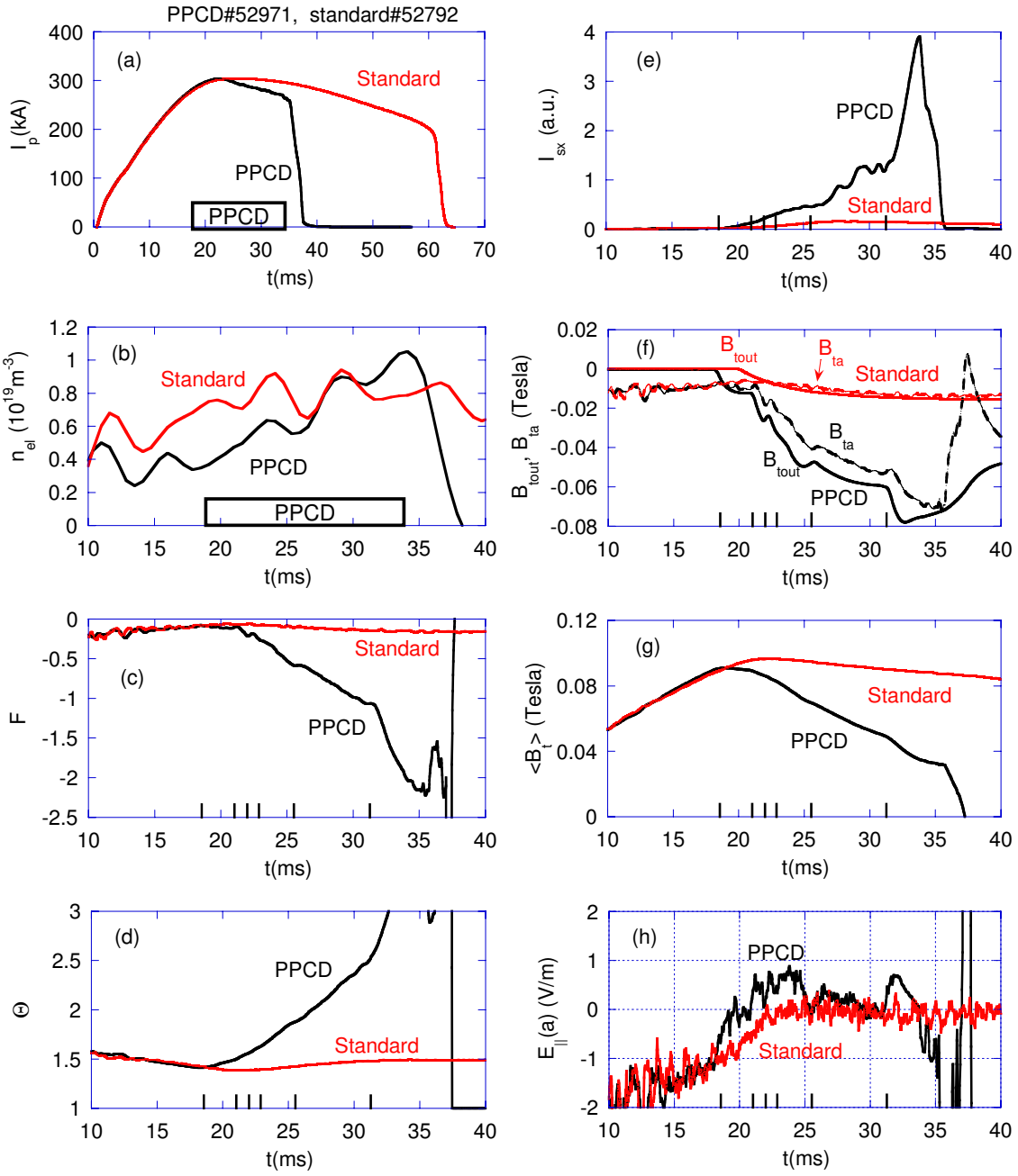

Figure 2.6: Waveforms of the PPCD and the standard plasmas. (a) plasma current, (b) line-averaged density, (c) F, (d) Θ, (e) soft X-ray, (f) toroidal magnetic field at outside of the wall (B_{tout}: solid line) and at the plasma surface (B_{ta}: broken line), (g) total toroidal average magnetic field, (h) parallel electric field to the magnetic field at the plasma surface.

2.3.2 Operation conditions of PPCD and standard plasmas

Figure 2.6 shows the waveforms of (a) plasma current, (b) line-averaged density, (c) F, (d) Θ, (e) soft X-ray, (f) toroidal magnetic fields at outside of the wall (B_{tout}: solid line) and at the plasma surface (B_{ta}: broken line), (g) total toroidal average magnetic field, and (h) parallel electric field to the magnetic field at the plasma surface ($E_{\parallel}$) in PPCD (black) and standard (red) plasmas. The plasma duration time is about 70 ms in the standard plasma (shot: 52792) and 35ms in the PPCD plasma (shot: 52971) (see figure 2.6 (a)). The plasma current is about 300 kA during the flat top of the discharge. $E_{\parallel}$ is estimated by [55]

$$\begin{aligned} E_{\parallel} &= \frac{E(a)\cdot B(a)}{|B(a)|} \\ &= \frac{B_{ta}V_{ta}/(2\pi R) + B_{pa}V_{pa}/(2\pi a)}{\sqrt{B_{ta}^2 + B_{pa}^2}} \end{aligned} \tag{2.2}$$

where, R and a are the major and minor radii, respectively. V_{ta} and V_{pa} are the toroidal and poloidal on-turn voltages at the plasma surface, respectively. $E(a)$ is the electric field at the plasma surface. $B(a)$ is the magnetic field at the plasma surface, and B_{pa} is the poloidal magnetic field at the plasma surface, given as

$$B_{pa} = \frac{\mu_0 I_p}{2\pi a} \tag{2.3}$$

B_{ta} is generated by the external coil current and also by an induced current in the liner. The poloidal one-turn voltage is induced by a change in the total toroidal magnetic field. The total toroidal magnetic field $< B_t >$ increases during the ramp up phase (< 20 ms, in figure 2.6 (g)) and induces a poloidal current in the liner. The reversal field can be sustained without B_{tout} (in standard plasma) by driving the plasma current. $E_{\parallel}$ is usually negative in a standard plasma. The dynamo activity can be reduced when $E_{\parallel}$ is positive [50]. The PPCD power supply in TPE-RX consists of six groups of capacitor banks, which can produce six pulses. Therefore, B_{tout} is stepped down six times.

The PPCD waveform is controlled to maintain a positive $E_{\parallel}$ as long as possible. The optimized PPCD timing is shown by the short lines in the bottom of figure 2.6 (e)-(h). The total toroidal magnetic field $< B_t >$ decreases after applying the PPCD, and the poloidal electric field is induced. As a result, $E_{\parallel}$ increases rapidly and becomes positive (figure 2.6 (h)). The soft X-ray increases more than ten fold. Since the total toroidal magnetic field $< B_t >$ decreases smoothly during PPCD, the pinch parameter

$\Theta = B_p(a)/ < B_t >$ increases rapidly and the reversal parameter $F = B_t(a)/ < B_t >$ decreases rapidly (figure 2.6 (c),(d)). The details of the PPCD and standard operations in TPE-RX are described in ref. [30; 55].

2.3.3 Features of MIR signals

The 2D density fluctuations have been measured in TPE-RX by using MIR. Figure 2.7 shows the time evolution of the plasma current (I_p), F, Θ, the line-averaged density (n_e) and the normalized cutoff radius (r_{cut}), and the MIR signals (Amplitude, I and Q signals) in the 2D detector array in shot #52971, respectively. MIR signals represent the density fluctuations when the cutoff surface appears. The fluctuation amplitude is very small when there is no cutoff surface, for example at $t = 5 \sim 9$ ms. MIR obtains the interferometer signal and the fluctuation of the signals is very small. The sharp burst at $t = 7.5$ ms may be caused by the suddenly presence of the cutoff surface. There is no cutoff surface at $t = 12 \sim 18$ ms but the fluctuation of the MIR signals is increased. This may be due to the stronger radial dependence than r^4 (see Eq. 2.1) in the actual density profile. The fluctuation of the MIR signal is increased as the cutoff surface moves out. During the flattop of the discharge, the fluctuation amplitude of the MIR signals becomes constant. and the normalized cutoff radius is about r/a=0.8 $\sim$ 0.9, which is near the surface of field reversal.

The waveforms of MIR signals look similar in the 2D detector array, especially for the large fluctuations (for example, the crash at $t = 20.005$ ms). It suggests that there are some waves or turbulent structures which propagate on the cutoff surface. The MIR signals also contain many short period bursts with small-scales, for example the fluctuation at $t = 20.04$ ms. If we expand the waveforms, the time delay of the fluctuation structures between different channels can be obtained. The time delay represents the propagation time the turbulence eddy. Therefore, the 2D image of the density turbulence is obtained by MIR.

Since the IQ signals are the cosine and sine components of the phase fluctuation, the Lissajous' curve (I-Q plot) should be a circle. The operation of the IQ detector is confirmed as the trajectory is rotating. In the test of IQ detector, the Lissajous' curve is a circular arc. Therefore, the IQ plot can be used to identify the movement of the cutoff surface or the fluctuation of the phase. One circle represents the motion of 1.5 cm in the radial direction at present setup in MIR. However, the Lissajous' curve is not

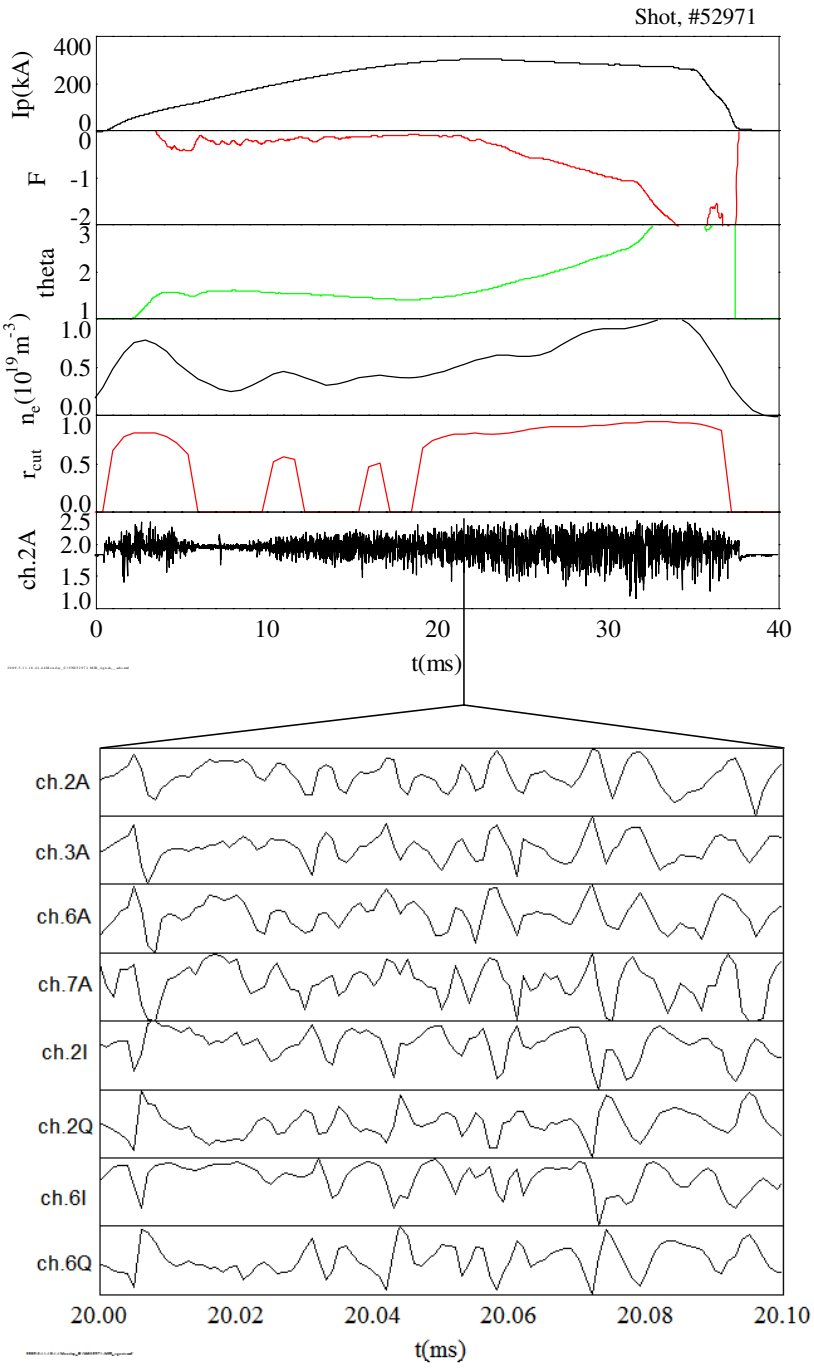

Figure 2.7: Plasma parameters and MIR signals in the PPCD plasma. From top to bottom they are the plasma current, F, Θ, line-averaged density, cutoff radius, the amplitude signals of channel 2 and the MIR signals in 2D detector array (Amplitude and IQ signals), respectively.

always circle in the experiments. It is distorted by the curvature of the reflection surface, turbulence and plasma rotation [56; 57].

Figure 2.8 shows the Lissajous' curves of the I and Q signals with (a) 1 ms time window, (b) 50 μs time window and (c) no cutoff surface (shot No. #52973). The complex IQ-plot looks like a doughnut if there is cutoff surface in plasma, which suggests MIR makes a clear imaging of the cutoff surface. In the case of small time window (see figure 2.8 (b)), the movement of the IQ signals is observed. The rotation of the I and Q signals indicates the cutoff surface is moving back and forth. The turn over points are indicated by the arrows. This corresponds to that the motion of the reflection surface is turned over. If there is no cutoff surface in the plasma, the complex IQ plot has characteristics of random walk and the signals are distributed in the center of the complex IQ plot.

Figure 2.9 shows the coherence of the amplitude and the IQ signals with the toroidal separation of 3.7 cm. The coherence analysis is performed during the flattop of the plasma (data length: 6 ms). The data of a 6 ms time window (1MHz sampling) is divided into 200 data sections. Each section has 64 data points. The coherence is obtained by the Fourier transform of these data sections. The dashed line is the uncertainty (noise) level which is decided by the independent data sections ($1/\sqrt{N}$). The detail of the coherence analysis method is discussed in chapter 4. The coherence decreases as the frequency increases. In the low frequency range (f <100 kHz), both the amplitude and the IQ signals have the high coherence (greater than 0.8). In the high frequency range (f > 100 kHz), the coherence of IQ signals is higher than that of amplitude. At about 400 $\sim$ 500 kHz, the coherence of amplitude becomes the noise level, while the coherence of IQ signals is about 0.3 $\sim$ 0.4. This is about two times higher than that of amplitude. Therefore, the IQ signal is more sensitive to the high frequency fluctuation. The higher coherence in the high frequency range suggests the longer coherence length is measured by the IQ signals.

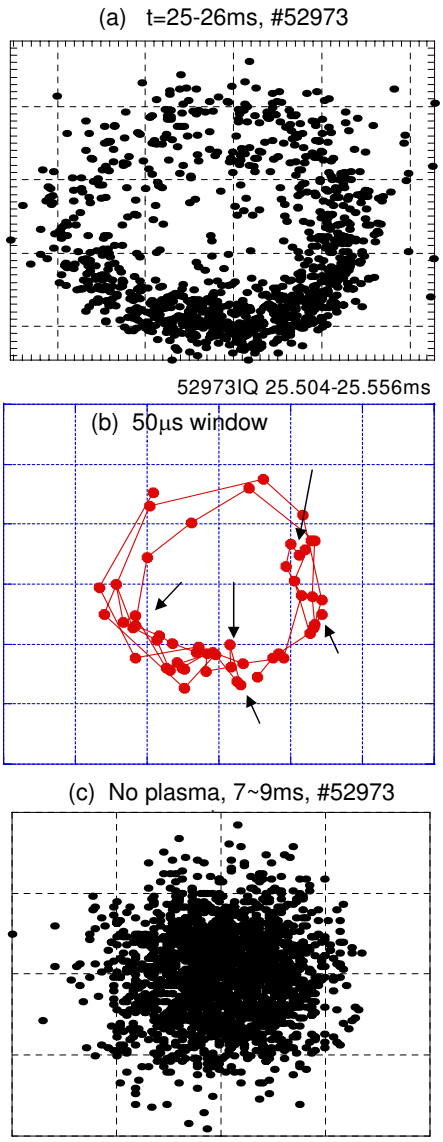

Figure 2.8: The Lissajous' curve (IQ-plot) of the I and Q signals of channel 1 (#52973). (a) 1ms time window (25 $\sim$ 26 ms) and (b) 50 μs time window (25.5 $\sim$ 25.55 ms) and (c) no cutoff surface (7 $\sim$ 9 ms) of channel 1. x-axis is I signal and y-axis is Q signal. The arrows represent the turn over points

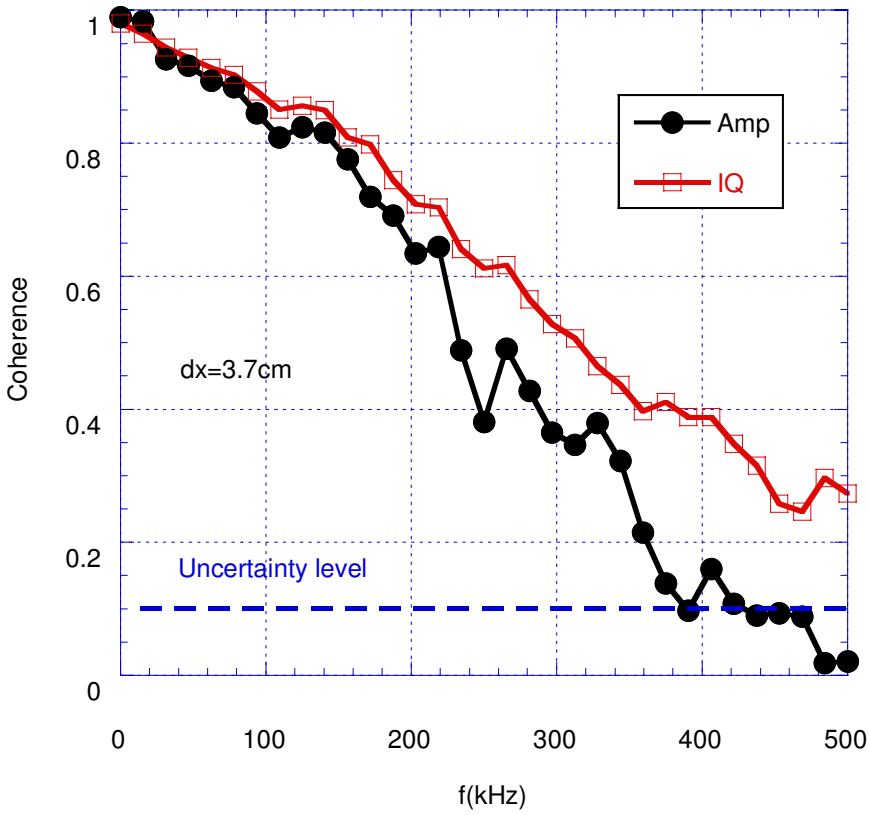

Figure 2.9: The coherence of the amplitude and the IQ signals with the toroidal separation of 3.7 cm

Chapter 3

Two-dimensional Simulations and Tests of MIR

3.1 Introduction

Microwave reflectometry is a powerful tool to measure the plasma density profile and density fluctuation [1; 9; 58]. In a reflectometry system, the microwave illuminates the plasma, and the microwave is reflected by the cutoff surface in the plasma. The reflected power is scattered by the modes on the cutoff surface. The phase difference between the illumination wave and the reflection wave is modulated by the radial displacement of the cutoff surface. The reflection wave is mainly modulated by the density fluctuations close to the cutoff surface, and the phase fluctuation is proportional to the density fluctuation as $\phi \propto L_n \tilde{n}/n$, where $L_n = n/(dn/dr)_{r=r_c}$ is the reverse density gradient length at the cutoff surface. The wave propagation is well understood in the one-dimensional (1D) reflectometry system [1]. However, in the two-dimensional (2D) and three-dimensional (3D) configurations the complicated interference pattern appears on the detection plane, because the reflected wave propagates in different directions. Therefore, it is difficult to extract any useful information from the fluctuations in a standard reflectometry [1; 2; 10; 56].

To correct the disturbed wave front, microwave imaging reflectometry (MIR) is developed [1; 2]. It uses the optical imaging technique in the reflectometry. A wide aperture

optics system is used to form an image of the reflected surface onto a 2D detector array located at the image plane. The time evolutions of 2D pictures of density fluctuation at the cutoff surface can be obtained, just like a movie. The feasibilities of MIR for turbulence measurement have been investigated in theories and experiments intensively [1; 2; 11–14]. The understanding of the received signals is very important to develop the next generation of MIR system. There remain many issues [2; 11; 15], such as the fringe jump, the antenna array and receiver array. Among them, the optical aberration is one of the biggest issues. Therefore, the optical system will be considered in the simulation.

Simulations have been performed at the standard reflectometry without imaging optics in many literatures [12; 56; 59]. In this work, the 2D numerical simulation model based on the Huygens-Fresnel equation is used to simulate the wave propagation in a microwave imaging system. The optical lens is considered in this model. A laboratory arrangement of the MIR system is made to test the reflected signal, which is compared with the simulation. The experimental results show that the MIR system works well at the in-focus condition when the displacement of the cutoff surface in the radial direction is much smaller than the wavelength of the launching wave. The Lissajous' curves of simulation and experiments have the shapes of circular arc when the MIR system is arranged at the in-focus condition. The reflected signals exhibit large random fluctuations at the out-of-focus conditions. Therefore, the in-focus of optics in MIR system is one of the key issues to obtain a bright reflected image. However, in the case of strong fluctuation, the reflected signals are distorted. Both the simulation and the experiments show that the distortions of the reflected signals depend on not only the displacement of the fluctuation in radial direction but also the wave number of the fluctuation. Their relationships are discussed by a geometrical model.

Section 3.2 contains a description of the numerical simulation based on the Huygens-Fresnel equation, which is used for the propagation of the reflected signals. The simulations with different amplitude and the phase fluctuations are shown. The arrangement of the MIR is described in section 3.3. The experimental signals are compared with simulations in the case of weak and strong fluctuations. The phase error of the test is given in section 3.4.

3.2 Numerical simulation

3.2.1 Model

The electric field in all space can be calculated from the Maxwell equation. It is used in the reflectometer model for the propagation of reflected signals. In this simulation, we assume the wave is only reflected at the cutoff surface in vacuum. The solutions of the homogeneous wave equation by means of Fourier method in a cartesian coordinate system (x, z) are given as follows [59]

$$E(x,z) = \frac{1}{2\pi}\int_{-\infty}^{\infty} E_z(k_z) e^{i(k_z z + x\sqrt{k_0^2 - k_z^2})} dk_z \tag{3.1}$$

$$E_z(k_z) = \int_{-\infty}^{\infty} E_0(z) e^{-ik_z z} dz \tag{3.2}$$

where k_0 is the wavenumber of the incident microwave, $E_0(z)$ is the distribution of the incident microwave at position x_0, given as:

$$E_0(z) = E_{x_0}(z) e^{-z^2/w^2} e^{ik_0 z^2/\rho} e^{i\phi} \tag{3.3}$$

here, x represents the radial direction and z represents the vertical direction. The first term $E_{x_0}(z)$ is the amplitude of the original electric field at the cutoff surface. It is a constant in a 1D model while it is modulated by the cutoff surface in a 2D model. $E_{x_0}(z) = \cos(2\arctan(dR_c(x,z)/dz))$ is used in this simulation, $R_c(x,z)$ is the function of cutoff surface. The second term e^{-z^2/w^2} denotes the Gaussian incident beam, and w is the $1/e$ fold of the Gaussian beam intensity. The third term $e^{ik_0 z^2/\rho}$ comes from the curvature effects of the cutoff surface and the incident wave front. The $\rho = \rho_c\rho_w/(\rho_c+\rho_w)$ is the effective curvature radius, where ρ_c and ρ_w are the curvature radius of cutoff surface and the incident wave front, respectively. Since the plane wave is used in MIR, we can assume $\rho \approx \rho_c$. The curvature effect becomes prominent at the inner reflection. The forth term $e^{i\phi}$ represents the phase modulation by density fluctuation.

The phase difference between the reference wave and the reflected wave is calculated in the 1D geometrical optics. It is given as:

$$\phi = 2k_0 \int_{x_0}^{x_{cut}} \epsilon^{1/2}\, dx \tag{3.4}$$

where ϵ is plasma permittivity which is a function of plasma density and magnetic field (X-mode)(see equation 1.3 and 1.4).

A poloidal plasma density fluctuation causes a phase modulation with poloidal wavenumber k_p. Assume the fluctuation is localized near the cutoff surface and the fluctuation radius is much smaller than the cutoff radius, the cutoff surface is given as:

$$R_c(x,z) = x^2/R_0 + (z-z_0)^2/R_0 + \sum_j d_j \sin(k_{p_j}(\sigma_j)z + \theta_j) \tag{3.5}$$

where d_j is the fluctuation amplitude which corresponds to the displacement in the x (or radial) direction, the wavenumber k_{p_j} has the standard deviation σ_j, θ_j represents the initial phase, z_0 is the vertical shift of the cutoff surface, and R_0 is the cutoff radius without fluctuation.

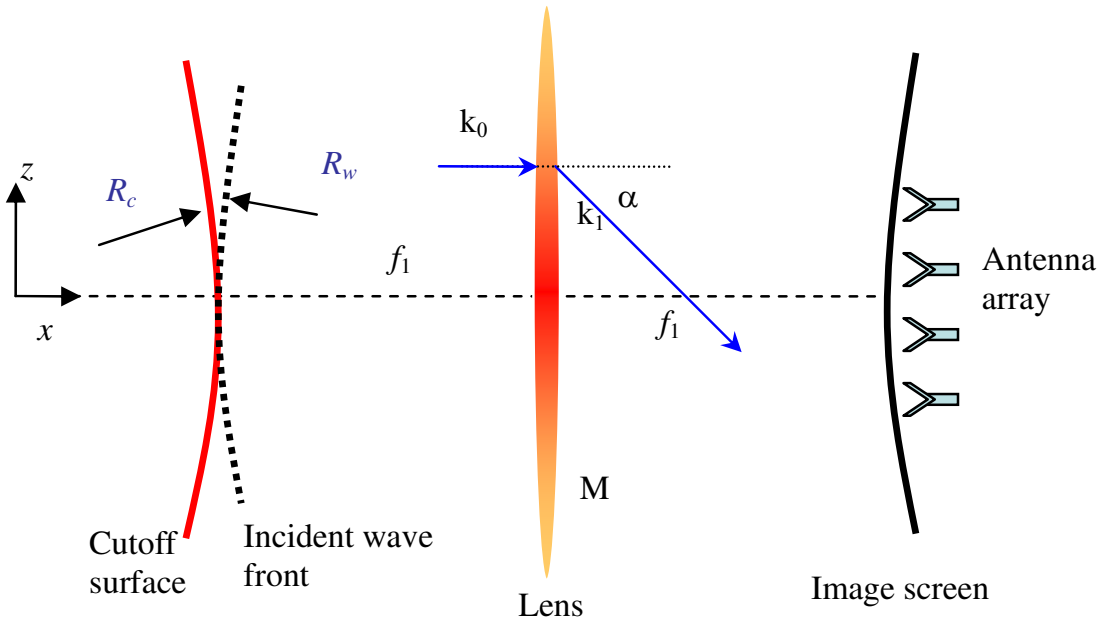

Figure 3.1: The model of the reflectometer imaging system.

In general, the concave mirror is used in the MIR optics system. The role of the concave mirror is similar to the convex lens, which can make a convergent beam. The mirror system in MIR is simplified to one optical lens. Figure 3.1 shows the schematic view of MIR. The image of the cutoff surface at the detector screen is made by the

optical lens M. The wave propagation direction rotates an angle α by the optical lens M. The electric field is changed as:

$$\begin{aligned} E(x,z) &= E_M(x,z)e^{-i\alpha} \\ &= E_M(x,z)e^{-i0.5k_0z^2/\sqrt{f_1^2+z^2}} \end{aligned} \tag{3.6}$$

where $E_M(x,z)$ is the electric field at the optical lens M and f_1 is the focal length. If the focal length is infinite, the optical lens M can be considered a plane mirror.

The wide aperture lens is necessary to obtain a definitional image. The small optical lens may lose some of the reflected beam and reduce the imaging depth (low brightness). Experimentally, the size of the optical lens should be at least two times larger than the image size. On the other hand, the solution of the electric field in this model is based on the WKB approximation, which requires the fluctuations should be in the range of $k < k_0(k_0L_\epsilon)^{1/3}$, where L_ϵ is the scale length of the plasma permittivity: $L_\epsilon = 1/(d\epsilon/dx)|_{x=x_{cut}}$ [1].

3.2.2 Numerical results

The amplitude modulation of the reflected wave is mainly caused by the perpendicular (azimuthal) fluctuations which scatter the reflection wave. To obtain a large amplitude modification, we assume that the fluctuation amplitude (displacement in the x direction) is $d = \lambda_0$, where λ_0 is the wavelength of the incident wave. Figure 3.2 (a) shows the contour plot of the amplitude of electric field in the imaging system. Here, we assume the cutoff surface is at $x = 40$ cm. The launched wave is a plane wave with the frequency of 20 GHz and the beam width of 20 cm. The wave is reflected and modified by the cutoff surface. An aperture with a diameter of 30 cm is set at $x = 67$ cm. The optical lens with a focal length of 50 cm is arranged at $x = 140$ cm. Therefore, the inverse image is made at $x = 240$ cm according to the principle of geometrical optics. We assume the poloidal wavenumber is $k_p = 0.2$ cm^{-1} with the deviation of 0.1 cm^{-1}. The interference pattern is observed outside of the cutoff surface. The beam becomes convergent when it passes through the optical lens, and the image of the cutoff surface is made at the image plane. Figure 3.2 (b) shows the amplitude distributions of the electric field at $x = 40$ cm (solid line), $x = 67$ cm (dashed line) and $x = 240$ cm (long dashed line). The peak of the electric field amplitude in cutoff surface is at $z = 2$ cm while it is at $z = -2$ cm

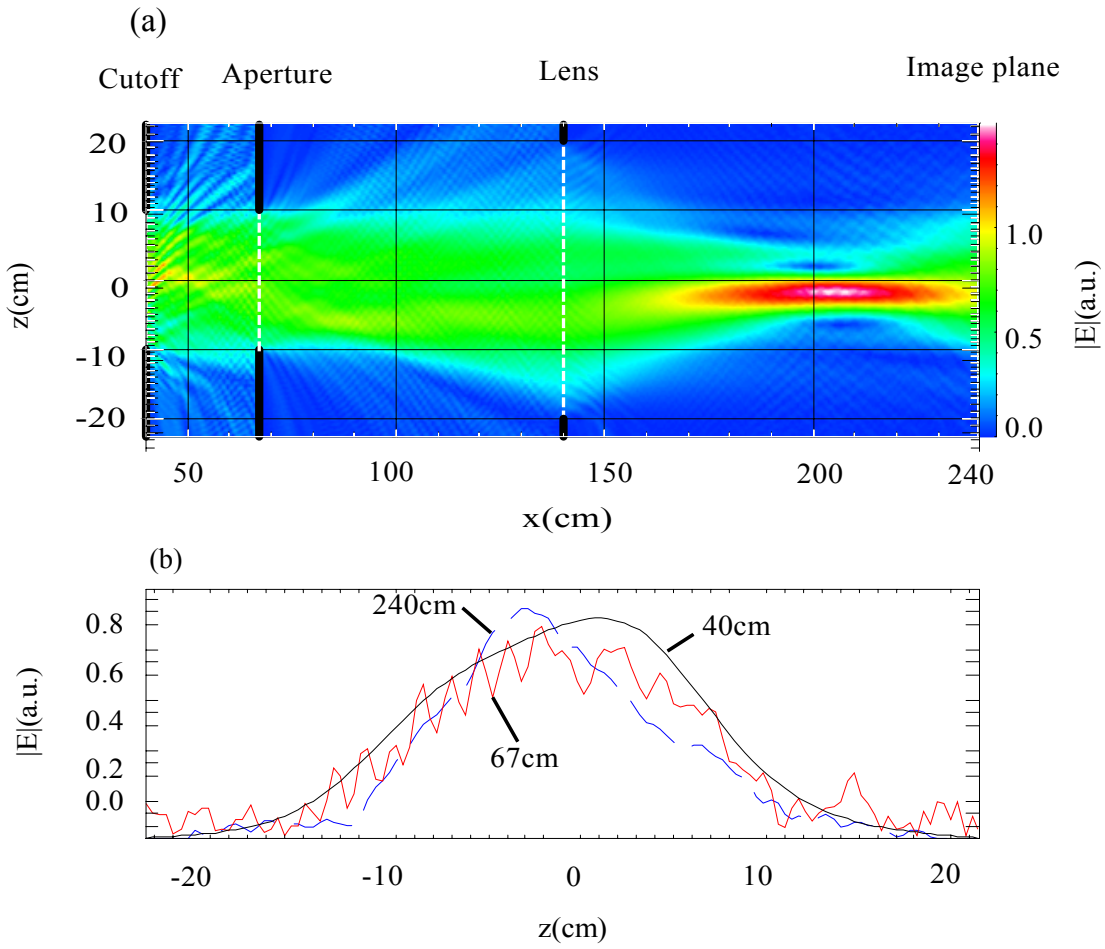

Figure 3.2: (a) The contour plot of the calculated electric field intensity in the imaging system. (b) The electric field amplitude profiles at $x = 40$ cm (solid line), $x = 67$ cm (dashed line) and $x = 240$ cm (long dashed line).

in the image plane. The profile of the electric field amplitude at $x = 67$ cm shows large fluctuation. Therefore, the reflected wave is deformed at away from the image plane.

Figure 3.3 shows the waveforms of the reflected wave with the phase fluctuation of π. Here we assume the fluctuation of the cutoff surface is modulated by a sinusoidal wave with the poloidal wavenumber $k_p = 0.2$ cm^{-1} and the phase fluctuation is $\phi = \pi$. The phase at the imaging plane is a sinusoidal wave which is similar to the fluctuation of the cutoff surface. The amplitude is slightly deformed by the scattering wave. The amplitude peak is obtained when the cutoff surface is perpendicular to the illumination wave. As a result, the frequency of the amplitude fluctuation is two times higher than that of the phase fluctuation if the mode only propagates in the perpendicular surface. It should be noted that the frequency of the amplitude signal mainly depends on the perpendicular velocity of the mode, as $\omega = k_\perp v_\perp$. Therefore, the interpretation of the phase fluctuations is easier than the amplitude fluctuations.

The phase modulation of the reflected wave is mainly produced by the radial fluctuations of the cutoff layer. Figure 3.4 plots the complex amplitude of the reflected waves at (a) in-focus, (b) weak-focus and (c) out-of-focus conditions of the fluctuation amplitude $d = \lambda_0/4$, and at the (d) in-focus of fluctuation amplitude $d = 3\lambda_0/2$. Therefore, the phase fluctuations in the radial direction are $\widetilde{\phi} = 1.0\pi$ and $\widetilde{\phi} = 6.0\pi$ due to the beam illuminating back and forth. The other parameters are the same as those in figure 3.2. In the case of weak fluctuation, the Lissajous' plot is a half circle at the in-focus condition. When the focus becomes weak, the Lissajous' plot changes to waning moon shape. At the out-of-focus condition, the Lissajous' plot exhibits large and random fluctuations. In the case of strong fluctuation, the Lissajous' plot shows deformed circles at the in-focus position. Therefore, the phase is distorted at strong fluctuation.

3.3 Laboratory test of MIR

3.3.1 Arrangement of MIR system

Figure 3.5 shows the Schematic view of the MIR system used in a laboratory test. It consists of optical elements (i.e., mirrors, optical lenses, beam splitters and antennas) and a 2D receiver system. The radio-frequency (RF) wave illuminating from the horn antenna is reflected by the first beam splitter (BS_1), and comes to the main mirror (M).

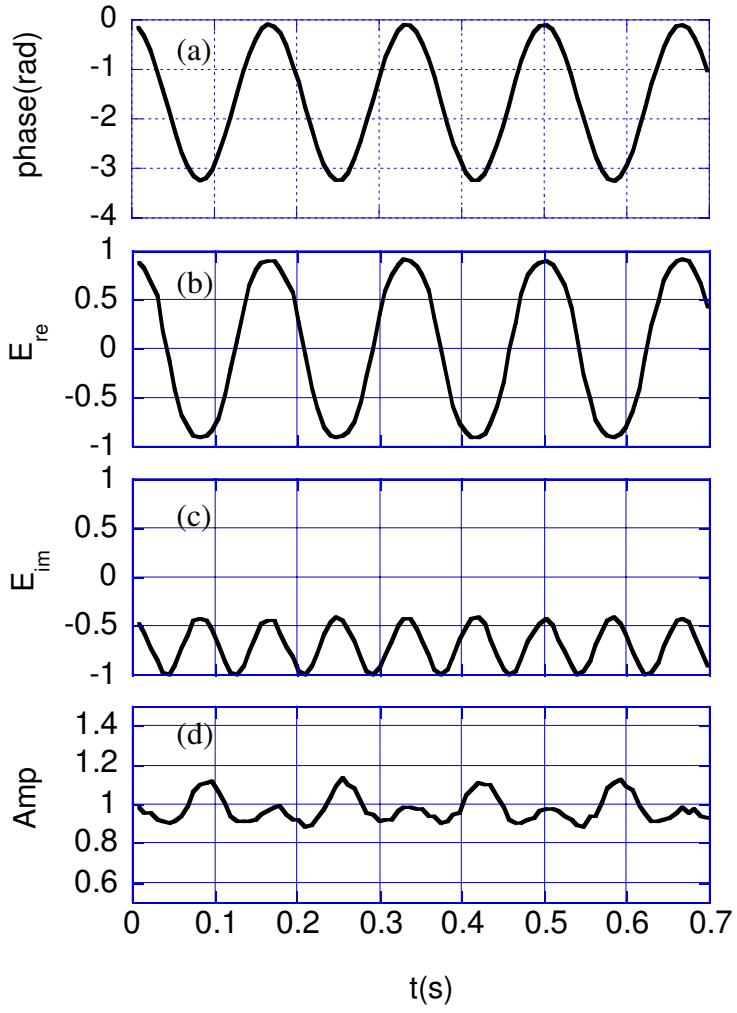

Figure 3.3: Waveforms of the reflected wave from the MIR model with the phase fluctuation ($\phi = \pi$) and $k_p = 0.2$ cm^{-1}. They are the phase (a), the real (b) and imaginary (c) parts of the reflection wave, the amplitude (d) from the top to bottom, respectively.

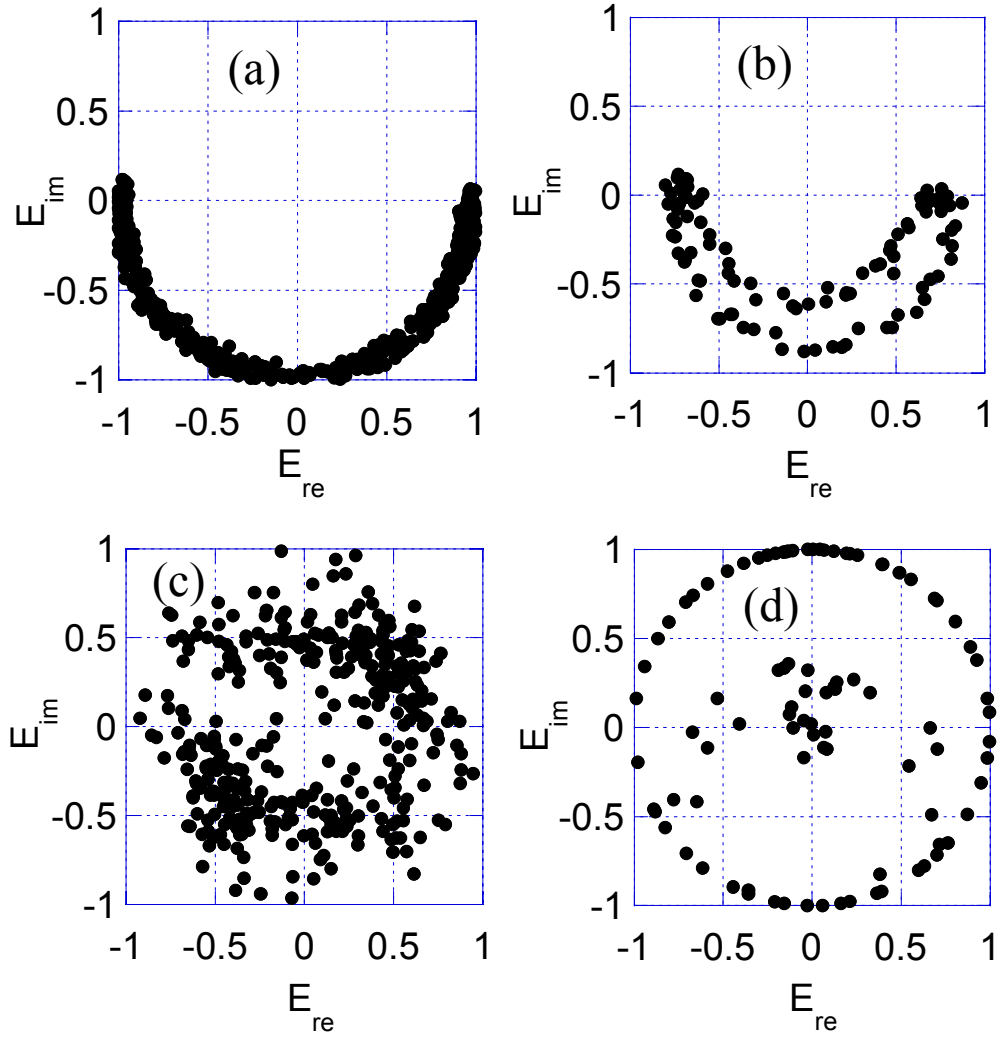

Figure 3.4: The complex plots of the reflected waves with $\widetilde{\phi} = 1.0\pi$ at (a) in-focus, (b) weak-focus, (c) out-of-focus conditions, and (d) in-focus of $\widetilde{\phi} = 6.0\pi$.

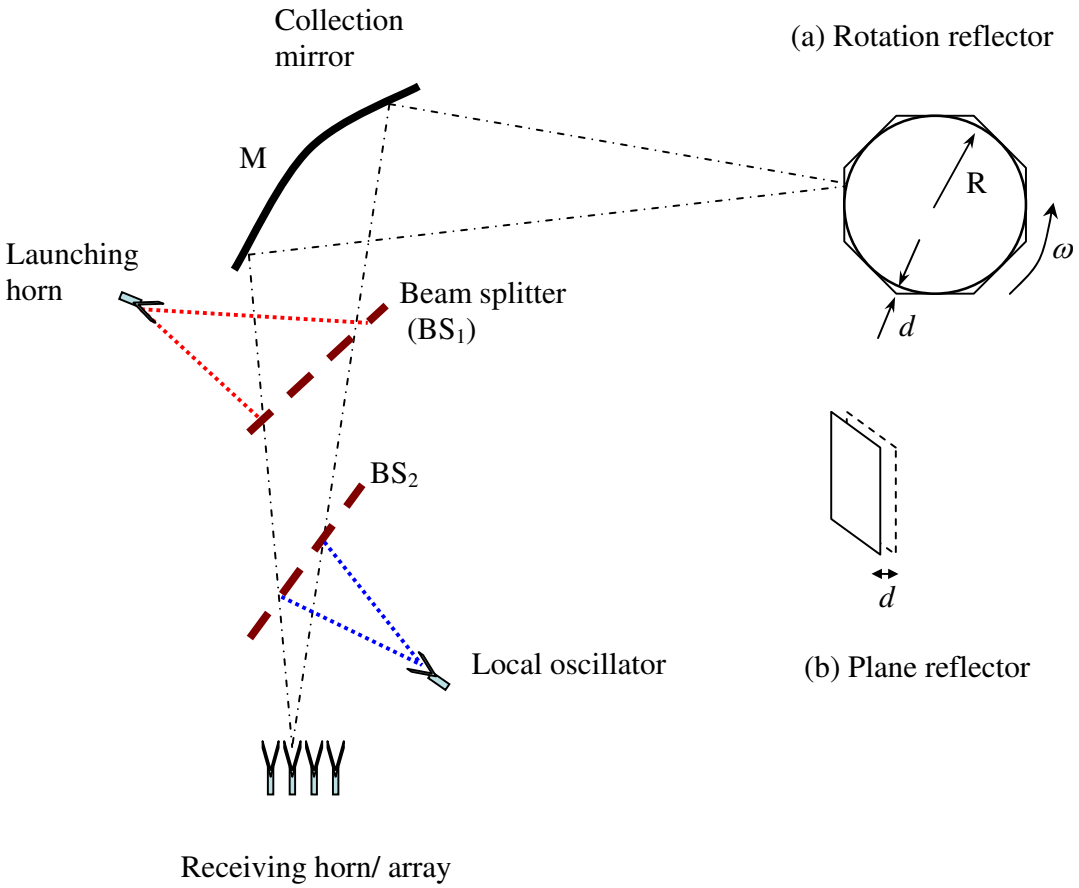

Figure 3.5: Schematic view of the laboratory arrangement for microwave imaging reflectormtery. The plane and rotation reflectors are used. In the test, the plane reflector moves back and forth in the x direction. The rotation reflector is made of a wood disk with a sinusoid corrugation with the wavenumber of k_p and the depth of d. The disk is driven by an electric motor.

The main mirror, which is an elliptic concave mirror with the size of 50 cm in diameter, makes a parallel beam to illuminate the reflector. The plane and rotation reflectors are used. In the test, the plane reflector moves back and forth in the x direction with distance d. The rotation reflector is made of a thick wood disk (2 cm) with a sinusoid corrugation with the poloidal wavenumber of k_p and the depth of d. The disk is covered with the aluminum foil. The disk is driven by an electric motor in the experiment. The reflected wave is collected by the collection mirror (M) and is separated from the illumination beam by the first beam splitter (BS_1). The local oscillation (LO) wave and the reflected wave are mixed at the second beam splitter (BS_2). The beam is focused at the antenna plane. Therefore, an image of the plasma fluctuation is made. A new pyramidal 5 by 8 2D antenna array with a wide band frequency response array is developed (the toroidal separation is 1.6 cm and the poloidal separation is 1 cm. It has been used in the 12^{th} experimental campaign in LHD). The resolution pattern at the object position has been measured by moving a 4 cm diameter spherical ball wrapped by aluminum foil. The size of the radiation pattern is 4.5×4.3 cm and the shape is circular. The detail discussions about the antenna array and the size of the radiation pattern are described by Kuwahara [60].

The launching microwave frequency is 48 GHz. The LO wave with the frequency of 48.11 GHz is made by up-converting the RF wave (48 GHz) and the lower frequency wave (110 MHz) at an up-converter. By mixing the reflected wave and the LO wave, the 2-D mixer array makes intermediate frequency (IF) signal of 110 MHz. This IF signal contains the amplitude (A) and the phase (ϕ). Here, the phase (ϕ) indicates the radial displacement of the reflection layer, and the amplitude (A) represents the reflected power which is scattered by the propagation wave on the cutoff surface. The amplitude is obtained by rectifying the IF signal with a diode detector. The phase is obtained by comparing the IF frequency and the mixed signal by the IQ demodulator. I and Q signals correspond to in-phase signal ($I = A\cos(\phi)$) and quadrature signal ($Q = A\sin(\phi)$), respectively.

3.3.2 Calibration

To obtain an in-focus image of the reflector, the detector array must be arranged at the image plane. The position of the detector array can be calculated by the geometrical optics theory ($1/U + 1/V = 1/f_1$, U is the object distance, V is the image distance and

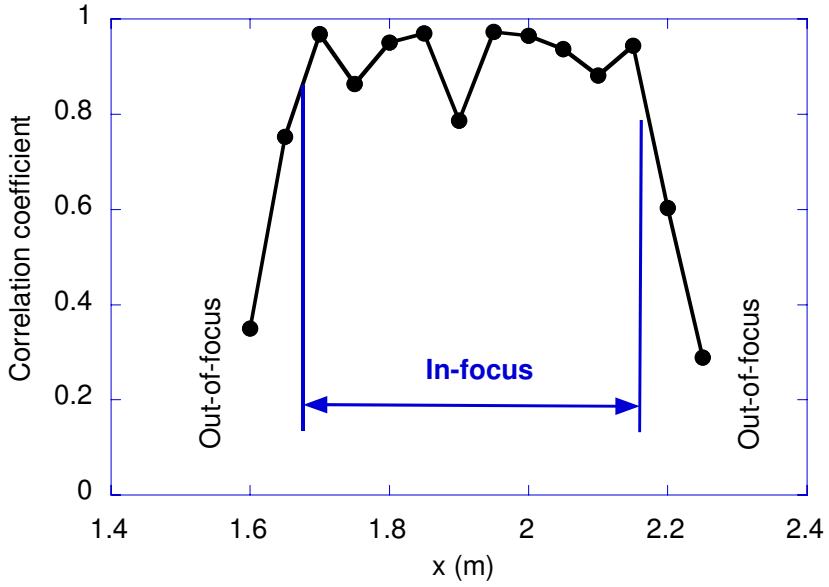

Figure 3.6: The in-focus region of the MIR setup. X-axis is the distance between the reflector and the collection mirror.

f_1 is the focal length). The in-focus image is obtained when the reflector is set at about 2 m away from the collection mirror (M) at present setup. Figure 3.6 shows the cross-correlation of the reflected signals as a function of the distance between the reflector and the collection mirror. The cross-correlation is calculated by the two signals with the distance of 1 cm in the horizontal direction. Here, the plane reflector is used. The cross-correlation is high when the reflector is located at the region between 1.7 m to 2.15 m. This is the in-focus region which agrees with the geometrical optical estimation. Note that the cross-correlation is not exactly one at the in-focus region. It is caused by either the misalignment of the reflector or the optical abbreviation of the MIR system. This problem can be solved by carefully adjusting the optical system. The low correlation at x $>$ 2.2 m and x $<$ 1.6 m indicates out-of-focus condition in MIR system which may cause the phase and amplitude distortions. By the way, the measurement region is mainly decided by the size of the optical mirror. Generally, the larger size of the optics is, the wider and better in-focus image will be.

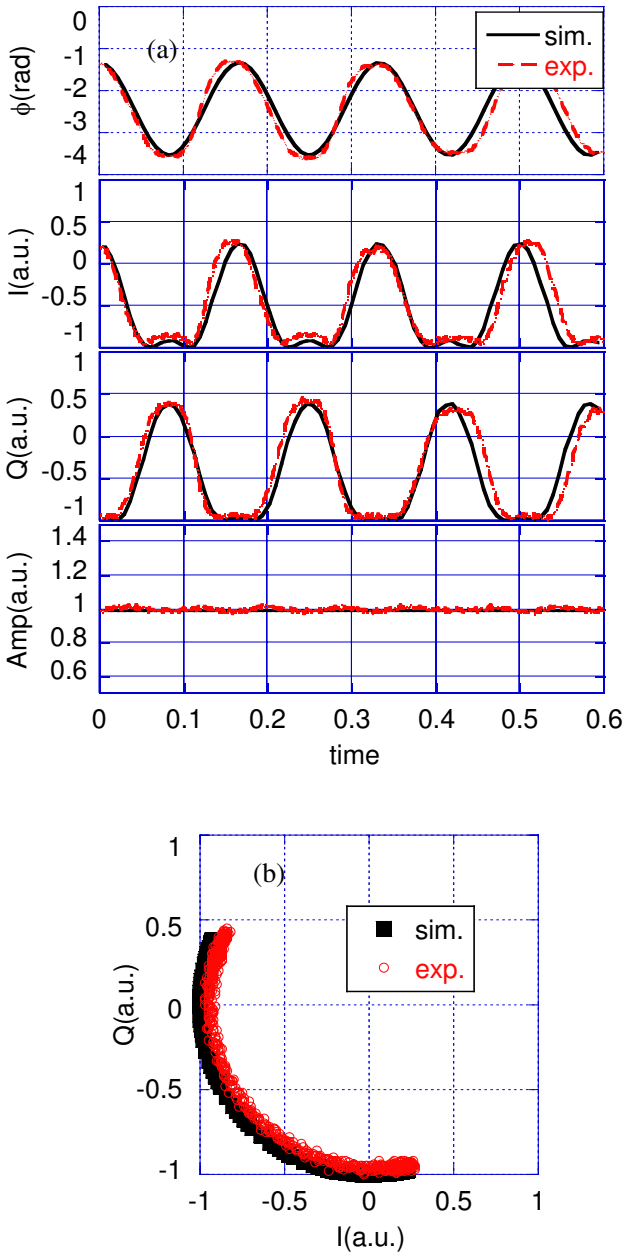

Figure 3.7: Waveforms obtained by the plane reflector with phase fluctuation $\widetilde{\phi} = 0.7\pi$ and the simulation with phase fluctuation $\widetilde{\phi} = 0.7\pi$. (a) The phase, I, Q and amplitude from top to bottom, (b) the Lissajous' curves of test and simulation.

3.3.3 Plane reflector

Measurements are taken with a series of fluctuations when the reflector is arranged at the in-focus region. Figure 3.7 shows the waveforms in the case of weak fluctuation by using the plane reflector. There are (a) the phase, I, Q and amplitude from top to bottom, and (b) the Lissajous' curves of test (black) and simulation (red). The phase is obtained from the I and Q signals. The phase fluctuation is about $\widetilde{\phi} = 0.7\pi$ when the plane reflector moves back and forth with the displacement of 1.1 mm along the x direction. Simulation with the phase fluctuation of $\widetilde{\phi} = 0.7\pi$ ($k_p = 0, d = \lambda_0/6$) is also given in this figure. The simulated signals are quite similar to that obtain in the experiment. The phase fluctuation is quasi-sinusoid which reflects the cutoff surface moves back and forth. The amplitude has small fluctuation while it is constant in the simulation. According to the 1D/2D reflectometer model, the fluctuation in the x (radial) direction can only cause the phase fluctuation, not the amplitude fluctuation. In this test, the amplitude fluctuation is very small, and it might be caused by the misalignment of the plane reflector. The plane reflector didn't move along the x direction exactly. The Lissajous' curve shows a circular arc with the angle of 0.7π. Therefore, the movement of the cutoff surface in radial direction is captured by MIR system.

3.3.4 Rotation reflector

Figure 3.8 shows the waveforms obtained by the rotation reflector with $k_p \approx 0.2$ cm^{-1} and $d \approx 0.8$ mm. The surface of the rotator is sinusoidal-like modulated. The phase fluctuation is about $\phi = 0.6\pi$. Simulation with $k_p = 0.2$ cm^{-1} and the phase fluctuation of 0.6π is also shown (solid line). In this simulation, we assume the fluctuation is a sinusoidal wave. The simulation agrees with the experiment when the phase is slowly changing, for example at $t = 0.18 \sim 0.27$. However, when the phase is rapidly changing, there is some discrepancy in the amplitude signal between the experiment and simulation, for example at $t = 0.28 \sim 0.34$. Although the amplitude signal is deformed, it seems that the phase signal is not deformed very much. The experimental circular arc in the Lissajous' curve agrees with the simulation.

To further understand this problem, a rotation reflector is used in the test. The rotation reflector is corrugated with three types of modulations on the surface. The test results are shown in figure 3.9. The waves with different amplitude modulations

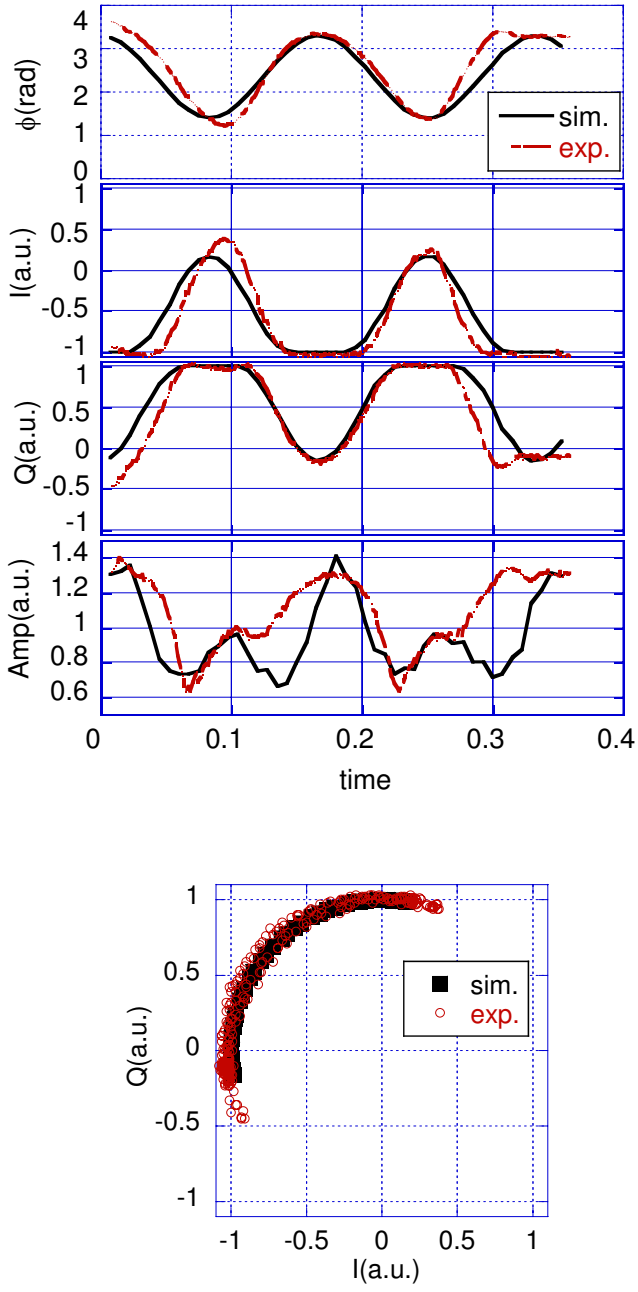

Figure 3.8: Waveforms obtained by the rotation reflector and simulation with phase fluctuation $\phi \approx 0.6\pi$. (a) the phase, I, Q and amplitude from top to bottom, (b) the lissajous' curve of the reflected signal.

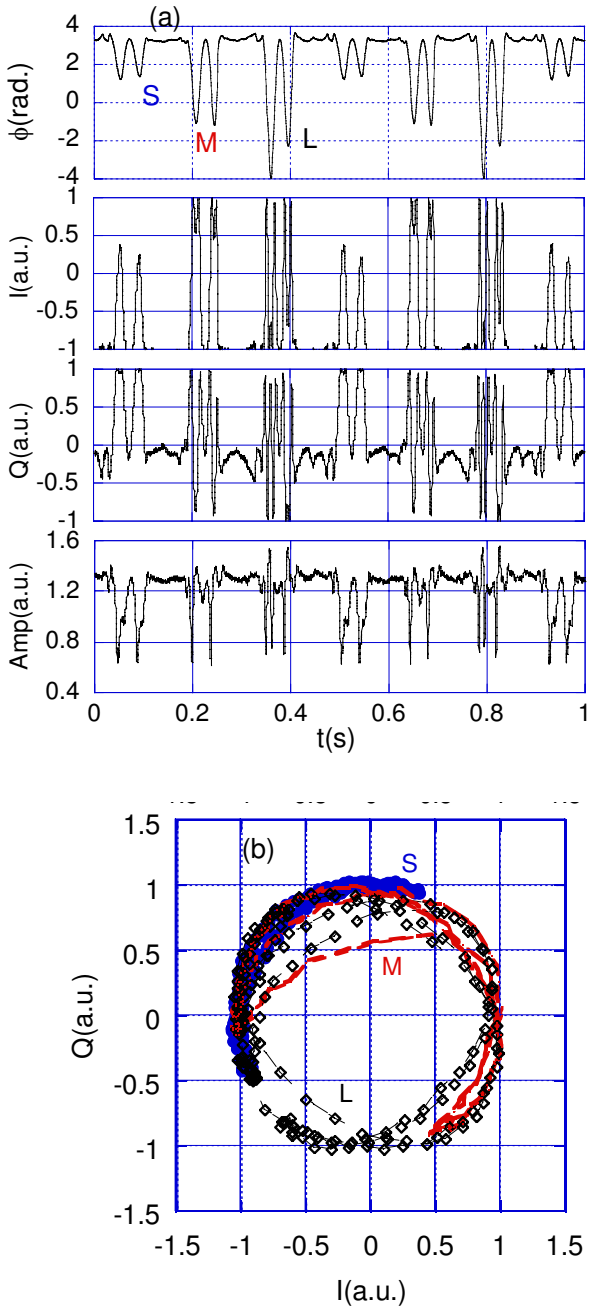

Figure 3.9: Waveforms obtained by the rotation reflector with different amplitude modulations (S, M, L). (a) the phase, I, Q and amplitude from top to bottom, (b) the lissajous' curve of the reflected signal.

are indicated by S, M and L in figure 3.9(a). Here, the S, M and L represent the small ($\widetilde{\phi} = 2/3\pi$), medial ($\widetilde{\phi} = 4/3\pi$) and large ($\widetilde{\phi} = 2\pi$) phase fluctuations, respectively. The fluctuation amplitudes of S, M and L are about 0.1 cm, 0.2 cm and 0.3 cm on the reflector, respectively. The wavenumbers of the waves are about $k = 0.2$ cm^{-1}. The fluctuation signals appear periodically, and the angular velocity of the reflector is estimated about 14.0 rad.s^{-1} in this test.

In the case of small phase fluctuation, the Lissajous' curve is a standard circular arc. The reflected amplitude (power) is also modulated. This is consistent with the phase fluctuation. In the case of medial phase fluctuation the Lissajous' curve is a deformed circular arc, and the reflected amplitude has two large sharp peaks with higher frequency fluctuations. In the case of large phase fluctuation the amplitude has spurious peaks, and the Lissajous' curve is a deformed circle. The amplitude distortion may be caused by the strong interference effect due to the strong fluctuation or the optical abberation of MIR system. Although the Lissajous' curve is deformed, it seems that the phase fluctuation is not so seriously distorted by the strong fluctuation. The phase modulation has a sinusoidal trace which is similar to the reflector surface. It corresponds to the longer correlation length measured by IQ detectors in reflectometer [19; 58]. This result suggests that the phase measurement is necessary to obtain the high correlation signals, especially for the strong and high k fluctuations.

The phase distortion depends not only on the fluctuation amplitude (displacement in radial direction) but also on the wave number of the fluctuation. A rotation reflector with 12 sinusoidal corrugations is made. The modulated amplitude of the corrugation is about $d \approx 1.0$ cm. Therefore, the phase fluctuation is about $\widetilde{\phi} = 6.4\pi$, and the wavenumber is about $k = 0.55$ cm^{-1}. The waveforms of phase, IQ and amplitude signals are shown in figure 3.10. The signals have strong and complicated fluctuations. The Lissajous' plots are deformed. The phase rapidly increases when the reflected amplitude becomes large. The phase stops at small reflected amplitude, leading to the runaway-phase phenomenon which is known in standard reflectometry [15]. One possible reason of the runaway-phase phenomenon is that the cutoff surface reflects the launching beam out of the optical lens when the deviation angle of the cutoff surface is too big, leading to small reflected power at the detector surface. The auto-gain amplifier in the phase detector doesn't work well with small signals. Another reason might be the strong fluctuations may cause a complicated interference pattern near the reflected surface, MIR can't restore the strong fluctuations, and the interference signals are obtained.

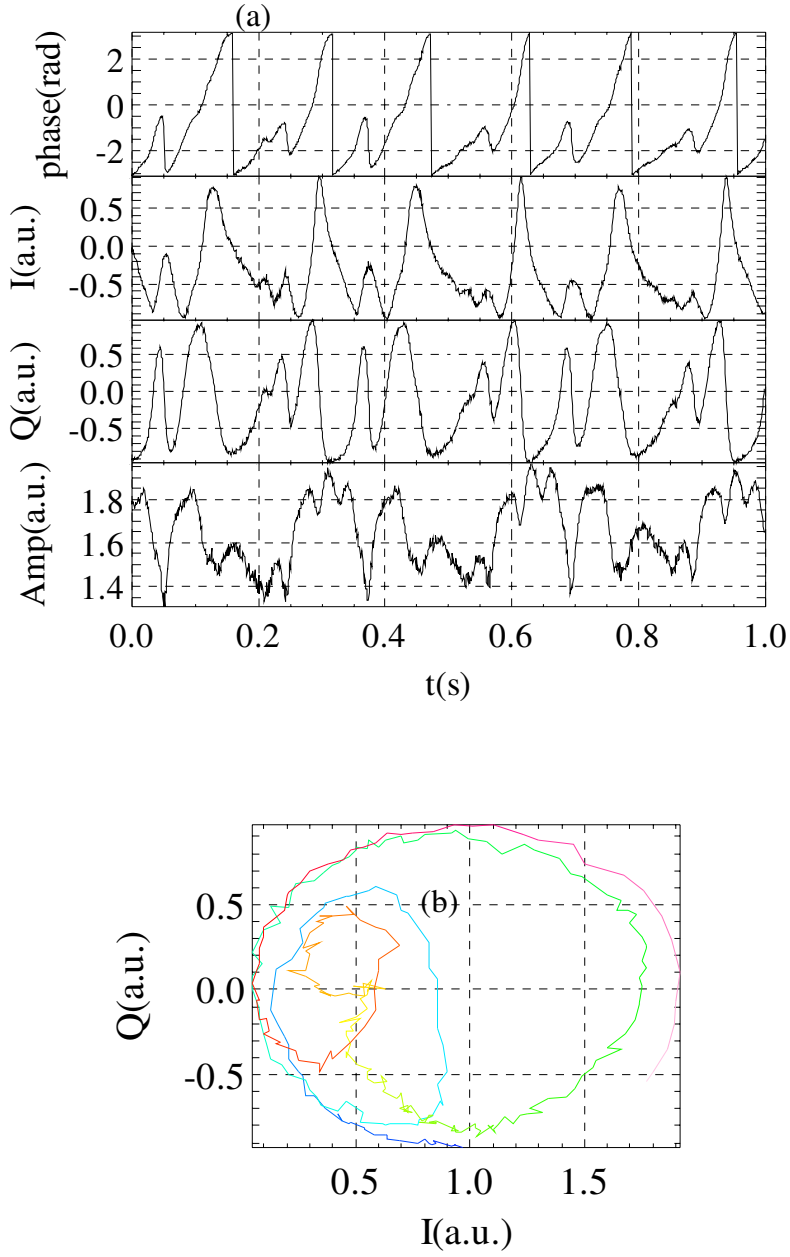

Figure 3.10: Waveforms in the strong fluctuations ($\widetilde{\phi} = 6.4\pi$, $k = 0.55$ cm^{-1}). (a) the phase, I, Q and reflected amplitude from top to bottom, (b) the lissajous' curve of the reflected signal.

This result agrees with the simulation shown in figure 3.4. Therefore, MIR fails to make the clear image in the strong fluctuations.

3.3.5 Wave propagation

The optical abberation of the MIR system can be checked by observing the 2D wave propagations. This is very important to understand the 2D turbulence measurement. The wave is generated by using the rotation reflector. Here, we use three detectors with 1 cm separation in the horizontal direction and three detectors with 1.6 cm separation in the the vertical direction. The reflector is rotating in the vertical direction, so the modulated wave is not propagating in the horizontal direction. Figure 3.11 shows the wave propagation in the (a) horizontal and (b) vertical directions by using the rotation reflector in the case of small fluctuation. To avoid overlapping, channel 2 and 3 are vertically shifted. The propagation of the wave is indicated by the arrows. The time delay of the modulated wave reflects its propagation speed and direction. One can find that the time delay in the horizontal direction is zero, while it is about 0.025 s between the neighboring detectors in the vertical direction. The wave only propagates in the vertical direction. The velocity of the wave in the vertical direction is about 0.64 ms^{-1}. The angular velocity of the rotation reflector is about 18.4 $rad.s^{-1}$ in this test. Therefore, we confirm that the image of the density fluctuation can be obtained by using MIR system in the case of small fluctuation.

However, both the amplitude and the phase will be distorted in the case of strong fluctuation as discussed in the previous section. Figure 3.12 show the wave propagation in the case of strong fluctuations ($d = 0.5$ cm, $k \sim 6$ cm^{-1}). Both the phase and the amplitude fluctuations are deformed. The signals have spurious peaks which may be caused by the interference pattern or out-of-focus of the MIR optical system. The jumps in the phase are caused by the phase runaway. As a result, the propagations of the waves are deformed.

3.4 Limit of phase error

In this simulation, we consider the optical lens in the wave equation at the laboratory scenario. There is no density gradient in the laboratory test, so the permittivity is

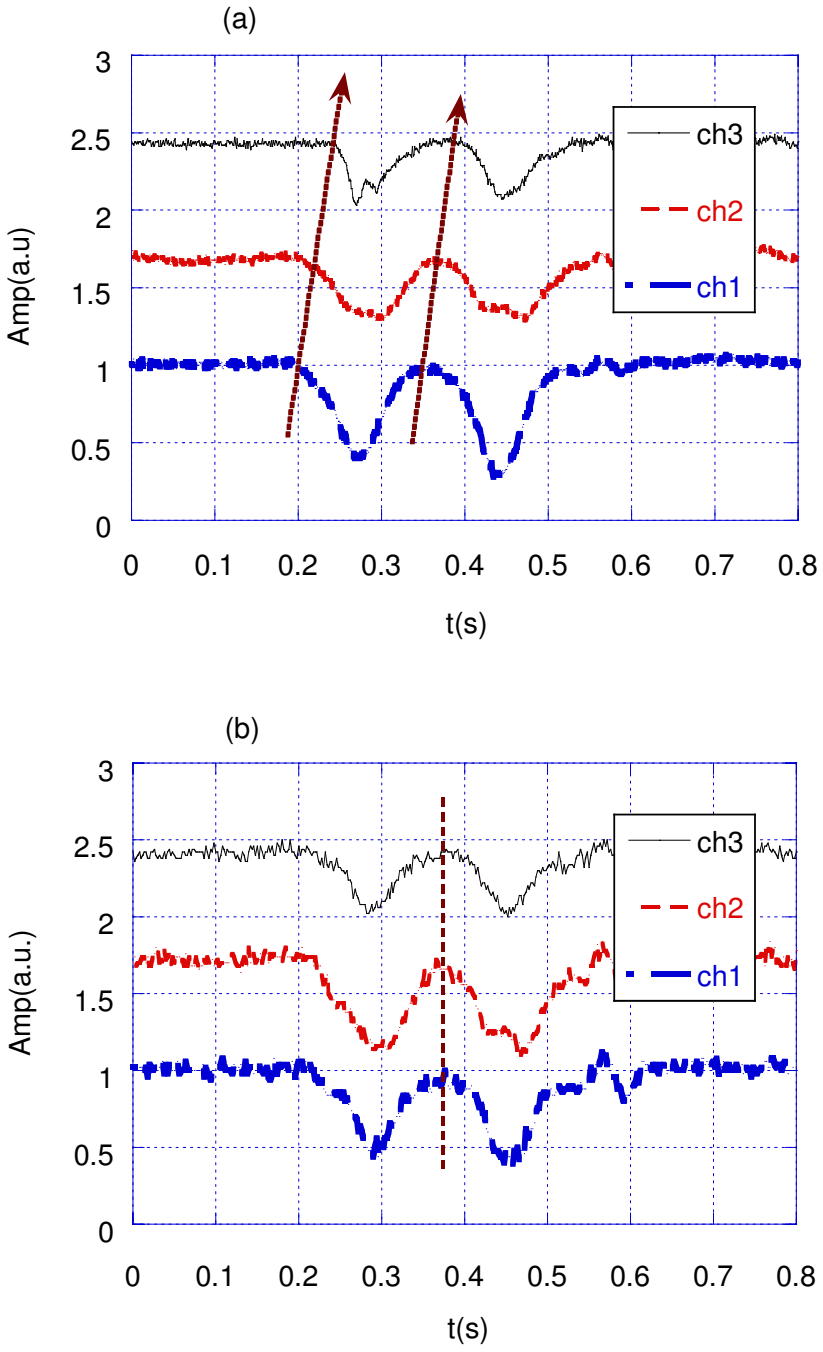

Figure 3.11: The wave propagation in the (a) horizontal and (b) vertical directions by a rotation reflector. The propagation of the wave is indicated by the arrows.

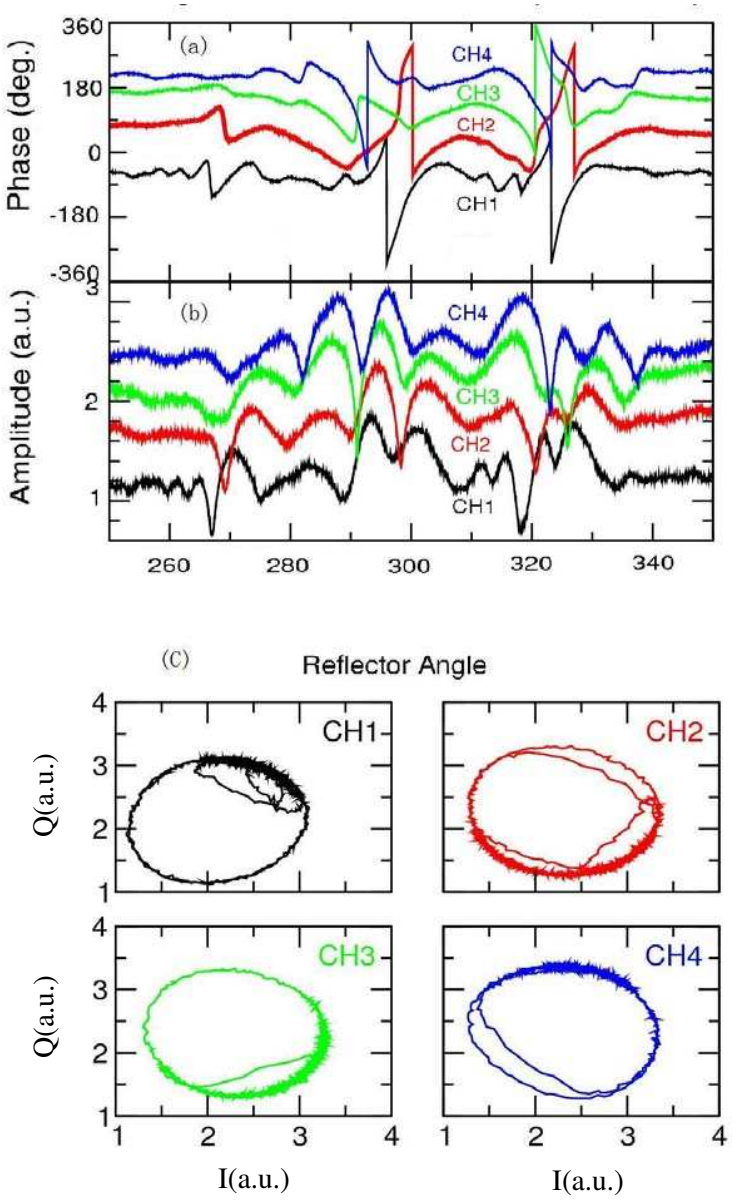

Figure 3.12: The wave propagation in the vertical direction by a rotation reflector in the case of strong fluctuation ($d = 0.5$ cm, $k = 6$ cm^{-1}). (a) the phase, (b) amplitude and (c) Lissajous' plots

constant. It can be used to calibrate the optics system and explain the experimental signals. In the present imaging system, the incident beam is perpendicular to the cutoff surface if the optical system is well designed and arranged. Therefore, the refractive effect is not so serious as expected in the plasma. The approximation in this work might be used for the O-mode plasma. However, it is not true under the most conditions. The full wave equation simulation should be used for the actual plasma test because of the strong diffractive effect. Several similar works, based on synthetic imaging technique and finite-difference time-domain (FDTD) methods, have been carried out [12–14]. Nevertheless, the phase distortion is still a crucial problem in MIR experiments.

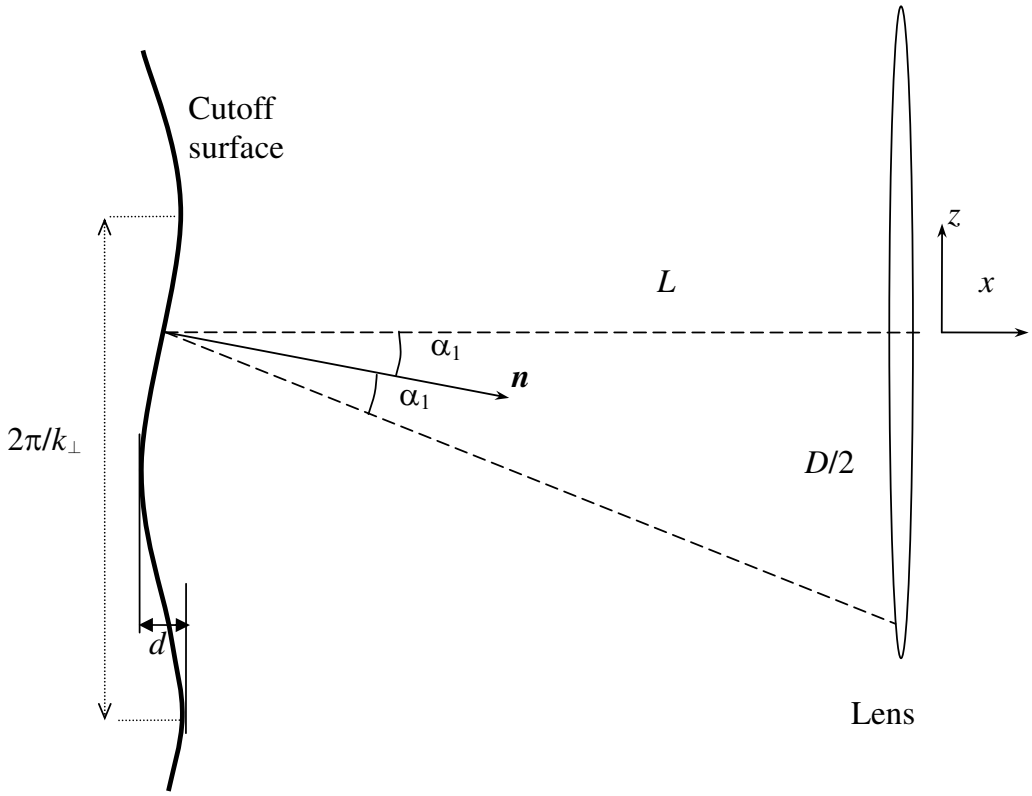

Figure 3.13: Schematic illustration of the beam diffraction

The diffraction effect causes the obscure image with low brightness (not zero) and with mismatch of the wavefront and the fluctuation. It is mainly decided by the size of the aperture optics, the displacement in radial direction and perpendicular wavenumber. The phase distortion can be estimated from the optical arrangement in MIR system. Figure 3.13 shows the schematic illustration of the beam diffraction in the MIR system.

Where, $\boldsymbol{n}$ is a surface normal vector and α_1 is the cutting angle of the cutoff surface, D is the diameter of the optical lens, L is the distance between the optical lens and the reflector surface, $k_\perp$ is the perpendicular wavenumber, d is the displacement in the x direction (fluctuation amplitude). The parallel launching beam is deflected by the angle $2\alpha_1$ with the reflector surface. The phase error increases when the lens can't collect the main reflected beam. If we assume the modulated wave is sinusoidal and $L \gg D$, the relationship between d and k is given as

$$\frac{4k_\perp dL}{D} < 1 \tag{3.7}$$

for the in-focus imaging. The error of the detected phase becomes significant when the radial displacement of the cutoff surface is larger than $D/(4k_\perp L)$. As shown in figure 3.9 (b), the perpendicular wavenumber $k_\perp$ of the modulated wave is estimated about 0.2 cm^{-1}. Therefore, the radial displacement should be smaller than 0.16 cm for the phase fluctuation without distortion. In the case of small fluctuation, the radial displacement is about 0.1 cm, so the circular IQ plots are obtained. In the case of medial and large fluctuations, the radial displacement are 0.2 cm and 0.3 cm, respectively. So the IQ plots are distorted.

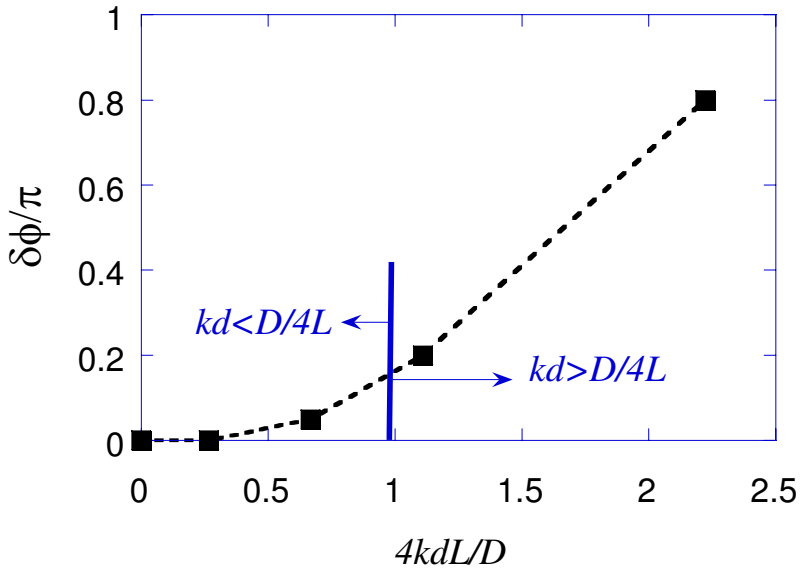

Figure 3.14: The error of the phase fluctuation as a function of $4k_\perp dL/D$

Figure 3.14 shows the error of the phase fluctuation as a function of $4k_\perp dL/D$. The error of the measured phase is smaller than 0.1π in the case of $4k_\perp dL/D < 1$. This

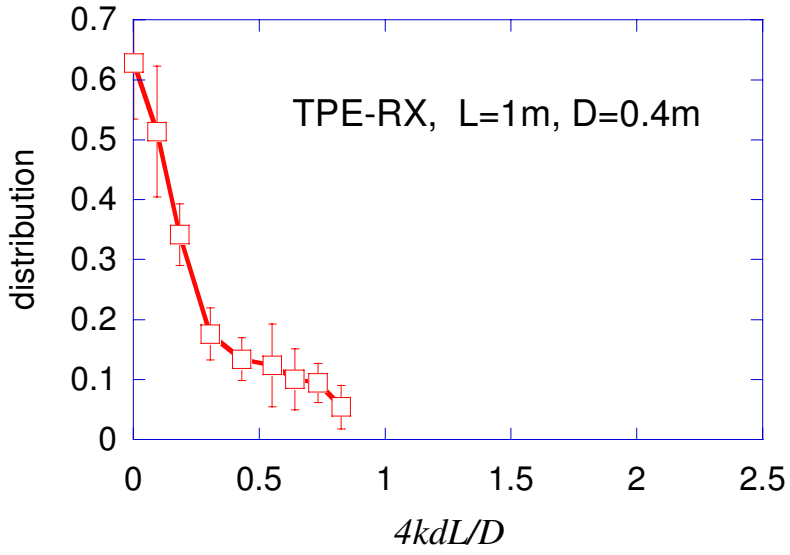

Figure 3.15: The distribution of the fluctuation measured by MIR in TPE-RX

suggests that a clear image of the cutoff surface may be made by MIR. The phase error is increased as $4k_\perp dL/D$ is increased in the case of $4k_\perp dL/D > 1$. Therefore, MIR can't make a clear image of the strong fluctuations with $k_\perp d > D/4L$ due to the strong diffraction effect of the reflected wave.

The equation 3.7 clarifies the relation between the optical parameters of MIR and the fluctuation parameters of the cutoff surface. It can be used to estimate the sensitivity of the MIR optical system to the turbulence. It can be also used to estimate the optical parameters if we know the fluctuation parameters in plasma. The perpendicular wavenumber and the radial displacement of the fluctuations are coupled. In general, high $k_\perp$ fluctuations have small radial displacement in the experiment. The measured $k_\perp d$ is determined by the geometrical parameter of the optical system. In the case of TPE-RX, the distance between the plasma and the main mirror is about 100 cm and the diameter of the main mirror is about 40 cm. Therefore, MIR can measure the fluctuation with $k_\perp d < 0.1$ in TPE-RX plasma.

Figure 3.15 shows the distribution of the fluctuations as a function of $4k_\perp dL/D$ in TPE-RX. The distribution decreases as $4k_\perp dL/D$ increases. The tail of the distribution in the high $k_\perp d$ range may be caused by the strong high k fluctuation or the intermittent burst of the turbulence (see chapter 6), which is often observed in the reversed-field pinch

plasma [41]. Nevertheless, the fluctuations mainly distribute in the range of $4k_{\perp}dL/D < 0.8$ which suggests present MIR optical systems in TPE-RX can make a clear image of the cutoff surface in plasma.

Chapter 4

Development of the Spectral Analysis Techniques

4.1 Introduction

The analysis method is important in the experimental study of turbulence. The real experimental signals are often submerged in the strong background noises such as electronic noise and thermal noise, especially when the signal is very weak. The turbulence has a large number of modes and different ranges of correlations. It is similar to a series of wave packets, which contains many different scales of fluctuations. On the other hand, the turbulence is transient and it always rapidly changes in spatial and temporal domains. The spectrum of the turbulence is broad due to many active modes in the wave packets. The transient turbulent structures may cause the distortion of the spectrum. Sometimes the turbulence is similar to the random noise. Therefore, it is hard to see something from the signal even in the frequency domain. Proper selection of analysis methods can give the direct evidence of the underlying physics of turbulence. On the contrary, miss selection of the analysis methods may lead fake results.

Many numerical noise reduction techniques have been developed in previous studies [61–63]. These techniques use the statistical feature of the random noises, whose power spectral density is similar in the whole frequency band. The expected error of the averaging in Fourier space (or real space and time) decreases monotonically as a function

of the number of the independent data sections in the ensemble average. Therefore, the statistical analysis of a fluctuating quantity over a long period may be useful to pickup fluctuating signals.

Fourier transform is one of the basic analysis methods which can provide the frequency and phase spectra of the fluctuations. However its time resolution is rather poor. The short time Fourier transform can provide the time evolution of the fluctuation spectrum. The frequency resolution becomes worse at high time resolution. Therefore, it is difficult to obtain the time evolution of the rapid changing modes by the traditional Fourier spectrum.

The wavelet transform is one of the most useful methods for the transient signal. This method uses a small wave packet which only contains several wave periods. The transform is performed by convoluting integral between the wave packed and the signal. When the structures are in correlation between wavelet packet and the signal, the wavelet transform has high value. By time sliding the wavelet packet, the wavelet can analyze the time series that contain non-stationary frequencies or multi-scale structures.

This work presents the methods to quantify the statistical properties of the spectra by using the test signals. As an example of the analysis, the MIR signals obtained in TPE-RX are used. This work is organized as follows. Section 4.2 introduces the fast Fourier transform (FFT) analysis method and the effects of ensemble average on the noise reduction in the spectrum. In section 4.3, the cross correlation analyses based on Fourier transform are presented. Wavelet analysis is explained in section 4.4. Section 4.5 shows the application of the analysis to the MIR signals. Significant results are as follows: the FFT spectrum with ensemble average technique has been quantitatively analyzed to reduce the noise; the wavelet analysis shows higher time and frequency resolutions and the transient structures are observed.

4.2 Noise reduction in Fourier analysis

Fourier analysis is used to obtain the frequency spectrum and the phase. The Fourier transformation $X(\omega)$ of signal $x(t)$ is given by

$$X(\omega, t) = \int_{t-\Delta t}^{t+\Delta t} w(t')x(t')e^{-j\omega t'}dt' \tag{4.1}$$

where $w(t)$ is the Hanning window function, which is used to reduce the leakage of the sideband. The short time FFT analysis is used to analyze the time evolution of the spectrum.

In many situations the signal from plasma contains random noise. Sometimes its amplitude in the frequency domain is higher than the signal that we are interested in. This may submerge the useful information. By using the ensemble average technique in the frequency domain, the amplitude of the random fluctuations has an average power level in all frequency range. The ensemble average has less influence on the mode whose amplitude doesn't change in the ensemble time.

By using a test parameter composed of a sinusoidal wave and a random function, it is used to show the qualitative effect of the noise on signal in the frequency spectrum. In this work, the definitions of the signal to noise (S/N) ratio in the time and frequency domain are illustrated in figure 4.1 (a) and (b), respectively. They are defined as the amplitude ratio between the test signal and the random noise. Figure 4.1 (c) shows the ratio between the absolute amplitude of the Fourier component at the frequency of the test signal and the amplitude of noise in frequency domain versus S/N ratio in time domain. Therefore, the y-axis can be called the S/N ratio in frequency domain. The FFT time window is fixed to 2 ms. Here, the black solid line denotes the ratio without average and the others are that with different ensemble numbers. The S/N ratio in frequency domain is increased with the ensemble number (N). Larger ensemble number is suggested for lower S/N signal.

Figure 4.1 (d) shows the relative ratio between S/N in frequency domain and S/N in time domain versus ensemble number. The ratio changes greatly with the time window, but not with the signal frequency. The time window reflects the frequency broadening. It implies that the frequency broadening affects the present S/N. The ratio is decreased as the frequency width is decreased. It becomes saturated as the ensemble number is larger than 100. Therefore, the improvement by ensemble average on noise reduction becomes weak at larger ensemble number. That is to say, the noise reduction is not improved very much even with large ensemble number. The best way is to improve the signal to noise ratio in the signal. The saturated threshold of the ensemble average with long time window is smaller than that of short time window. If the S/N ratio is lower than 1%, it is difficult to obtain the spectral peak even with large ensemble number.

Here, we assume 1.5 (S/N in frequency domain) as the discriminating level of the

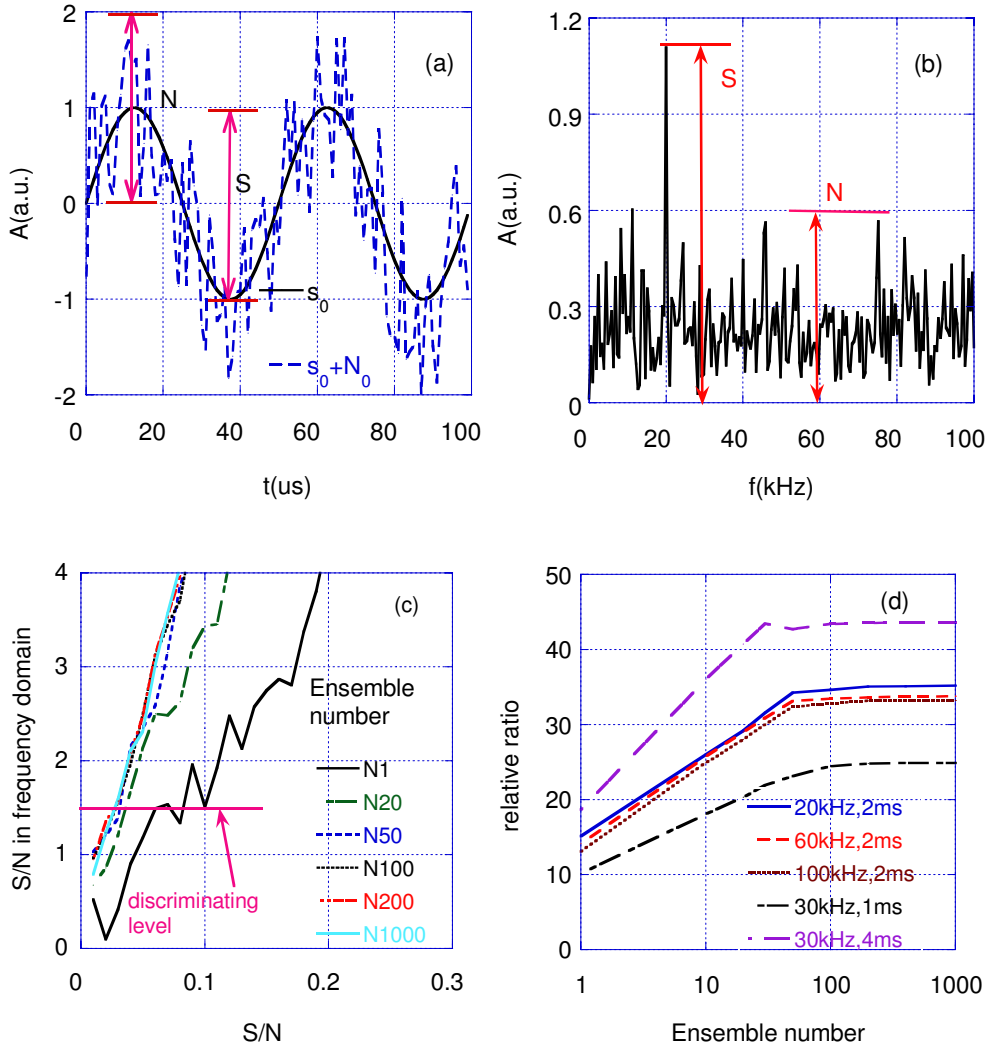

Figure 4.1: Effects of S/N on the FFT spectrum. (a) definition of S/N in time domain (S/N = 1 case), (b) definition of S/N in frequency domain (S/N = 0.1 in time domain), (c) the S/N in frequency domain versus S/N ratio in time domain, here, Y-axis is the ratio between FFT amplitude of the test signal and the maximum amplitude of background fluctuation in frequency domain; (d) The relative ratio between S/N in frequency domain and S/N in time domain as a function of ensemble numbers.

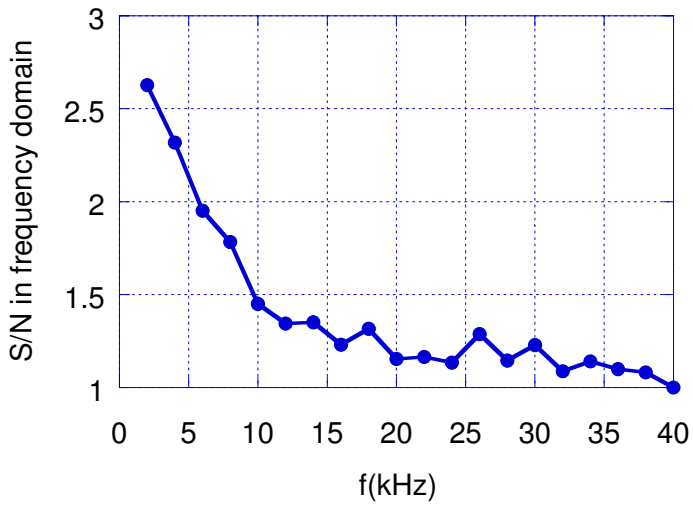

Figure 4.2: The effects of frequency broadening on the S/N ratio (same definition as shown in Fig. 2). x-axis is the full width of the mode packet in the frequency domain. The S/N ratio in time domain is 0.1 and the ensemble number is 200.

FFT spectrum (red horizontal line shown in figure 4.1 (c)). That is, the FFT amplitude of the signal is 1.5 times higher than the maximum amplitude of the noise in frequency domain. By using the ensemble average technique, the value of S/N in time domain is about 0.03, while it is about 0.1 without ensemble average (the time window is 2 ms). Note that, this value mainly depends on the frequency broadening, not on the frequency of the signal. This simulation only shows the qualitative effect of the noise on the periodical signal. For the quantitative estimation, the frequency broadening should be considered in the test model.

Figure 4.2 shows the effects of frequency broadening on the S/N ratio, where x-axis is the full width of the mode packet in the frequency domain. Here, the S/N ratio of 0.1 in time domain and the ensemble number of 200 are used. The S/N ratio decreases as the width of the spectrum increases. This suggests that the S/N value used in this work is sensitive to the frequency broadening.

Although the ensemble technique is an effective way to reduce noise, this method requires the lifetime of the mode should be longer than the time window of FFT. Otherwise, the signal might be distorted by averaging and new analysis method which has

both high time and high frequency ability should be used, for example wavelet transforms [64–66].

4.3 Cross correlation analysis

The cross-power spectral analysis is used to identify the two time series which have the similar spectral properties. The cross-power spectrum between two time series $x(t)$ and $y(t)$ is defined as

$$G_{xy} = Y(\omega)X(\omega)^* \tag{4.2}$$

here the asterisk $(*)$ denotes the complex conjugate. $X(\omega)$ and $Y(\omega)$ is the discrete Fourier transforms of the time series $x(t)$ and $y(t)$, respectively. The phase shift between two time series is given by

$$\Phi_{xy}(\omega) = \arctan\{\frac{Im[G_{xy}(\omega)]}{Re[G_{xy}(\omega)]}\} \tag{4.3}$$

In order to obtain the phase shift whose value corresponds to a high correlation in the frequency domain, the coherence spectrum is introduced and it is defined by the cross-power spectrum normalized by the total power, as

$$\gamma_{xy}(\omega) = \frac{|< G_{xy}(\omega) >|}{\sqrt{< G_{xx}(\omega) >< G_{yy}(\omega) >}} \tag{4.4}$$

where the bracket $(<>)$ denotes ensemble average. The coherency is bounded between 0 and 1, and high value corresponds to high correlation, zero represents completely uncorrelated. The statistical confident level of coherence spectrum is determined by the number of the independent time series $(1/\sqrt{N})$.

The phase-frequency spectrum can show the phase shift of a certain frequency between two signals in a 2D plot. The spectrum is obtained by the two-point cross-correlation method.

$$S(\Phi, \omega) =< |G_{xy}(\omega)|\delta(\Phi_{xy}(\omega) - \Phi) > \tag{4.5}$$

In the calculation the delta function is replaced by a rectangular window. The width of the window depends on the number of the discrete sections in the value range of $\Phi_{xy}(\omega)$. Substituting the wavenumber $k_{xy}(\omega)$ for the phase shift $\Phi_{xy}(\omega)$ in equation 4.5, the wave number frequency spectrum (dispersion relation of the fluctuation) can be obtained [62].

$$S(k, \omega) = \langle |G_{xy}(\omega)|\delta(k_{xy}(\omega) - k)\rangle \tag{4.6}$$

where, Δ_{xy} is the distance between two detectors. The wavenumber is $k_{xy}(\omega) = \Phi_{xy}(\omega)/\Delta_{xy}$. The phase velocity can be obtained by $v = \omega/k_{xy}(\omega)$. If we substitute the modenumber for phase shift, the modenumber-frequency spectrum can be obtained.

4.4 Wavelet analysis

The wavelet transform of time series is its integration with the local basis functions, i.e. wavelet functions, which can be stretched and translated with flexible resolution in both time and frequency.

$$W(s,t) = \frac{1}{\sqrt{s}} \int_{T-\Delta t}^{T+\Delta t} x(t')\Psi^*(\frac{t'-t}{s})dt' \tag{4.7}$$

where s is the scale parameter and t is the time translation parameter, asterisk $(*)$ denotes the complex conjugate, $\Psi(s,t)$ is the wavelet mother function. We use Morlet wavelet function because it has a good balance between time and frequency localization. Furthermore, complex Morlet wavelet analysis preserves the phase information that is very important for the cross correlation analysis. The Morlet wavelet is a continuous transform. One can select any time scales s (or frequencies) in the wavelet transform. It is very convenient for some analyses which need frequency selection rules, for example the wavelet bicoherence (see chapter 6). The complex Morlet wavelet waveform is a sinusoidal wave with a Gaussian envelope, defined as

$$\Psi(s,t) = \sqrt{s}\exp[i\omega_0(\frac{t'-t}{s}) - \frac{1}{2}(\frac{t'-t}{sd_0})^2] \tag{4.8}$$

where ω_0 is the dimensionless frequency and t' is the dimensionless time. d_0 is a constant related to the envelope of the Morlet wave packet. The conversion between the time scale and the frequency of Morlet wavelet is given as

$$\frac{1}{f} = \frac{4\pi s}{\omega_0 + \sqrt{2+\omega_0^2}} \tag{4.9}$$

Here we take $d_0 = 1$ and $\omega_0 = 2\pi$ in this study. Therefore, the scale is an approximation of the inverse of the frequency, thus $s \approx 1/f$.

Figure 4.3 shows the waveforms of Morlet wavelet functions (left) and their Fourier transforms (right) with $s = 1$ and $d_0 = 1, 2, 3$ and 20. The Fourier transforms of the Morlet wavelet function have been shown at the right hand side. The black solid line denotes the real part, and the red dotted line denotes the imaginary part. The envelope

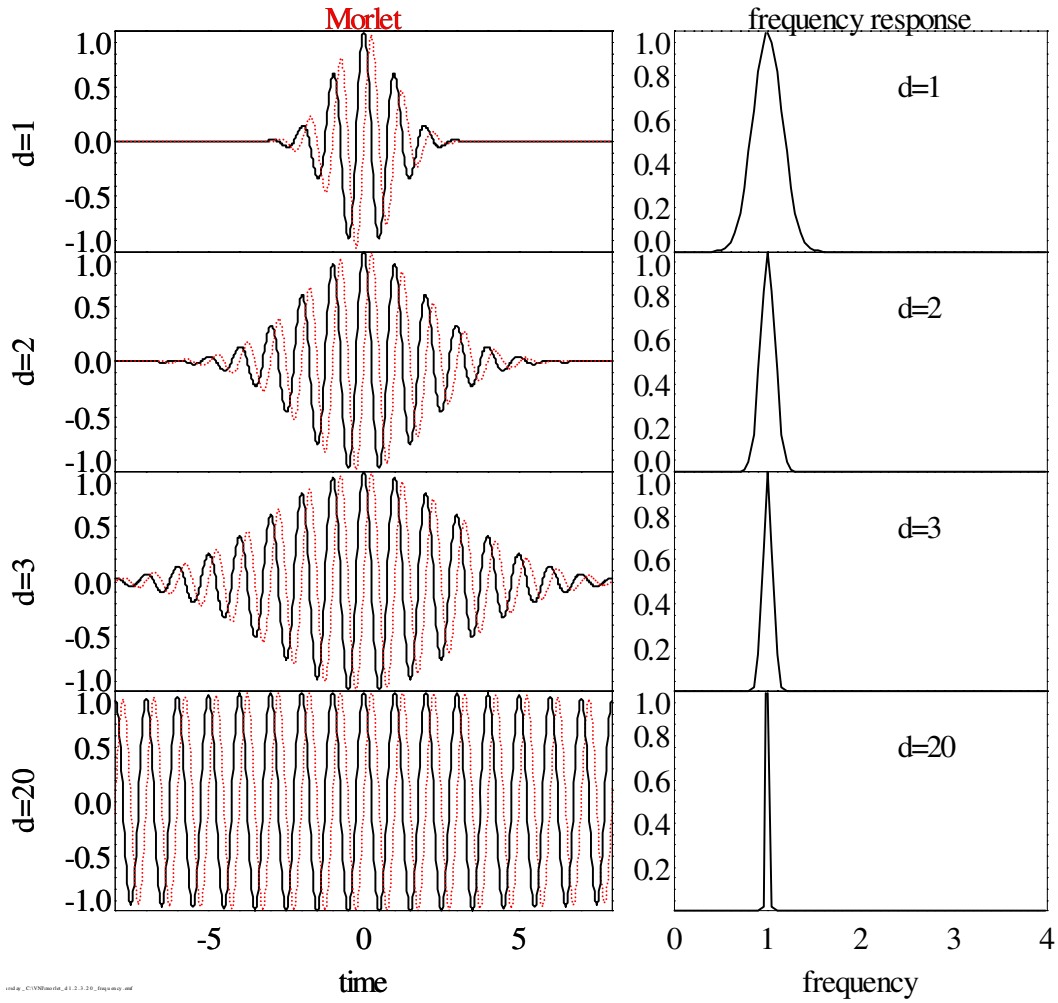

Figure 4.3: The Morlet wavelet functions (d_0 = 1, 2, 3 and 20) and their Fourier transform at $s = 1$.

of the Morlet wavelet function is changing with d_0. As d_0 is decreased, the wave packet becomes small. As d_0 is increased, the wave packet becomes large. The frequency response of the wavelet function is similar to that of a band pass filter. The width of the frequency response is changing with d_0. The small d_0 has the wide frequency response, while the large d_0 has the narrow frequency response. Therefore, in the Morlet wavelet spectrum the time resolution becomes better while the frequency resolution becomes worse as d_0 is decreased. The Morlet wavelet becomes the Fourier transform at very large d_0.

Quantity	Fourier form	Wavelet form
Transform	$X(\omega,t) = \int_{t-\Delta t}^{t+\Delta t} w(t')x(t')e^{-j\omega t'}dt'$	$W(s,t) = \frac{1}{\sqrt{s}}\int_{T-\Delta t}^{T+\Delta t} x(t')\psi^*(\frac{t'-t}{s})dt'$
Cross-transform	$G_{xy}(\omega) = Y(\omega)X(\omega)^*$	$W_{xy}(s) = W_x(s)W_y(s)^*$
Coherence	$\gamma_{xy}(\omega) = \frac{\lvert< G_{xy}(\omega) >\rvert}{\sqrt{< G_{xx}(\omega) >< G_{yy}(\omega) >}}$	$\gamma_{xy}(s) = \frac{\lvert< W_{xy}(s) >\rvert}{\sqrt{<\lvert W_{xx}(s)\rvert><\lvert W_{yy}(s)\rvert>}}$
Phase difference	$\Phi_{xy}(\omega) = \tan^{-1}\left\{\frac{\mathrm{Im}[G_{xy}(\omega)]}{\mathrm{Re}[G_{xy}(\omega)]}\right\}$	$\Phi_{xy}(s) = \tan^{-1}\left\{\frac{\mathrm{Im}[W_{xy}(s)]}{\mathrm{Re}[W_{xy}(s)]}\right\}$
Bispectrum	$B(\omega_1,\omega_2) = X(\omega_1)Y(\omega_2)Z^*(\omega)$ $\omega = \omega_1 + \omega_2$	$B(s_1,s_2) = W_x(s_1)W_y(s_2)W_z^*(s)$ $1/s = 1/s_1 + 1/s_2$
Bicoherence	$b^2(\omega) = \frac{\lvert< B(\omega_1,\omega_2) >\rvert^2}{<\lvert X(\omega_1)Y(\omega_2)\rvert^2><\lvert Z(\omega)\rvert^2>}$	$b^2(s) = \frac{\lvert< B(s_1,s_2) >\rvert^2}{<\lvert W_x(s_1)W_y(s_2)\rvert^2><\lvert W_z(s)\rvert^2>}$

Table 4.1: Comparison of equations used in Wavelet and Fourier analysis

The calculations of Wavelet transform can be performed as a convolution which is considerably faster in frequency domain.

$$W(s,t) = \widehat{F}^{-1}[X(\omega)\Psi(\omega)] \tag{4.10}$$

where $X(\omega)$ and $\Psi(\omega)$ are the Fourier transforms of the time series $x(t)$ and the Morlet wavelet function, respectively. $\widehat{F}^{-1}$ represents the inverse Fourier transform. Based

on the similar definitions described in the previous section, the cross wavelet spectrum, wavelet coherence, the phase difference and the wavelet bispectrum can be obtained. The comparisons of the equations used in wavelet analysis and Fourier analysis are shown in table 4.1 [66; 67].

4.5 Analysis results

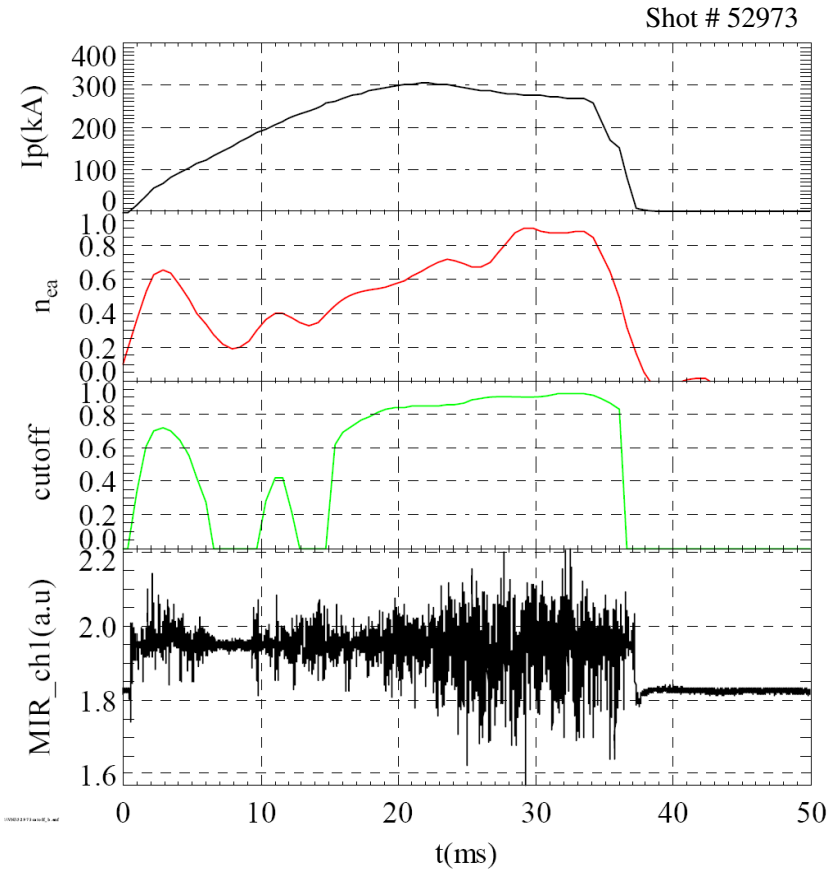

Figure 4.4: Time evolution of the plasma parameters and the MIR signal in TPE-RX

The Fourier spectrum is obtained by integrating $e^{-j\omega t}$ over the time series within a time window. It is difficult to distinguish the mode which changes in the Fourier integration time. If we shrink the time window, the frequency resolution becomes worse. Wavelet analysis can reveal the fluctuation structures at any scales in correlation with

high time resolution. This is advantageous to analyze the turbulence, especially for the intermittent fluctuations.

As an example of the wavelet analysis, we will present an analysis of one shot (#52973, PPCD plasma) in TPE-RX. The details of the experiment have been presented in chapter 2. Figure 4.4 shows the time evolution of the plasma parameters and the MIR signal (ch1, #52973). They are the plasma current I_p, the line-averaged density n_{ea}, the cutoff radius and MIR signal from top to bottom. Here, the amplitude signal is used. The fluctuation of the MIR signal is increased when there is cutoff surface in plasma. The cutoff radius is about $0.8 \sim 0.9$ (normalized by the minor radius of $a = 45$ cm) during flat top of the plasma current. This region is close to the reversed field surface and the fluctuation is strong and changed rapidly [24; 68].

To further understand the difference between the Fourier analysis and the wavelet analysis, the toroidal cross power spectra by FFT and wavelet transforms are compared in figure 4.5. A band pass filter with the frequency range of 5 kHz $\sim$ 50 kHz is used. The time window of FFT transform is 0.25 ms and frequency resolution is 4 kHz. Therefore it is difficult to get the mode which changes faster than 250 μs. In the wavelet spectrum, many small time structures with the time duration shorter than 0.2 ms appear in the high frequency range. It suggests that the RFP turbulence is short-lived fluctuations. The high frequency modes have shorter duration.

Fourier transform has a fixed time resolution. We can't distinguish the frequency which changes within the Fourier time. The spectrum may be transverse elongated by the integration in the range of time window. For example, the fluctuation between 30 $\sim$ 35 kHz from 26.4 ms to 26.7 ms is changing both in frequency and amplitude, but it has the same frequency and amplitude in Fourier spectrum. Comparing FFT and wavelet spectra between 26.5 ms and 27.6 ms, the frequency evolution between 7 $\sim$ 10 kHz in the FFT is less clear than that in wavelet analysis. Therefore, wavelet transform can give good time resolution for high frequency events and good frequency resolution for low frequency events. It is sensitive to the transient fluctuation.

Since Morlet wavelet has the waveform of a sinusoid with the Gaussian envelope, it may fail in tracking the very sharp pulses. In this case, the complex Paul wavelet function may be an adequate one [65]. On the other hand, Morlet wavelet may fail in tracking the high frequency components due to the interference of the low frequency components. This problem can be solved by changing the time and frequency resolutions

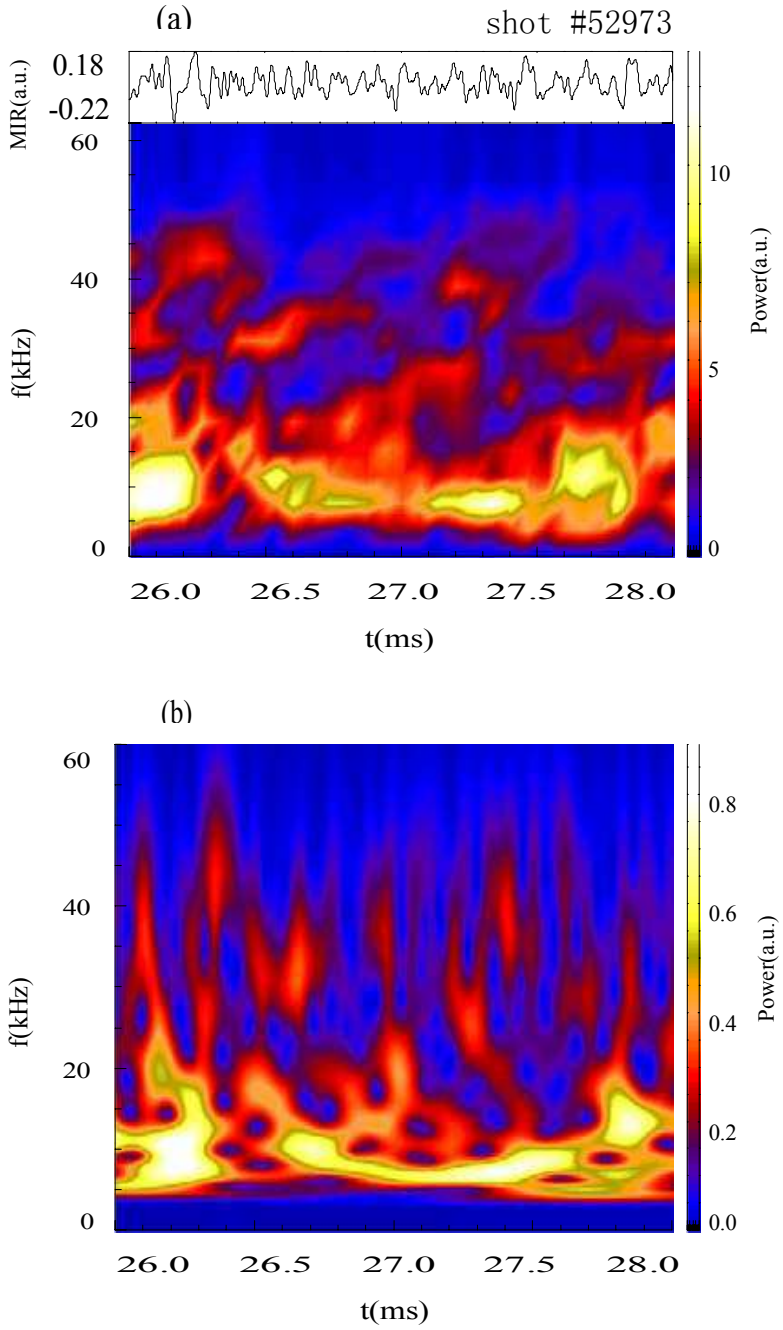

Figure 4.5: (a) Contour plot of the toroidal cross power spectrum $|G_{xy}(\omega, t)|$, (b) Toroidal cross wavelet spectrum $|W_a(s,t)W_b^*(s,t)|$.

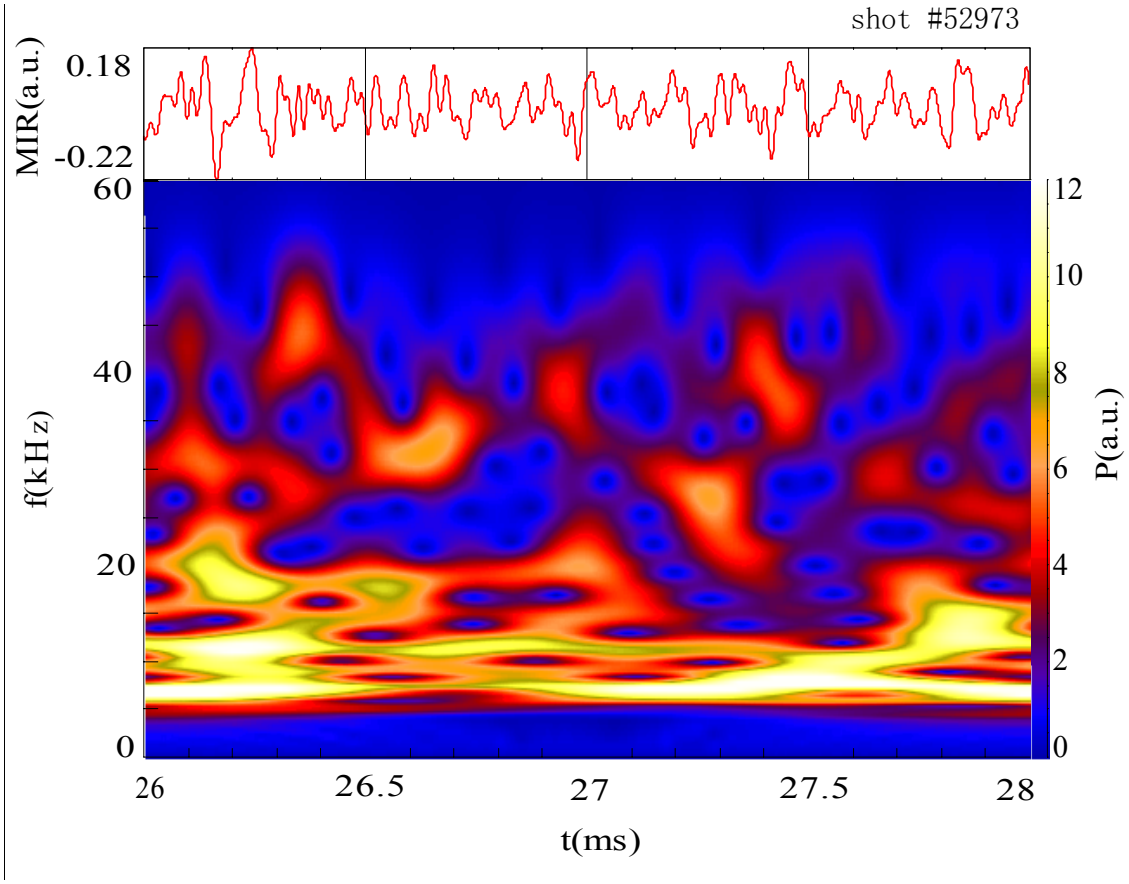

Figure 4.6: Contour plot of the toroidal cross wavelet spectrum with $d_0 = 2.0$

(by adjusting the parameter d_0 in the equation 4.8) or using a high pass filter. Figure 4.6 shows the contour plot of the toroidal cross wavelet spectrum $|W_a(s,t)W_b^*(s,t)|$ with $d_0 = 2.0$. Here the same signal in figure 4.5 is used. We can find that the frequency resolution in the high frequency range becomes better while the time resolution becomes poor. To obtain the high frequency resolution in the high frequency range and the high time resolution in the low frequency range, We can change the d_0 with different time scales (frequencies), as a small d_0 in the low frequency range, and a large d_0 in the high frequency range.

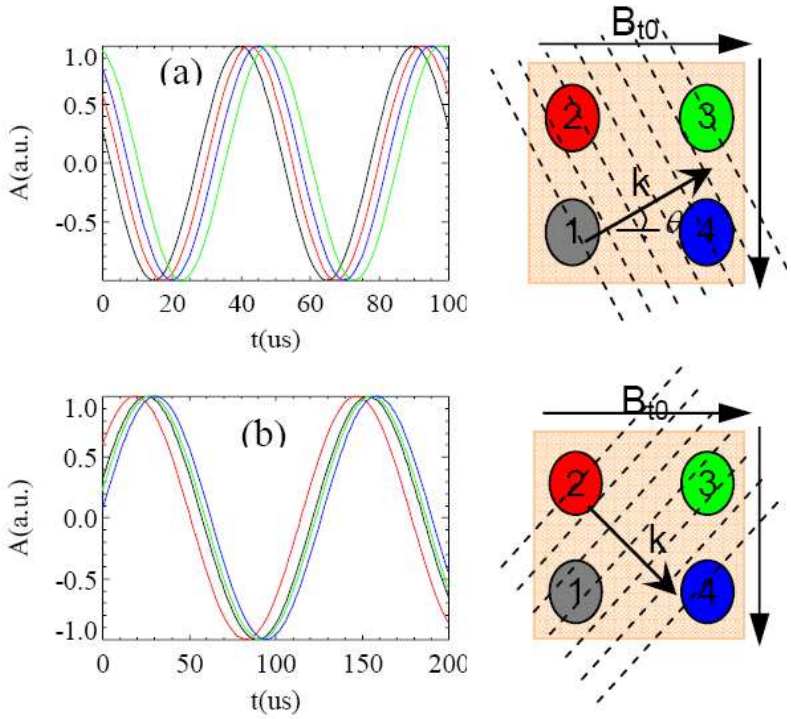

Figure 4.7: (a) The waveforms of 20 kHz fluctuations and its propagation direction at $t = 27$ ms. (b) The waveforms of 8 kHz fluctuations and its propagation direction at $t = 27 - 27.5$ ms.

Since MIR has a 2D detector array, we can select the mode by the wavelet spectrum. By comparing the phase difference, the propagation of the wave can be obtained. Figure 4.7 (a) shows the waveforms of 20 kHz fluctuations and its propagation direction at $t = 27$ ms by the plane wave assumption. Where, the waveforms are reconstructed from the frequency and the phase obtained by using the Fourier analysis. The amplitude is normalized. Since the phase difference is almost the same between the neighboring

channels, the wave number is $k = 17$ m^{-1} and $\theta = 0.46$ rad. Therefore, the poloidal and the toroidal wave numbers are $k_p = 7.5$ m^{-1} and $k_t = 15$ m^{-1}, respectively. The mode number is $m/n = 3/25$. The phase velocity is $\omega/k = 8$ kms^{-1}. Figure 4.7 (b) shows the waveforms of 8 kHz fluctuations and its propagation direction between $t = 27$ ms and 27.5 ms. The wave-number is $k = 10$ m^{-1}, the mode number is $m/n = 2/15$ and phase velocity is $\omega/k = 5$ kms^{-1}.

4.6 Discussions

The analysis of the plasma density fluctuation measured by MIR in TPE-RX has been performed by using the techniques developed in this work. The ensemble technique has been developed to reduce the noise effect in the spectrum analysis. By using this technique, the statistical property of the fluctuations is obtained more accurately than a single data. The mode numbers are obtained by the cross correlation technique. The wavelet analysis has higher time and frequency resolutions, and the evolution of the small time scale structures is observed.

The traditional Fourier method integrated over a large time window, it is useful for the periodical signals. However, this method can't compare the waves which changes within the time range of the Fourier transform, especially for the high frequency components. The reason is that the low frequency components are transformed by several waveforms (poor frequency resolution), and the high frequency components are transformed by many waveforms (poor time resolution) by using a fixed Fourier time window. The turbulence usually has a feature of short time scale and the occurrence of the turbulence often has many non-periodic fluctuations. The integration over a large time window in Fourier method may distort the natural features of turbulence. As a result, the intermittent occurrence of the turbulence may be lost.

The definition of the S/N ratio in section 3.2 may be significantly disturbed by the intermittent bursts in the turbulence signal. One possible improvement of this method is that change the definition of the S/N ratio used in this work, for example the ratio between standard deviation. Nevertheless, present work gives the basic diagram of the noise reduction by statistical method.

In wavelet analysis, the time window is changing with the frequency (or time scale). The spectral resolutions are decided by the number of the wave periods in the wavelet

packet. The wavelet spectrum is slightly changing with the wavelet mother function. Therefore, the waveform of the wavelet mother function should be similar to the waveforms of the turbulent signal.

Chapter 5

MEM Analysis of the 2D Turbulence

5.1 Introduction

Analysis of the 2D turbulence is very important because it provides the more accurate information of the turbulence. In the 2D turbulence measurement system, a big size detector array is necessary to measure the fine structures of the turbulent flow. However, the detector size is often smaller than the cross correlation length of the fluctuation in the real experiments. The measured area in plasma is limited by the small window. On the other hand, the turbulent signals are often mixing with long distance correlation and short distance correlation modes, leading to the complicated 2D cross-correlation function. The traditional two-point cross-correlation analysis can't distinguish the multiple modes which have the finite correlation lengths. It is necessary to develop a new numerical method to estimate the turbulent structure from the signals measured by the small size detector array.

In this work, we developed the maximum entropy method (MEM) to analyze the 2D turbulence measured by MIR in TPE-RX [69]. This method is similar to the 2D filter technique. It can estimate the cross correlation outside the detector array through autoregressive arithmetic (the entropy of the spectrum becomes maximum). As a result, the measurement region is extended, and the spectrum resolution is improved. In this

work, the turbulences between the pulsed poloidal current drive (PPCD) and the high Θ plasmas are compared by MEM. The analysis result shows that the PPCD plasma switches off the turbulence. the standard plasma has high turbulence.

5.2 MEM analysis technique

5.2.1 2D cross-correlation

The two-point cross-correlation [62] is a standard analysis method to study the correlation between two fluctuations, given as

$$\Gamma_{ij} =< n_i n_j >= \int_{\Delta t}\int_{\Delta \omega} n_i(\omega,t) n_j^*(\omega,t)\, d\omega dt \tag{5.1}$$

where the asterisk $*$ denotes complex conjugation, $n(\omega,t)$ is the Fourier transform of the time series, i and j represent different channels, $<>$ denotes ensemble averaging. The cross-correlation spectrum array can be obtained by the cross-correlation analysis between the reference channel and every channel in the measured region. Since the averaging is performed over many wave periods in Fourier space, the cross-correlation spectrum should be independent of the spatial position. In this work, we assume the homogenous turbulence is measured by MIR detector array. The two-point cross-correlation spectrum with the same distance and same direction should be same.

Figure 5.1 shows an example of (a) the detector array (the filled circles denote detectors, and the digits denote the detector number) and (b) its cross-correlation array (the digits in the brackets denote the number of cross-correlation, X denotes no cross-correlation). Six detectors are arranged in a (4×2) array (missed two detectors). To decrease the error, the cross-correlation array is averaged over cross-correlation spectra with the same distance and same direction. x-axis and y-axis in figure 5.1(b) represent the distance between two detectors, and the digits in the brackets denote the number of the cross-correlation in the same distance and same direction. For example, the digit 6 at the center represents the autocorrelation between six detectors themselves. The digit 4 at the right hand side denotes the cross correlation of the channel pair: (4,3), (3,2), (2,1) and (6,5). (4,3) denotes the cross correlation between channel 4 and channel 3. The digit 2 at the right hand side denotes the correlation of the channel pair: (4,2) and

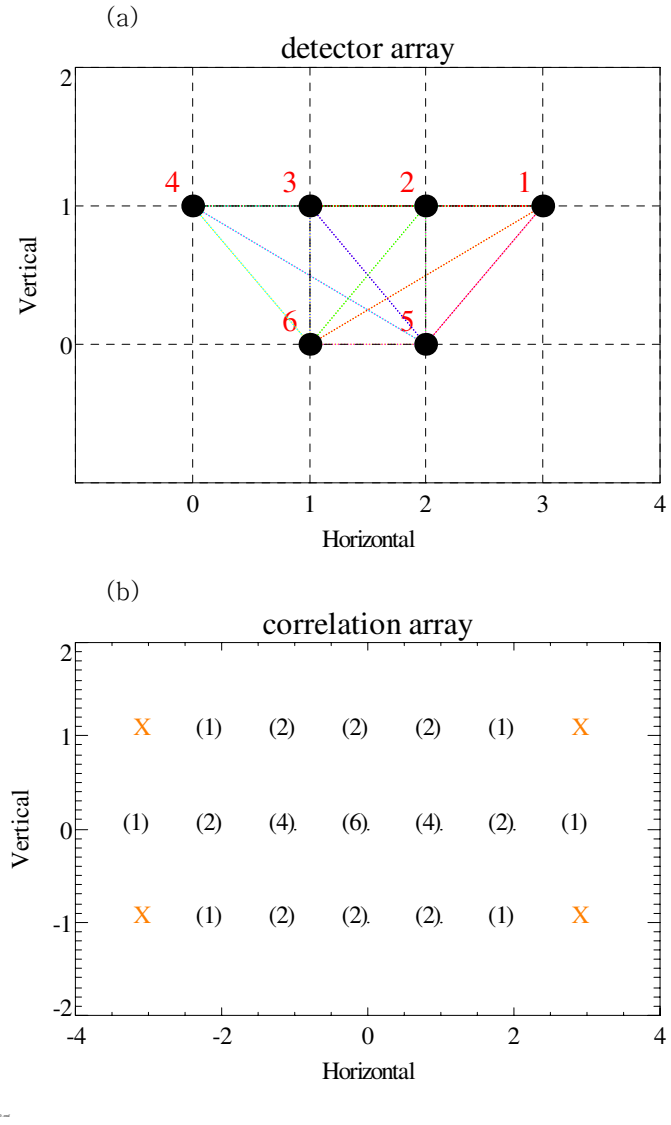

Figure 5.1: Schematic diagram of the autocorrelation function by a (4×2) detector array. (a) detector array (the digits denote the detector No.), (b) locations of the cross-correlation (the digits in the brackets denote the No. of cross-correlation)

(3,1), while at the left hand side the digit 2 denotes the cross correlation of the channel pair: (2,4) and (1,3).

The cross-correlation spectrum is the inverse Fourier transforms of the power spectrum. According to the Wiener–Khinchin theorem, the power spectrum is the Fourier transform of the corresponding autocorrelation function, defined as

$$S(k_x, k_y) = \int\int \Gamma(x, y) e^{-i(k_x x + k_y y)}\, dxdy \tag{5.2}$$

where, k_x and k_y are the toroidal and the poloidal wavenumbers, respectively. $\Gamma(x, y)$ is the average autocorrelation array which is averaged over different reference channels. The average rule is averaging the cross-correlations of two detectors which have the same direction and distance. $\Gamma(x, y)$ is a complex function. The real part is an even function and the imaginary part is an odd function according to the Fourier theorem.

To test the 2D spectrum, we assume two sinusoidal waves with the wavenumbers of $k_1(k_x = -0.5, k_y = -0.2)$, and $k_2(k_x = 0.3, k_y = 0.1)$ propagating on a (7×7) detector surface simultaneously. Figure 5.2 shows the real and imaginary parts of the autocorrelation array of the test signals. X-axis and y-axis represent the toroidal and poloidal distances between two detectors, respectively. The autocorrelation array has some periodical structures which represent the measured waves. Here, the autocorrelation is normalized by the total power. The real part is symmetric at the zero while the imaginary part is inverse symmetric at the zero. The center of the correlation array is one which represents the coherence of itself. Since the coherence is still high at the edge of the detector region, the detector array size is smaller than the coherence length. The power spectrum calculated by equation 5.2 is broad due to the finite detector size which is smaller than the coherent length.

Figure 5.3 shows the 2D power spectrum $S(k_x, k_y)$ calculated by equation 5.2. Here we use the autocorrelation function shown in figure 5.2. The x-axis and y-axis are the toroidal and the poloidal wavenumbers, respectively. The normal z-axis is used for the spectral power. The green and black colors correspond to the high power. The yellow color denotes the low power. The spectrum has a broad peak with some sidelobes caused by the small detector size. The energy of the low k leaks to the high k. The broad spectrum with the dominant energy might conceal the other modes which have small power density. It shows poor spectral resolution. Therefore, by using standard Fourier method, the location of peak k is unclear due to the imaged region being smaller

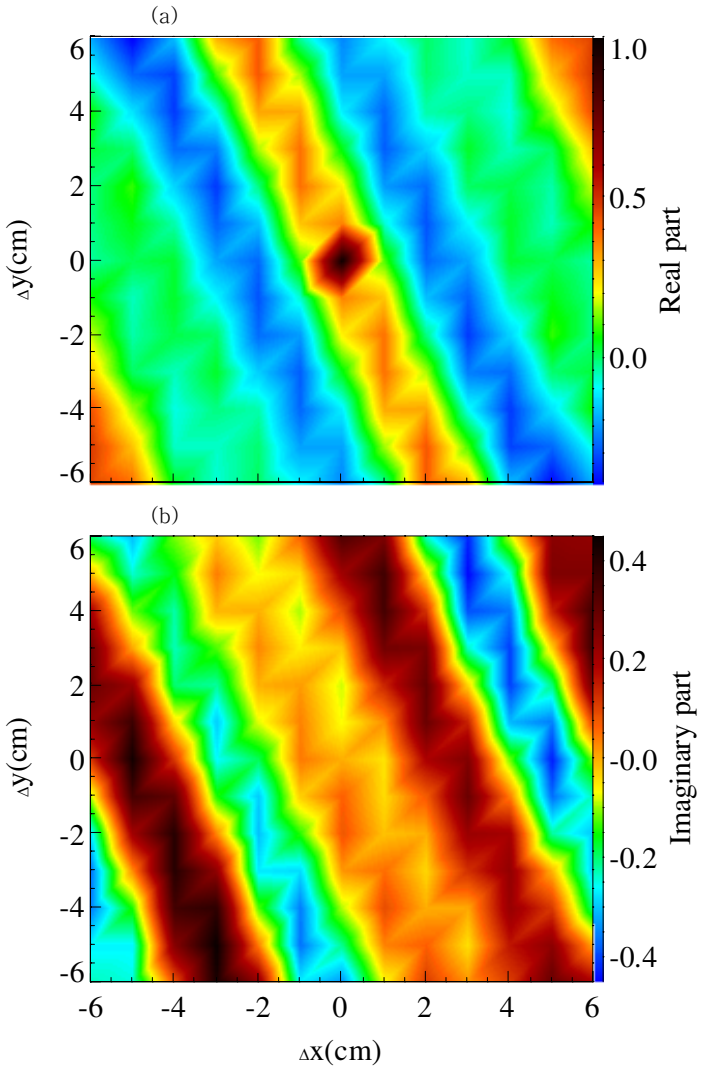

Figure 5.2: The real part (a) and imaginary part (b) of the autocorrelation function.

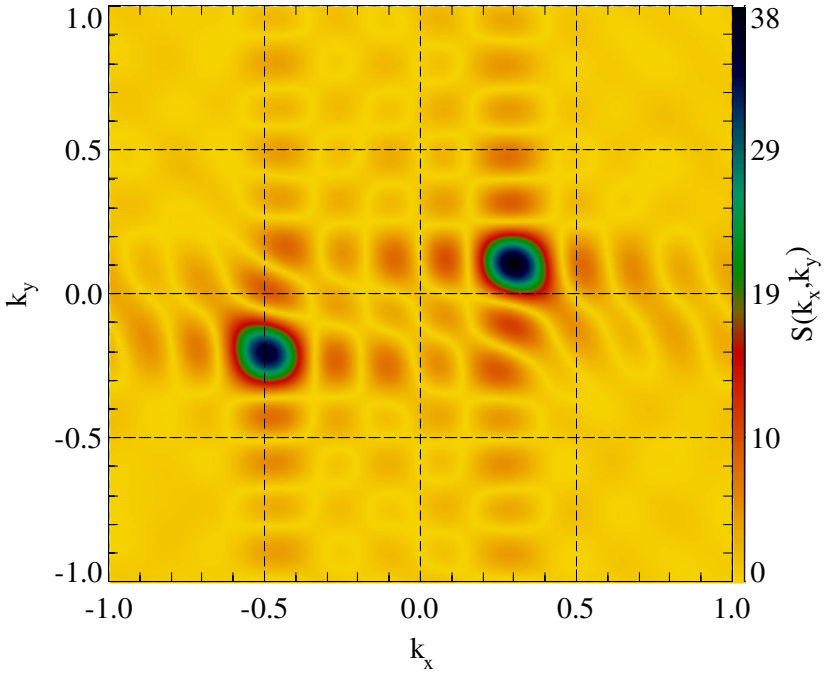

Figure 5.3: The power spectrum $S(k_x, k_y)$ obtained by Fourier transform using the autocorrelation function shown in figure 5.2. The k_x and k_y represent the toroidal and the poloidal wavenumbers, respectively.

than the wave measured. Since the low k leaks to high k, we can't compare when there are a few simultaneous propagating modes.

5.2.2 MEM analysis

The power spectrum estimated by the Fourier transform is similar to a spatial band pass filter in the autocorrelation function. If one can extend the correlation outside the measured region, the power spectrum with high resolution can be restored. One possible way is trying to find the filter coefficients by autoregressive method. However, the result is sensitive to the noise and is not very reliable sometimes. It may cause spurious peaks if we fail to set the convergence condition and fail to select the optimized order of the autoregressive filter. So far, many numerical methods such as autoregressive, maximum likelihood method (MLM) and Pisarenko methods have been used to the power spectral estimation [70–72]. Among them, 2D MEM is the most powerful and effective method [73]. This technique allows us to fit as many peaks to the k spectrum as there are unique values of cross-correlation points. As a result, the location of peak k becomes clear especially when the imaged region is smaller than the wave measured.

The difference between the FFT and the MEM analysis methods are shown in figure 5.4. The red dot line represents the measured cross-correlation. Here, we assume the width of the window is w. Since the broadening of the power spectrum is proportional to $1/w$, a broad spectrum with energy leakage is observed by FFT. In the MEM analysis, the cross correlation range is extended, and the peak spectrum is obtained if there are some waves in the cross correlation array.

In this work, the Skilling MEM is used [73], because it is a model-free method which can give the more reliable results than the other MEM algorithms, for example the method based on the autoregressive model. The entropy is defined as

$$H(S) = \int\int \log(S(k_x, k_y))\, dk_x dk_y \tag{5.3}$$

Define the constrained statistic, chi-squared, to estimate the misfit between the experimental value and expectation value, as

$$\begin{aligned} C(S) &= \chi^2(S) - \chi^2_{tar.} \\ &= \sum_{i=1}^{N_{ch}} (\Gamma_{meas.} - \Gamma_{aim})^2/\sigma^2 - \chi^2_{tar.} \end{aligned} \tag{5.4}$$

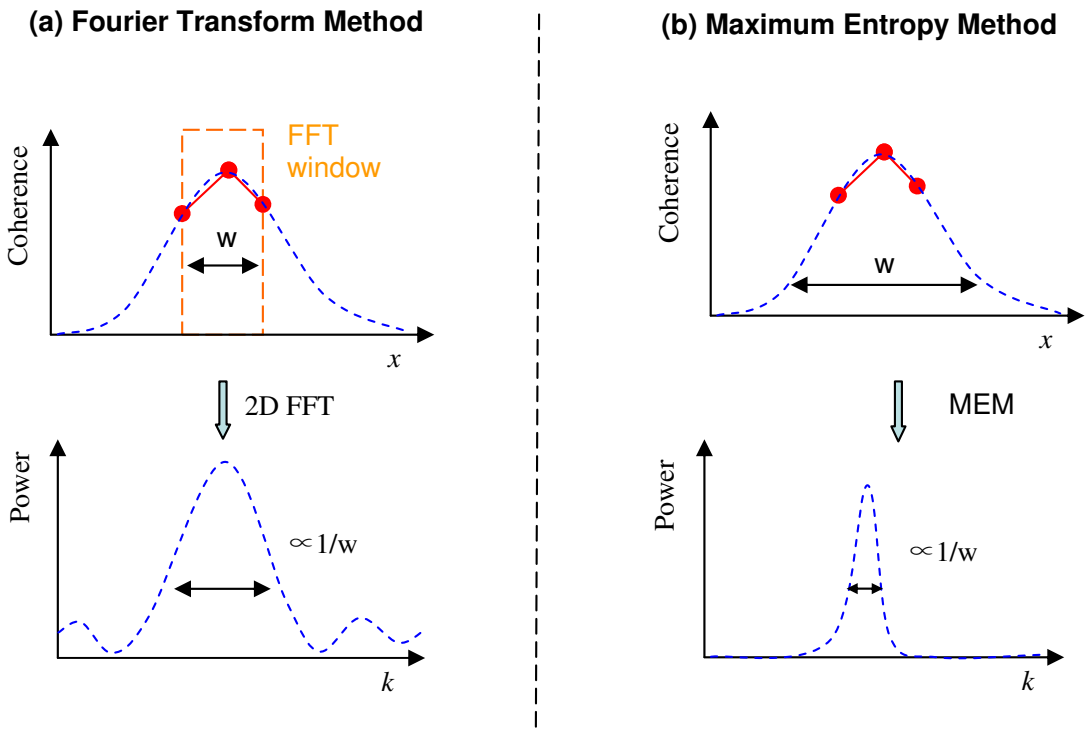

Figure 5.4: Comparison of the k spectrum estimation between (a) Fourier analysis and (b) MEM

The entropy is changed to solve the following equation in maximum

$$P(S) = H(S) - \lambda C(S) \tag{5.5}$$

under the constraint of $C \to 0$. Here λ is the Lagrange multiplier. $\Gamma_{meas.}$ is the 2D autocorrelation function given by eq. 5.1. Γ_{aim} is the autocorrelation function estimated by MEM. σ is the standard error of $\Gamma_{meas.}$. $\chi_{tar.}$ is the target to converge maximum of eq. 5.5 within reasonable calculation time. The maximum condition is satisfied when $\Gamma_{meas.} = \Gamma_{aim}$ and it is possible for the 1D MEM. However, the maximization process of eq. 5.5 in 2D array requires non-linear optimization. $\chi_{tar.}$ should be equal to channel number but it is determined empirically for good convergence. This problem is solved iteratively by searching for maximum entropy over three well chosen search directions. The details of the calculation are described in ref. [71–74].

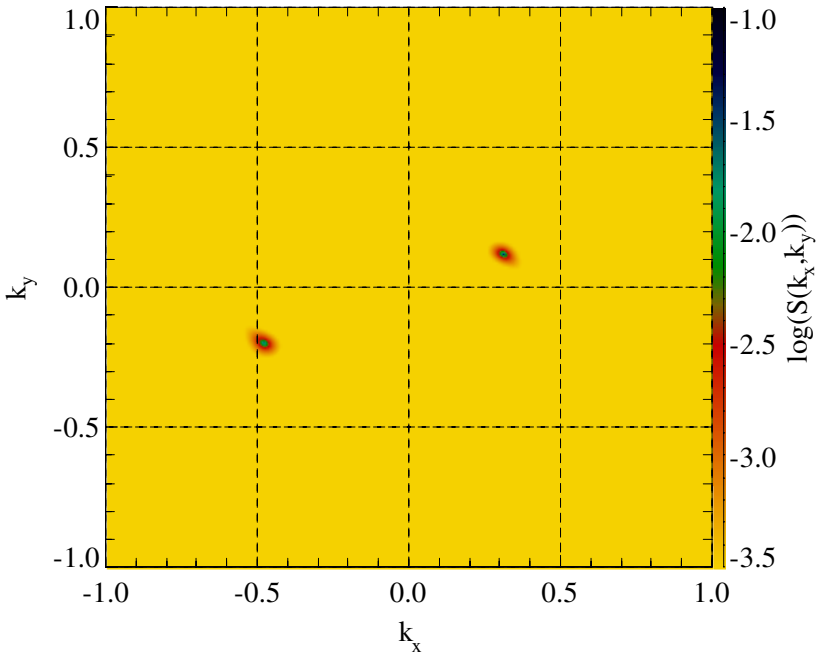

Figure 5.5: The power spectrum $\log(S(k_x, k_y))$ of the PPCD plasma obtained by MEM using the autocorrelation function shown in figure 5.2. The k_x and k_y are the toroidal and the poloidal wavenumbers, respectively.

Figure 5.5 shows the 2D power spectrum $\log S(k_x, k_y)$ estimated by MEM by using the autocorrelation array shown in figure 5.2. Note that the logarithm z-axis is used.

The peaks in the power spectrum are much higher than the background fluctuations. In contrast with the standard 2D Fourier method, the sidelobes are very small and the locations of the peak k become clear. The spectral peaks at $k_1(k_x = -0.5, k_y = -0.2)$, and $k_2(k_x = 0.3, k_y = 0.1)$ agree with the wavenumbers in the test signals. Therefore, the MEM analysis may reduce the spectrum broadening and provides a clear peak k-spectrum.

5.3 Analysis of the RFP turbulence

The standard RFP configuration is generated by the relaxation process and sustained by the dynamo activities, which are driven by the turbulences and instabilities. The RFP plasma can also be sustained by PPCD operation. The mechanisms of dynamo have been investigated intensively [29; 75]. The nonlinear MHD model is widely used to explain the dynamo mechanism. This model assumes that the fluctuation-induced electromotive electric field sustains the field aligned current against resistive decay. The Ohm's law can be written as [75]

$$\eta j_{\parallel} = E_{\parallel} + < \widetilde{v} \times \widetilde{B} >_{\parallel} \tag{5.6}$$

where, η is the electric resistivity. $j_{\parallel}$ is the parallel equilibrium current, $\tilde{v}$, $\tilde{B}$ are the fluctuating fluid velocity and the magnetic field, respectively. <> denotes the average over an equilibrium flux surface. $< \widetilde{v} \times \widetilde{B} >_{\parallel}$ represents the electromotive force. $E_{\parallel}$ is the external electric field parallel to the magnetic field which is generated by PPCD (In the edge region, the magnetic field is poloidal in the RFP).

The standard plasmas includes low Θ and high Θ plasmas. Both of them are sustained by dynamo related fluctuations. Here, the pinch parameter Θ is defined as the ratio of the poloidal magnetic field at the edge to the volume averaged toroidal magnetic field, $\Theta = B_p(a)/ < B_t >$. The high Θ is defined as $\Theta > 1.6$. The fluctuation becomes more coherent and the fluctuation amplitude of the magnetic probe is increased with the Θ. The sawtooth crashes are often observed during high Θ operation [45; 68]. In the PPCD operation, the external $E_{\parallel}$ drives the poloidal current, so that the relaxation state (or Taylor state) is sustained without the help of the dynamo effect. As a result, the dynamo-related fluctuations can be suppressed.

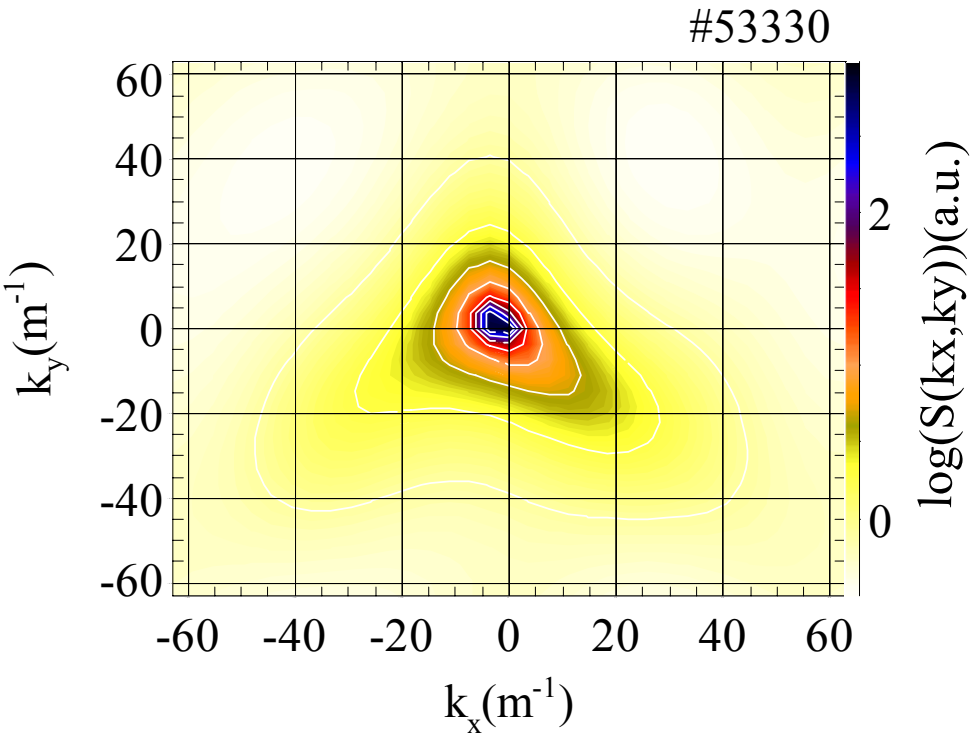

Figure 5.6: The power spectrum $\log(S(k_x, k_y))$ of the PPCD plasma (shot # 53330, $t = 20 - 30$ ms, $f = 93$ kHz) obtained by MEM. The k_x and k_y are the toroidal and the poloidal wavenumbers, respectively.

The turbulences of the PPCD and the high Θ plasmas are compared by the 2D k spectra estimated by MEM. Figure 5.6 shows the power spectrum $\log(S(k_x, k_y))$ of PPCD plasma (shot #53330) obtained by MEM. Where, the black and blue colors correspond to the high power. The white and yellow colors denote the low power. The peaked power is observed at $k_x = -3 \pm 3$ m^{-1} and $k_y = 3 \pm 3$ m^{-1} in the PPCD plasma. Here, the error is defined as the 90% of the spectral power. The mode energy is limited at the low k range which suggests low turbulence in the PPCD plasma. The dominant mode is $m = 1/n = -7$ with the error of $\Delta m = 1/\Delta n = 7$, where m and n are the poloidal and toroidal modenumbers, respectively. This is the quasi-single helicity mode which is often observed in the PPCD plasma in TPE-RX.

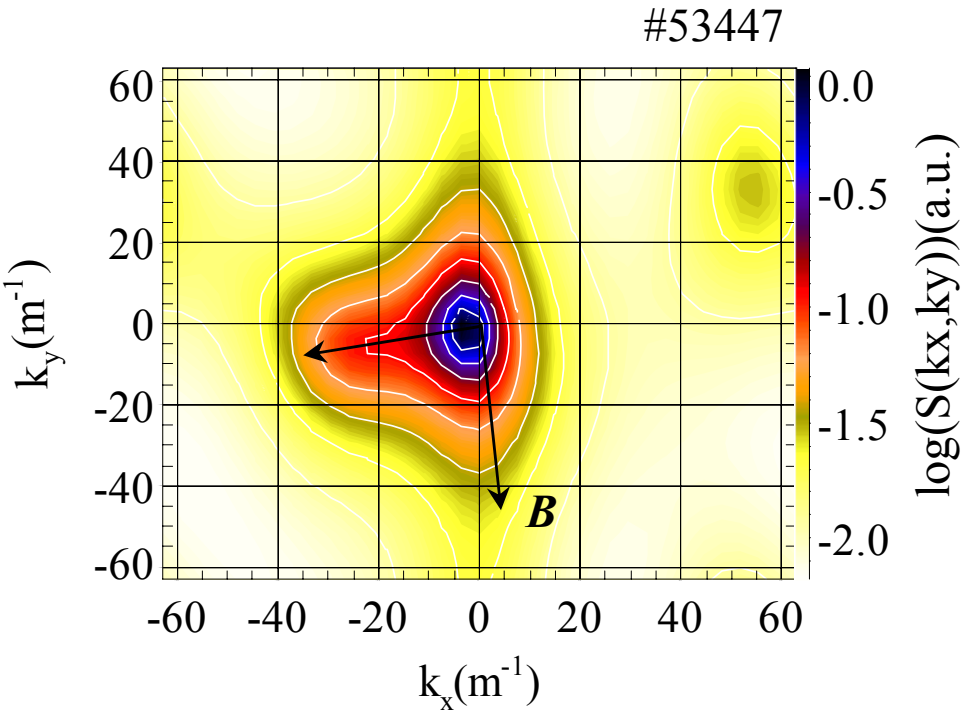

Figure 5.7: The power spectrum $\log(S(k_x, k_y))$ of the high Θ plasma (shot # 53447, $t = 20 - 30$ ms, $f = 109$ kHz) estimated by MEM. The k_x and k_y are the toroidal and the poloidal wavenumbers, respectively.

Figure 5.7 shows the power spectrum $\log(S(k_x, k_y))$ in the high Θ plasma (shot #53447). The cutoff radius is about $r/a = 0.75$. The spectral peak is observed at $k_x = -3 \pm 5$ m^{-1} and $k_y = -3 \pm 6$ m^{-1}. The dominant modes are $m = -1 \pm 2/n = -7 \pm 14$.

It is wider than that of the PPCD plasma. Therefore, the spectrum of high Θ plasma expands to the high k range.

The revered surface can be obtained by the modified Bessel function model [3]. Generally, the reversed field surface is about $r/a = 0.9$ in the standard plasma, while it is about $r/a = 0.8$ in the typical PPCD plasma due to the driving of the external field. In the PPCD plasma, the cutoff surface of MIR is about $r/a = 0.85$ because of the high electron density. MIR may detect the density fluctuation outside of the reversed field surface. In the high Θ plasma, the cutoff surface of MIR is at about $r/a = 0.75$ because of the low electron density. MIR may detect the density fluctuation inside of the reversed field surface. Therefore, the poloidal mode numbers of the PPCD and the high Θ plasmas have different signs.

The evolutions of the tearing modes during the dynamo event have been discussed by using magnetic probes [45; 68]. Those observations show that the multi-modes will be excited during the dynamo event in the high Θ plasma. As shown in figure 5.7, the wide k distribution denotes the presence of multi-modes in the high Θ plasma (The mode analysis is shown in chapter 6).

The turbulence has many active modes. The measured wide k distribution in high Θ plasma suggests the high turbulence. The expansion direction in k spectrum of the high Θ plasma is mainly in toroidal direction which indicates by an arrow shown in figure 5.7. The magnetic field is mainly poloidal near the reversed field surface. The expansion direction is perpendicular to the magnetic field line. It is in the electron drift direction. Therefore, the turbulence in the high Θ plasma propagates in the electron drift direction. The expansion in high k range suggests the strong turbulence in the high Θ plasma. This result agrees with the nonlinear MHD dynamo model.

5.4 Discussions

In this work, turbulences between the PPCD and the high Θ plasmas have been studied by using MEM, which provides high spectral resolution. The low k mode is dominant in the PPCD plasma, while in the high Θ plasma the spectrum is broad which suggests presence of multi-modes in the plasma. The k spectrum of the high Θ plasma expands to the high k range and the turbulence propagates in the electron drift direction. The

preliminary result suggests that the PPCD operation suppresses the turbulence, and the high Θ plasma has strong turbulence. It agrees with the nonlinear MHD dynamo model.

MEM is a new technique to estimate the power spectrum. It allows us to fit as many peaks to the k spectrum as there are unique values of cross-correlation points. As a result, the location of peak k becomes clear especially when the imaged region is smaller than the wave measured. This technique is very useful and can be used in other imaging diagnostics.

Nevertheless, MEM may make artefacts when the signal-to-noise ratio (SNR) is very low, and the detector size is much smaller than the cross-correlation length. Some sorts of numerical checking would be necessary, for example, synthesizing data. To measure the fine structures of the turbulence, the high sensitive detector array with big size and high spatial resolution should be developed.

Chapter 6

Characteristics of Turbulence in RFP Plasma

6.1 Introduction

Although the turbulence theory is well established [76; 77], the turbulence in RFP plasma is hard to study. The main reason is the complicated fluctuations (magnetic and electrostatic) and the high beta operation in RFP plasmas, which may cause the violation of the approximations in turbulence theory. On the other hand, the magnetic and electrostatic fluctuations may highly interact with each other, make the RFP turbulence a very difficult problem.

Experimental study of the RFP turbulence is not sufficient. So far, the turbulence in the RFP plasma has been studied by magnetic probe, Langmuir probe and Gas-puff imaging (GPI) [40; 41]. However they measure the very edge region or obtain the integrated signal. Previous research suggests that the turbulence in the inner area is important for the sustainment of the RFP configuration [75]. The turbulence around the reversed field surface has not been well understood experimentally.

Reflectometry is a powerful tool for turbulence measurement, because it can provide the direct view of the density turbulence localized at the cutoff surface (the reflected signal is sensitive to the motion of the cutoff surface) [1]. In this work, we have developed

a microwave imaging reflectometry (MIR) system for the two-dimensional (2D) local density turbulence measurement in TPE-RX. This is the first demonstration of the turbulence diagnostics by MIR.

There are two types of plasmas in RFP: one is the standard plasma, the other is the PPCD plasma [5; 28]. Here, we define the standard plasma is the plasma without current drive such as PPCD. In the standard operation, the plasma configuration is sustained by the electromotive force generated by fluctuations (dynamo). In the PPCD operation, the plasma configuration is sustained by the external driven field. As a result, the fluctuations may be suppressed in the PPCD operation. Therefore, the study of turbulence between the plasmas with and without PPCD by using MIR may clarify the physics of turbulence in RFP.

In this chapter we will study the turbulence near the reversed-field surface by comparing the plasmas with and without PPCD in TPE-RX [78]. It is organized as follows: Section 6.2 describes the experiments of the plasmas with and without PPCD in TPE-RX. In section 6.3 the features of the fluctuation distribution are presented. Section 6.4 shows the long range cross correlation of the turbulence. Section 6.5 describes the mode analysis by magnetic probes. The 2D k spectra are presented in section 6.6. Section 6.7 describes the correlations of MIR with potential and magnetic signals. In section 6.8, the nonlinear interaction of the turbulence has been analyzed. The relations between the nonlinear interaction and the intermittent structures are discussed in section 6.9.

6.2 Experimental results

Experiments have been performed in the standard and PPCD plasmas in TPE-RX. The experimental parameters with MIR is explained in chapter 2. Figure 6.1 shows the plasma current (I_p), the reversal parameter ($F = B_t(a)/ < B_t >$), soft X-ray (SXR), the line averaged density (n_{ea}), the normalized cutoff radius (r_{cut}), the amplitude signals of MIR and their wavelet spectra in the standard (# 53441, $F \approx -0.5$, $\Theta \approx 1.7$) and PPCD (# 53362) plasmas. During the flattop of the discharge, the plasma current is about 285 kA and 235 kA in the PPCD and standard plasmas, respectively. The PPCD operation starts at 18 ms which causes the rapidly increase in the SXR intensity and the rapidly decrease in the reversal parameter F (because the edge toroidal field $B_t(a)$ is mainly driven by the external field generated by PPCD operation). The SXR intensity

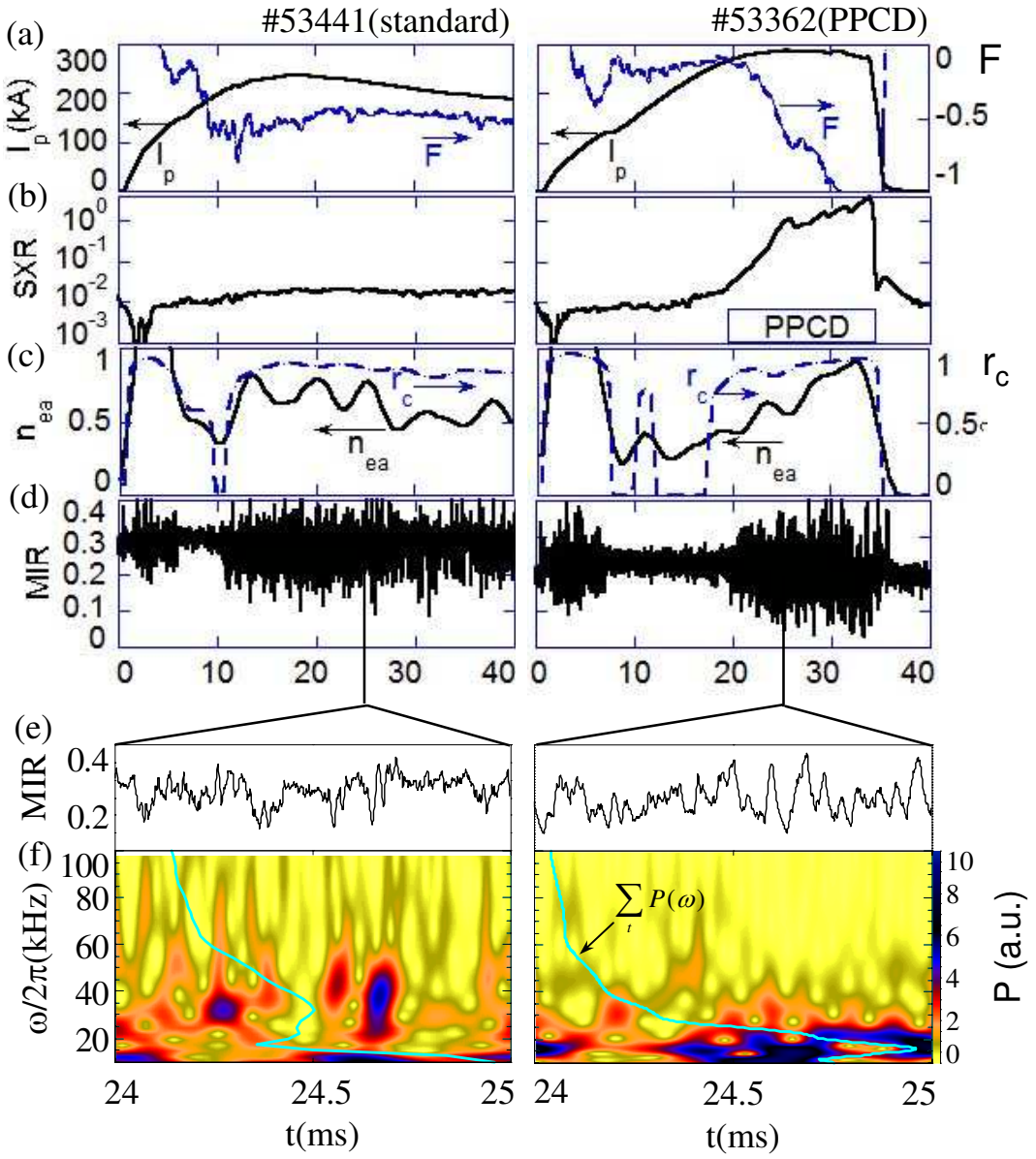

Figure 6.1: Plasma parameters and MIR signals in the standard (left) and the PPCD (right) plasmas in TPE-RX. (a) the plasma current (I_p) and reversal parameter (F), (b) the soft X-ray (SXR), (c) the line averaged density (n_{ea}) and cutoff radius (r_{cut}), (d) (e) the amplitude signal of MIR (ch.4) and (f) wavelet spectrum.

of the PPCD plasma is about 100 times higher than that in the standard plasma. This indicates good confinement with PPCD.

Without PPCD, F is constant during the flattop of the plasma. The normalized cutoff radius r_{cut} is estimated from the density profile measured by the double-chord interferometer [52]. It is about 0.8 during the flattop of the plasma current due to the flat density profile which is often observed in TPE-RX. The fluctuation amplitude is very small if there is no cutoff surface in plasma. The standard and the PPCD plasmas have the same density fluctuation amplitudes near the cutoff $r_{cut} \approx 0.8$. However, their fluctuation structures are different. In the standard plasma, the fluctuation in the amplitude signal is intermittent which bursts mainly in the negative direction, while in the PPCD plasma the fluctuation in the amplitude signal is symmetric. Actually, the plasma (#53441) has a higher Θ ($\Theta \approx 1.7$)(or deeper F, $F \approx -0.5$) than the usual RFP plasma. With low Θ (or narrow F) ($t = 10 - 18$ ms at the right hand side) the SXR is much less than that with PPCD.

Figure 6.2 shows the poloidal magnetic fluctuations (δB_p) in the standard ($F = -0.5$) and the PPCD plasmas. The magnetic fluctuation is measured by the complex edge probe (CEP) which is sensitive to the fast magnetic fluctuations [54]. The magnetic fluctuation is suppressed during PPCD, while in the standard plasma ($F = -0.5$) the magnetic fluctuation amplitude is high. It should be noted that the magnetic fluctuation before PPCD operation is low because of shallow F (or low Θ) ($\Theta = 1.4$, $F = -0.15$). The high magnetic fluctuation at $t = 24 \sim 25$ ms may be caused by the time interval between two PPCD pulses. After switch off the PPCD operation, the strong magnetic fluctuation appears at $t = 34 \sim 35$ ms.

Figure 6.3 shows the magnetic fluctuation as a function of plasma energy ($P = n_{ea}T_e$) in the standard and the PPCD plasmas. Here, n_{ea} is the line averaged density measured by interferometer. The temperature is measured by the Thomson scattering (one data at about 30 ms in one discharge). The magnetic fluctuation ($\widetilde{B_t}$) is obtained by the complex edge probe (CEP). The PPCD plasma has high pressure and low magnetic fluctuation. The magnetic fluctuation during PPCD plasma is about 0.5%. The standard plasma ($F = -0.5$) has low pressure and high magnetic fluctuation. The magnetic fluctuation of the standard plasma is up to 2.5%. The plasma pressure in the PPCD plasma is about 5 times higher than the standard plasma ($F = -0.5$). Although the magnetic fluctuation has been suppressed in the PPCD plasma, it is much higher than that in tokomak and stellarator (typically $< 0.1\%$).

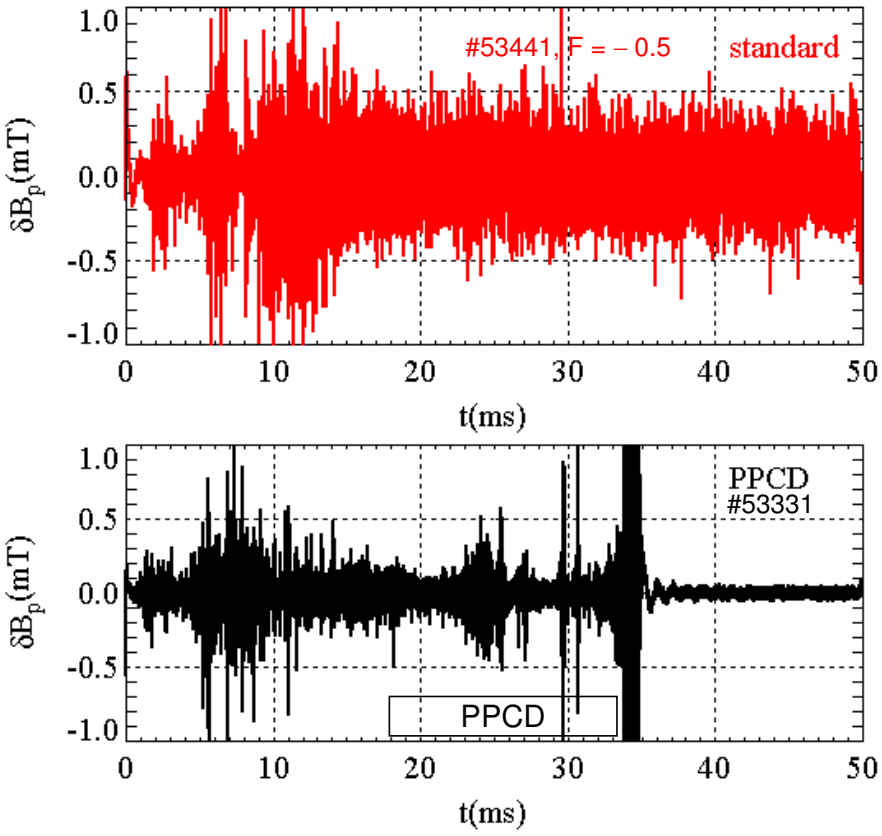

Figure 6.2: Time evolution of the poloidal magnetic field in the standard (top, $F = -0.5$) and the PPCD (bottom) plasmas

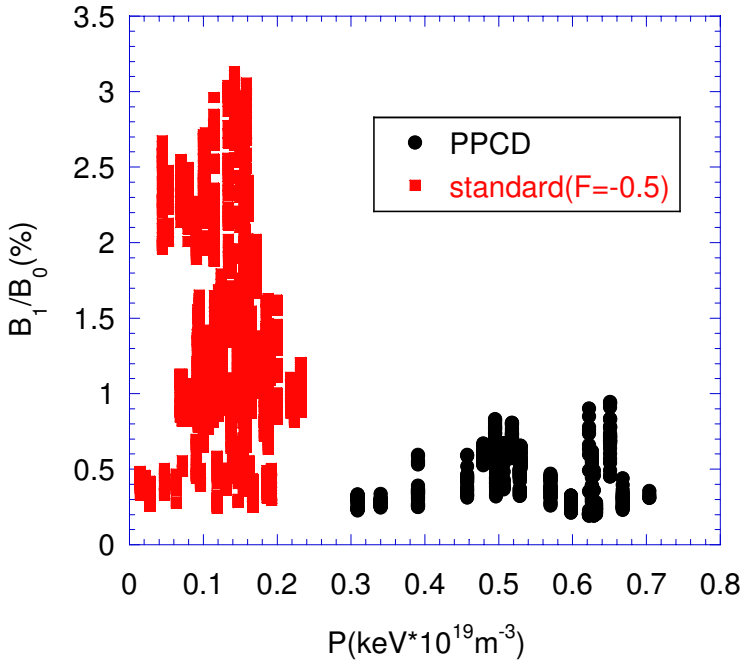

Figure 6.3: The toroidal magnetic fluctuation as a function of the plasma energy ($P = n_{ea}T_e$)

As discussed in chapter 4, the traditional Fourier method is not suitable to analyze the intermittent signals. Here, we use wavelet transform because it is a powerful tool to analyze the intermittent signals [79; 80]. Figure 6.1 (f) shows the wavelet spectra of the amplitude signals. The summed powers $\sum P(\omega)$ are also shown. Here, the black and blue colors represent high power. The yellow color represents low power. In standard plasma the spectrum has some high discrete power at about $20 \sim 60$ kHz, which corresponds to the intermittent bursts in MIR signal. There are many short-lived fluctuations (< 0.1 ms) in the high frequency range. As a result, the summed power is increased in the high frequency range. In PPCD plasma the high frequency fluctuations have been suppressed, and the spectrum is dominated by a single frequency ($\sim 15 - 20$ kHz) which corresponds to the sinusoidal-like fluctuation in the the signal.

6.3 Fluctuation distribution

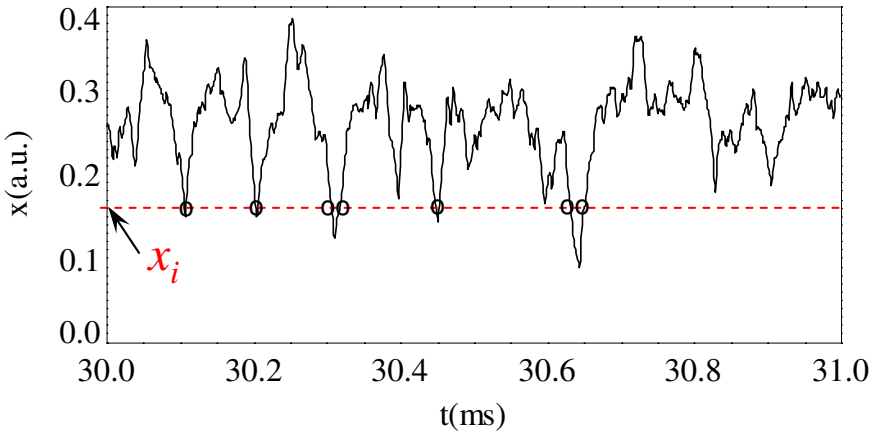

Figure 6.4: Definition of the probability distribution function (PDF)

The fluctuating quantities of the quasi-stationary turbulence can be characterized by the probability distribution function (PDF). It is defined as

$$D(x_i) = n_i/N_0 \tag{6.1}$$

where, n_i is the data number at value x_i in the data series $x(t)$, N_0 is the total data number. The definition of the PDF is illustrated in figure 6.4. Here, the circles denote

the points of the value x_i in $x(t)$. The sum of the $D(x_i)$ for all x_i is one, as

$$\int_{-\infty}^{\infty} D(x_i)dx_i = 1$$

.

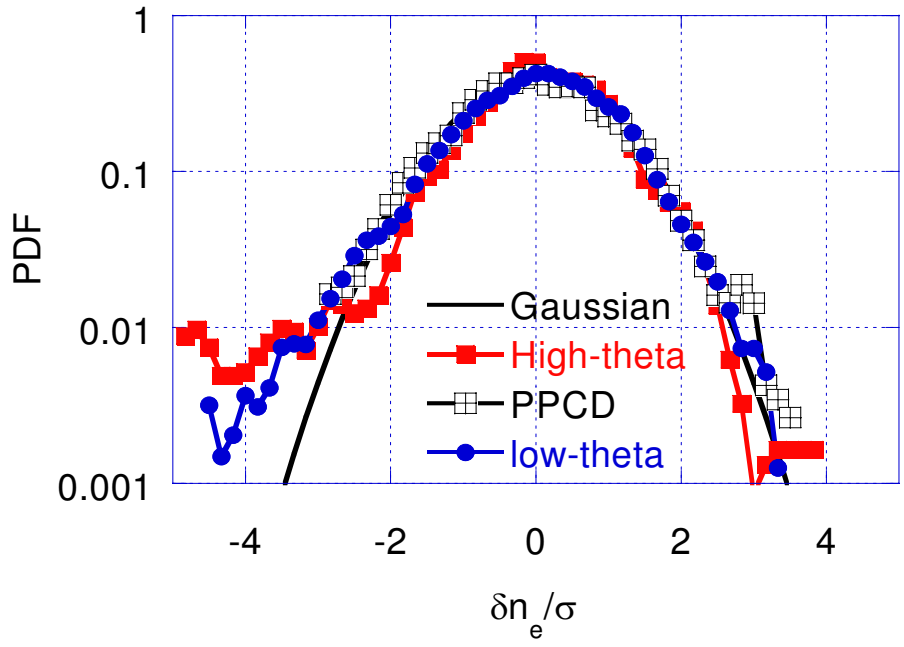

Figure 6.5: PDF of the standard and the PPCD plasmas

Figure 6.5 shows the PDF of the standard and PPCD plasmas. Here, the x-axis represents the fluctuation amplitude which is normalized by its standard deviation (σ). The black solid line denotes the Gaussian distribution. A non-Gaussian PDF represents the presence of coherent structures or intermittency of ambient turbulence. The PDF of PPCD plasma is similar to the Gaussian distribution, and the fluctuating quantities are limited at the low ($\delta n_e/\sigma$) values (no Gaussian tail), which suggests the fluctuation is suppressed. The standard plasmas have the non-Gaussian distribution. As shown in figure 6.1, the standard plasma has many negative intermittent bursts, which correspond to the negative non-Gaussian tail. The non-Gaussian tail is increased as the pinch parameter Θ ($\Theta = B_p(a)/ < B_t >$) is increased. This suggests more and more large peaked structures are generated as the Θ is increased in standard plasma.

To quantify the asymmetry and peak degrees of the fluctuation distribution with respect to its mean value, the third and fourth moments of the probability distribution function, called as skewness S and kurtosis K, are used. They are defined as [81]

$$S =< \widetilde{x}^3 > / < \widetilde{x}^2 >^{3/2} \tag{6.2}$$

$$K =< \widetilde{x}^4 > / < \widetilde{x}^2 >^2 -3 \tag{6.3}$$

respectively, where $\widetilde{x} = (x - \overline{x})/\sigma$ is the normalized fluctuation signal. The skewness is a measure of the asymmetry of the PDF. The kurtosis is a measure of the non-Gaussianity of the PDF. For a Gaussian random distribution, $S = K = 0$, whereas for others the deviation from zero indicates a non-Gaussian distribution. If one has a positive skewness, the relatively more positive perturbations exist than the negative one. On the contrary, a negative skewness corresponds to relatively more negative perturbations. As the absolute value of the skewness is increased, the asymmetry deviation from a Gaussian distribution is increased. If one has a higher kurtosis, there are larger perturbations (more negative and positive) for the present distribution than for a normal Gaussian one. The larger the kurtosis is, the further the present distribution deviates from a Gaussian one. A negative kurtosis represents the fluctuations are suppressed.

The dependence of skewness and kurtosis on the frequency can be obtained by using a wide bandpass filter (The filtered signal becomes a sinusoidal-like signal if we use a narrow band pass filter) [82]. The filter extracts the fluctuations in the bandpass domain (f_1, f_2). The skewness and kurtosis are calculated from the isolated fluctuations, and they are supposed to be located at the frequency $(f_1 + f_2)/2$ with a bandwidth of $f_2 - f_1$. Figure 6.6 shows the frequency dependence of the skewness and kurtosis in PPCD and standard ($F = -0.5, \Theta = 1.68$) plasmas. Here we use a bandwidth of $f_2 - f_1 = 50$ kHz. The dashed lines represent $S = K = 0$, respectively. The values of $|S|$ and K in PPCD plasma are very small (around zero). This corresponds to the symmetric fluctuation in the MIR signal. In standard plasma, the skewness is negative in the low frequency region ($f < 50$ kHz). This corresponds to the negative bursts in MIR signal. In the high frequency region, the skewness of standard plasma becomes positive, which suggests the high frequency fluctuation is different from the low frequency intermittent bursts in standard plasma. The kurtosis is increased with the frequency, and the kurtosis of standard plasma is much higher than that in PPCD plasma. It suggests that there are more peaked structures in standard plasma especially in the high frequency range.

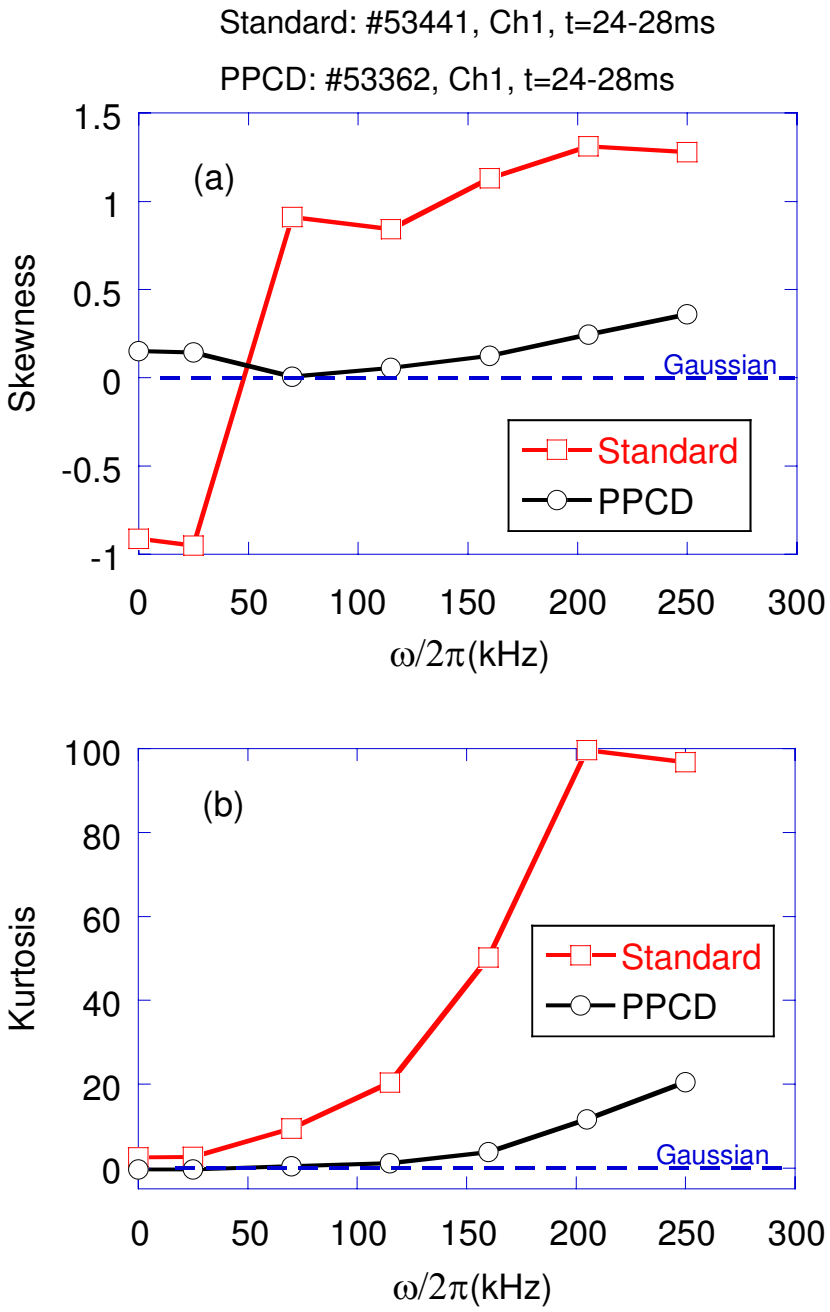

Figure 6.6: The frequency dependence of (a) skewness and (b) kurtosis in the PPCD and the standard plasmas

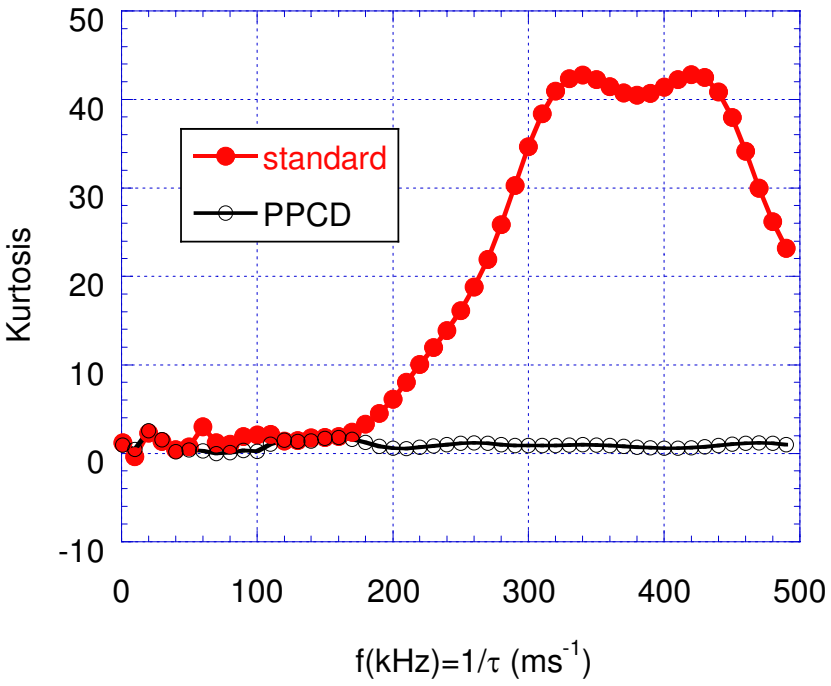

Figure 6.7: The kurtosis of the wavelet spectrum as a function of time scale in the PPCD and the standard plasmas.

In order to further understand the turbulent structures, the wavelet spectrum is used in the kurtosis analysis, because wavelet transform is sensitive to the short lived fluctuations [80]. Figure 6.7 shows the kurtosis of the wavelet spectrum as a function of time scale (inverse of frequency). In standard plasma, the kurtosis at the small time scale is rapidly increased. This corresponds to many short lived structures in the wavelet power spectrum. The kurtosis of PPCD plasma is much smaller than that of standard plasma especially in the small time scale range. Therefore, the turbulent structures have been suppressed in PPCD plasma.

6.4 Toroidal cross correlation

The characteristics of the fluctuations are analyzed by the two-point cross correlation method. In this section, we select the MIR signals, which are arranged in the toroidal direction, to study the characteristics of the toroidal cross correlation, such as the coherence and coherent length of the turbulence.

Figure 6.8 shows the cross-correlation spectra ((a) cross power spectrum, (b) coherence and (c) cross phase spectrum) of the standard and PPCD plasmas by using complex IQ signals ($X(t) = I + iQ$). The distance between two signals is 7.4 cm in the toroidal direction. Here, we select the data length of 10 ms at the flattop of the discharge. The data has been separated into 200 sections, and each section has 64 data points. Note that there is overlapping between the neighboring sections. The cross correlation spectra are obtained by ensemble averaging the cross Fourier spectra of these 200 data sections. Therefore, the frequency resolution is 15.6 kHz (1MHz sampling).

In the cross-power spectra, PPCD plasma has the high fluctuation power in the low frequency range, while the power spectrum is decreased in the high frequency range. The standard plasma has higher fluctuation power in the high frequency range, and it is slowly decaying compared with PPCD plasma. The decay index ($f^{-\alpha}$) of the power spectrum represents a qualitative indication of an energy exchange process between fluctuations at different scales [83]. The higher α denotes the stronger energy dissipation in the plasma. The power decay index of the PPCD plasma is about $f^{-2.5}$ in the frequency range of 200-500 kHz. In the standard plasma, the power decay index is about $f^{-1.4}$. The coherence decreases as the frequency increases, and it is higher than the noise level ($1/\sqrt{N}$) in the whole frequency range. In PPCD plasma, the coherence is higher than that in standard

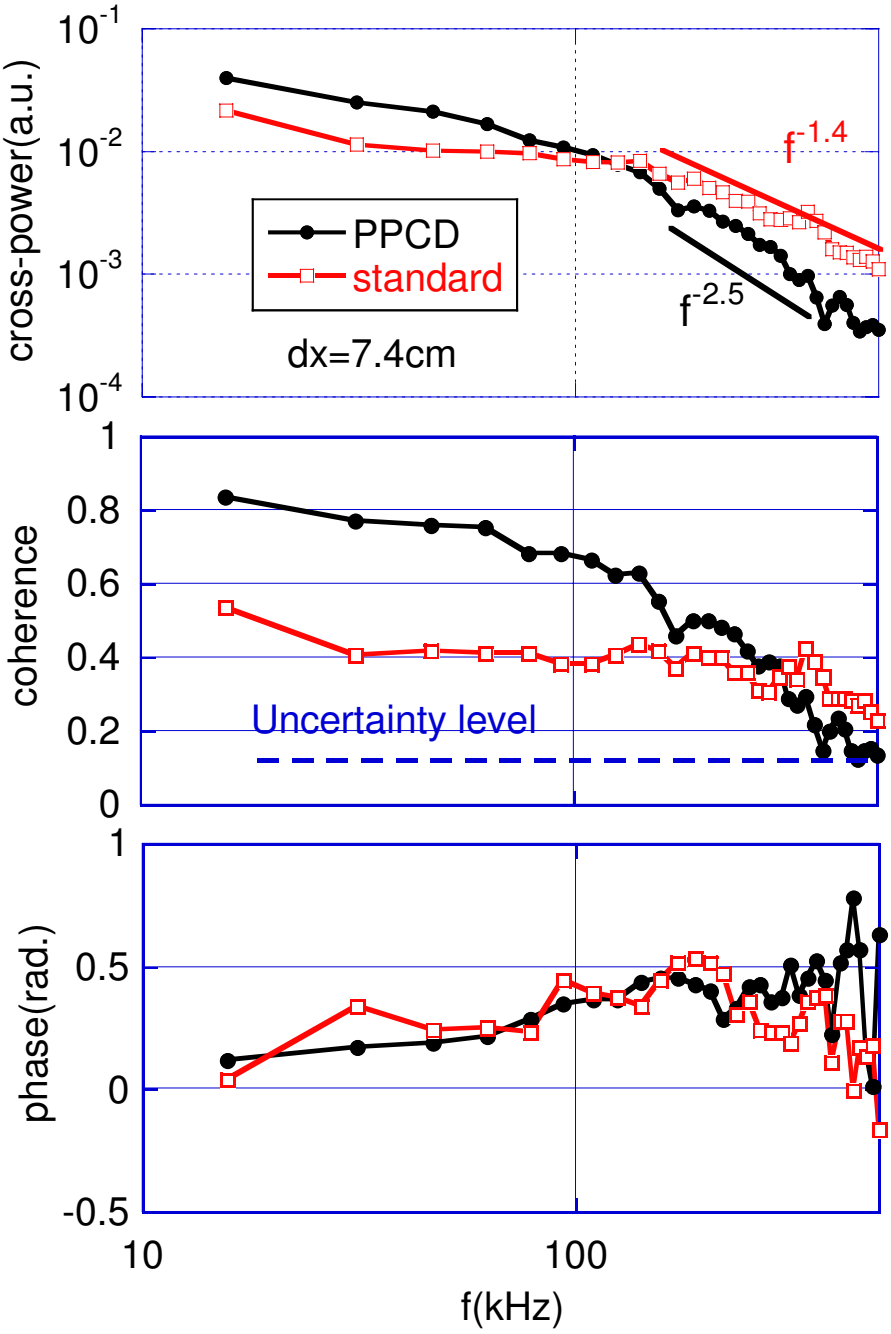

Figure 6.8: Cross-correlation analysis of the standard and the PPCD plasmas. (a) cross-spectrum, (b) coherence and (c) cross-phase

plasma, which suggests long distance fluctuation structures in PPCD plasma. Both the standard and PPCD plasmas have a positive cross-phase shift (electron drift direction). The phase shift linearly increases as the frequency increases, which gives a phase velocity (ω/k) about 100 kms^{-1} in the electron drift direction.

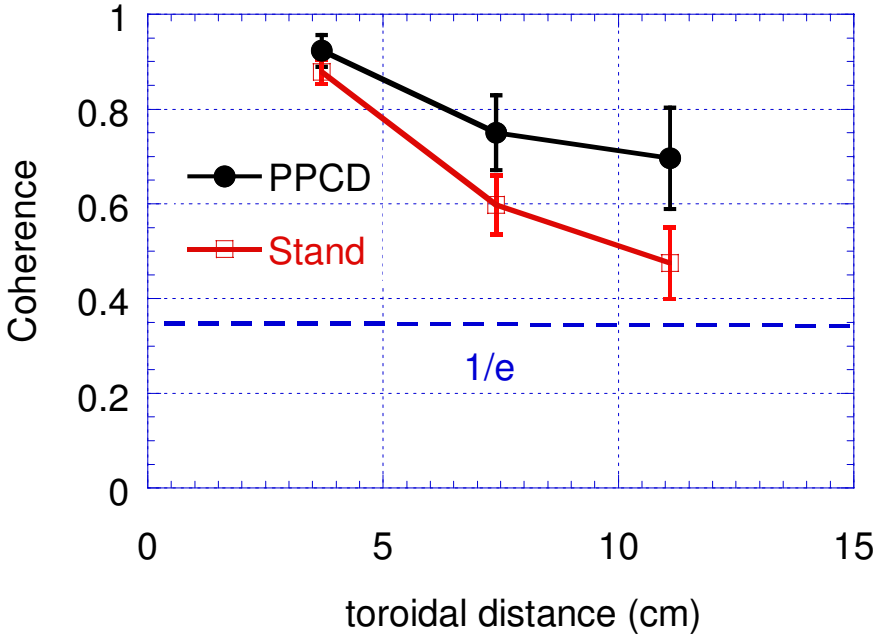

Figure 6.9: The toroidal coherence length

The coherence length identifies the size of the fluctuation. Figure 6.9 shows the toroidal coherence length of the standard (red square) and PPCD (black dot) plasmas (the magnetic field is mainly poloidal at the edge region). The coherence is obtained by averaging the toroidal coherence at $f = 10 \sim 100$ kHz. The coherence is decreased as the distance is increased. The toroidal correlation length is defined as the coherence is decreased to 1/e. Both the coherence of PPCD and standard plasmas are higher than this value in the measured range. So the coherence length is longer than the detector size. PPCD has higher coherence. So PPCD plasma has a longer coherence length and standard plasma has a shorter coherence length. Therefore, the fluctuations in PPCD plasma have the characteristic of large-scale structures. In standard plasma, the fluctuations have the characteristic of small-scale structures. If we draw a trendline in figure 6.9, the toroidal correlation length of PPCD and standard plasmas at the cutoff

surface ($r_{cut} \approx 0.8$) can be estimated. The estimated correlation length may be larger than 40 cm in PPCD plasma, while it is about $15 \sim 20$ cm in standard plasma. Note that the estimated toroidal correlation length at ($r_{cut} \approx 0.8 - 0.85$) is similar to results at $r/a = 1.0$ measured by GPI in TPE-RX [41].

6.5 Mode analysis

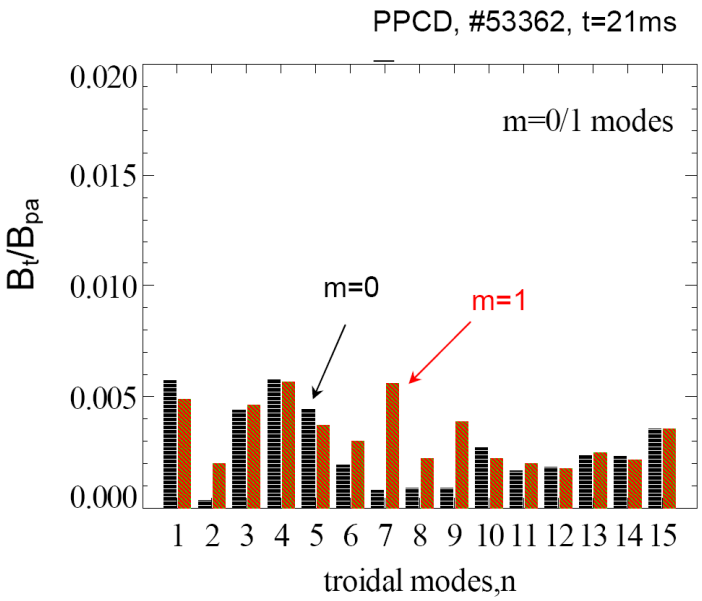

Figure 6.10: $m = 0$ and $m = 1$ modes in the PPCD plasma

Figure 6.10 shows the mode spectra ($\widetilde{B_t}/B_p(a)$) of the magnetic fluctuations ($m = 0$ and $m = 1$ modes) as a function of the toroidal modes n in PPCD plasma (#53362, $t = 20 - 22$ ms). The magnetic fluctuations are obtained by an extensive magnetic measurement system (MMS) [53]. The power of the $m = 1$ modes is higher than the $m = 0$ modes. It may indicate the suppression of the dynamo ($m = 0$ modes). The fluctuation in PPCD plasma is dominated by the localized MHD modes ($m = 1$ modes). The low n modes have the high fluctuation energy. The high n or (k) modes have very small power. This suggests that the high k modes (or small-scale fluctuations) have been suppressed. As shown in Fig. 6.1(f), the frequency in the wavelet spectrum has the

short-lived features, though the summed spectrum is dominated by a single frequency of ~ 20 kHz. Therefore, the low n modes ($n = 1 \sim 7$), which have the dominant fluctuation power, may have different fluctuation frequencies.

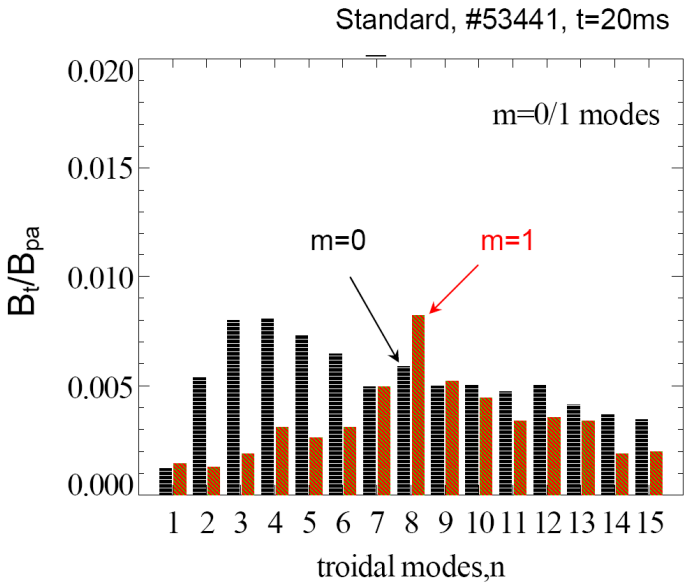

Figure 6.11: $m = 0$ and $m = 1$ modes in the standard plasma

Figure 6.11 shows the mode spectra of the magnetic fluctuations ($m = 0$ and $m = 1$ modes) as a function of the toroidal modes n in standard plasma (#53441, $t = 19 - 21$ ms). The power spectra of standard plasma is stronger than that of PPCD plasma. This is as a result of strong magnetic fluctuation in standard plasma. The power of the $m = 0$ modes is higher than the $m = 1$ modes especially for the low n modes. It suggests the global features of the fluctuations (global dynamo effects, $m = 0$ modes) in standard plasma. The fluctuation powers of the these modes are much higher than that in PPCD plasma. The wide distribution of $m = 0$ and $m = 1$ modes suggests that the standard plasma is rich of fluctuation structures (multi-helicity (MH) state).

6.6 2D k-spectrum

Figure 6.12 shows the 2D wavenumber (k) spectra of the standard and PPCD plasmas by using complex IQ signals ($X = I + iQ$). Here, the k_φ and k_θ are the toroidal and

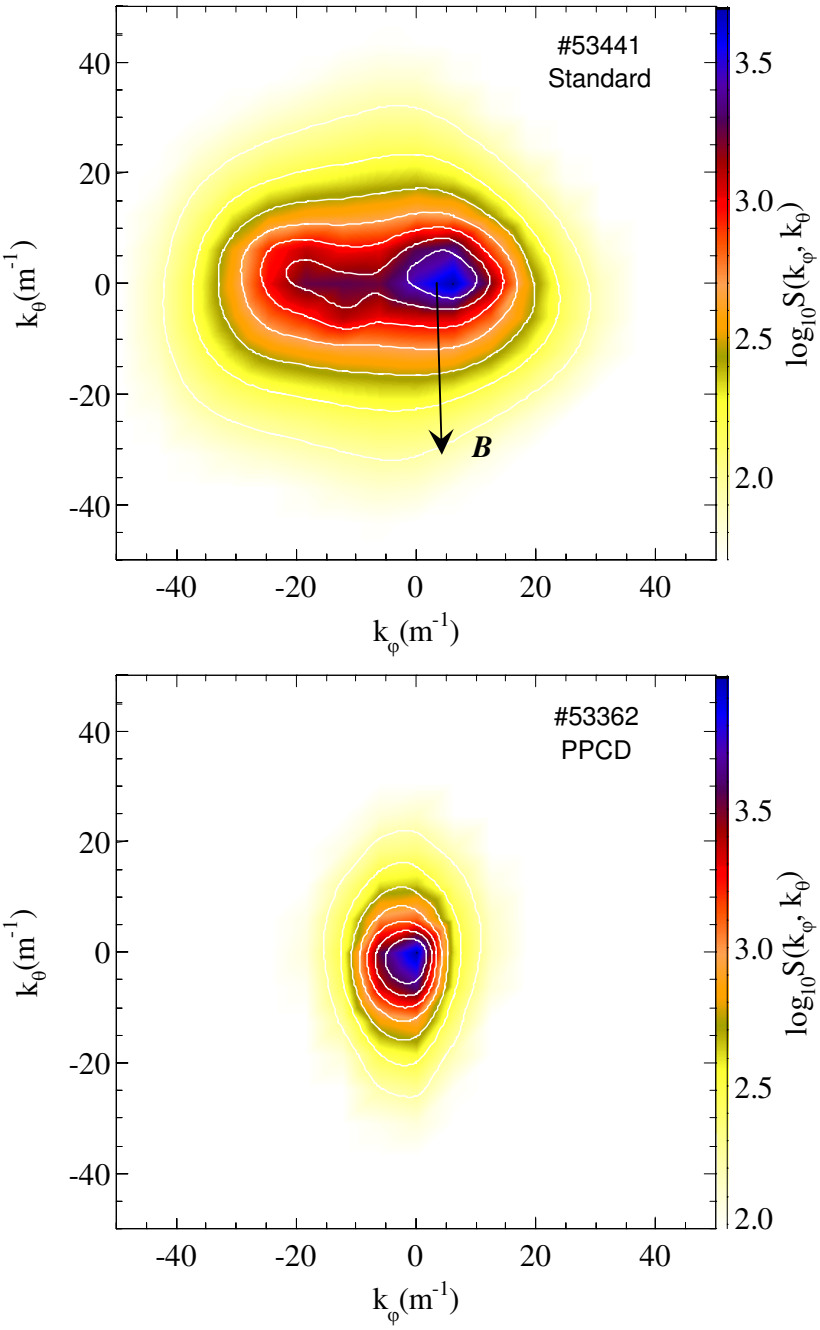

Figure 6.12: The 2D k spectra ($\log_{10} S(k_\varphi, k_\theta)$) of the standard (top) and the PPCD (bottom) plasmas estimated by MEM

poloidal wavenumbers, respectively. The k spectra are analyzed by the 2D maximum entropy method (MEM) [69; 73]. The details of the MEM have been discussed in chapter 5. In PPCD plasma, the fluctuation power is localized in the low k_θ and k_φ ranges, and the spectrum is dominated by a pinpoint ($m = 0 \pm 4$, $n = 0 \pm 15$). The k spectrum of the standard plasma distributes in a wide k range, especially in the toroidal direction ($m = 0 \pm 6$, $n = -60 \sim 40$). The magnetic field is mainly poloidal near $r_{cut} \approx 0.8$. It is indicated by an arrow in figure 6.12. The k spectrum spreads in the electron drift direction which is perpendicular to the magnetic field line. The expansion into the high k range suggests presence of many mode structures in standard plasma. This result is consistent with the multi-helicity modes state in the standard plasma (see figure 6.11).

Figure 6.13 shows the toroidal modenumber-frequency spectra $\log_{10} S(n, f)$ of standard (top) and PPCD (bottom) plasmas. The toroidal modenumber spectrum is obtained by integrating the 2D k spectra (in poloidal direction) estimated by MEM. In standard plasma, the spectrum is broad ($n = -60 \sim 40$) in the whole frequency range. In PPCD plasma, The fluctuation is limited at the low n mode range ($n = 0 \pm 20$) and the fluctuation power becomes weak at high frequency range.

Figure 6.14 shows the k_φ (or n) spectra of the standard and PPCD plasmas by integrating the toroidal modenumber-frequency spectrum from 15 kHz to 110 kHz. PPCD has a sharp peak at the low n mode ($n \sim 0$). In standard plasma, the spectrum has a broad peak with high fluctuation power. The width of n spectrum is $\Delta n \sim 120$ (from $n = 40$ to -80). The n spectrum of standard plasma tends to shift in the electron drift direction. These results suggest that the turbulence measured by MIR has the electrostatic-like features [46; 48]. The wide k spectrum suggests standard plasma has high turbulence. In PPCD plasma, the narrow k spectrum indicates PPCD has low turbulence. The large fluctuation in PPCD plasma (shown in figure 6.1) may be the low frequency MHD mode.

6.7 Correlation structures

Both the magnetic and electrostatic fluctuations can induce the density fluctuations. As discussed in chapter 1, the electrostatic fluctuation is dominant in the edge region, while in the core region, the magnetic fluctuation is dominant. In this work, MIR measures the

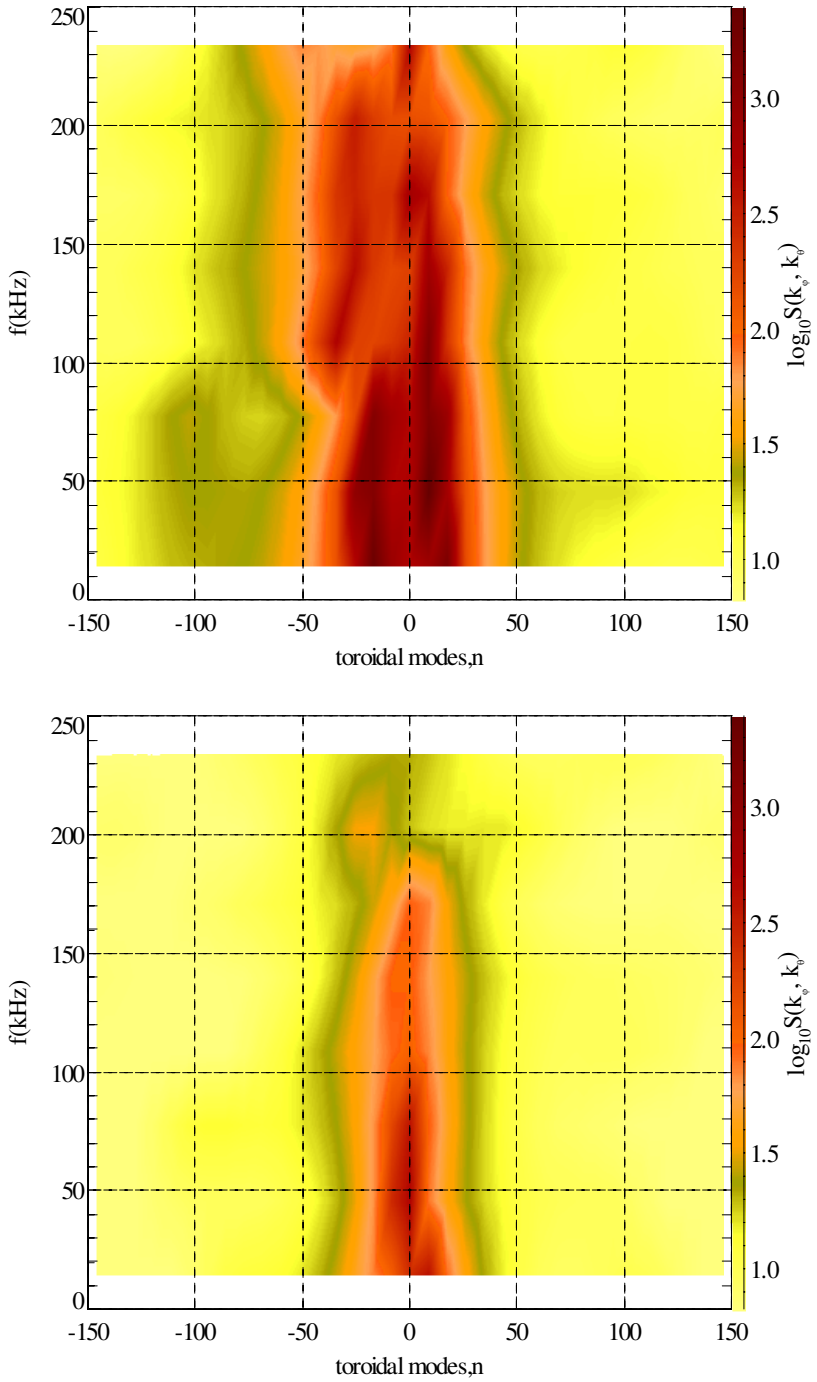

Figure 6.13: The modenumber-frequency spectra of the standard (top) and the PPCD (bottom) plasmas

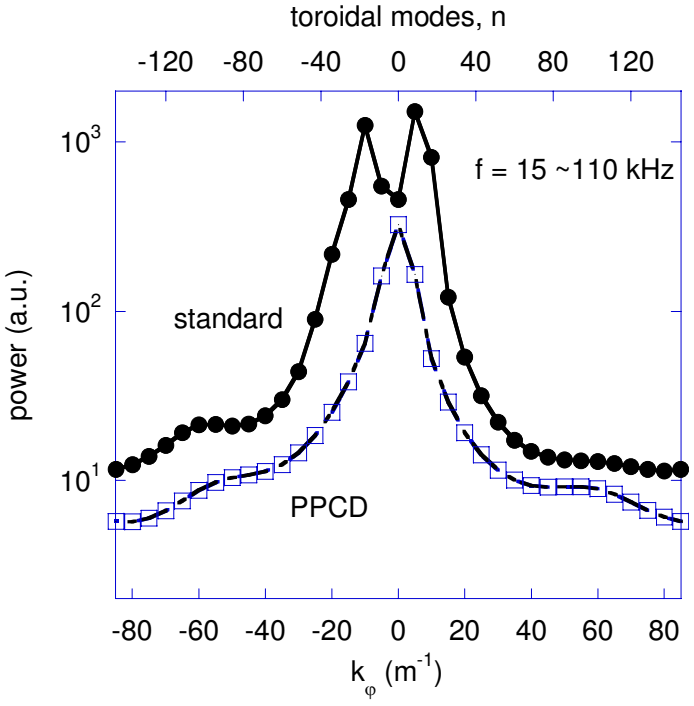

Figure 6.14: The k_φ spectra of the standard and the PPCD plasmas

local density fluctuation near the field reversal region. This area may have many high n tearing modes ($m = 1$), $m = 0$ tearing modes and strong electrostatic fluctuations.

In order to analyze the dominant fluctuation in MIR, one good way is taking the correlations of MIR signal with magnetic fluctuation and with electrostatic fluctuation. Here, we use the magnetic and electrostatic fluctuations measured by a complex edge probe system (CEP). MIR and CEP are arranged in the same poloidal plane (see chapter 2). The CEP is arranged at $r/a = 1.05$ in the vertical (top) position. MIR is arranged at the equatorial position and the cutoff surface is about $r/a \simeq 0.8$. The radial distance between MIR and CEP is about 10 cm.

Since the MIR, magnetic and electrostatic probes measure at different positions, the measured fluctuations may have some time delay. Here, the correlation function is used. It is a function of one signal (auto) or between signals (cross) which allows extraction of lag time and correlation time. The method integrates one signal (the reference signal), and another signal shifted in time. The shift parameter is defined as the time delay τ, and is the variable which the function $C_{1,2}$ is plotted against. The equation is normalized, bounding $C_{1,2}(\tau) \in [-1, 1]$, as

$$C_{1,2} = \frac{\int x_1(t)x_2(t-\tau)dt}{\sqrt{\int x_1^2(t)dt \int x_2^2(t)dt}} \tag{6.4}$$

where, $x_1(t)$ and $x_2(t)$ denote two signals, respectively. The auto correlation function is defined as $C_{1,1}$.

Figure 6.15 shows the cross-correlation between (a) MIR and $\widetilde{B_r}$, (b) MIR and V_f in PPCD and standard plasmas. In order to select the low frequency fluctuation, the signals are low-pass filtered at 20 kHz. As a result, the possible high frequency turbulence do not affect the analysis. The correlation is not high due to the large distance between MIR and probes. MIR signals have similar correlations with magnetic and potential fluctuations. The periodical correlations between MIR and magnetic fluctuations give the frequencies of ~ 17 kHz in PPCD plasma and ~ 12 kHz in standard plasma, which agree with the results shown in Fig. 6.1 (f). This result suggests that the low frequency fluctuation in MIR signal is caused by the MHD modes.

Figure 6.16 shows the (a) autocorrelations of MIR (black solid line), the radial magnetic fluctuation $\widetilde{B_r}$ (red dotted line) and floating potential (V_f) (blue dashed line), (b) toroidal cross-correlation of MIR (ch1-ch2) and V_f (ch1-ch2), (c) cross-correlation between V_f and $\widetilde{B_r}$, and (d) cross-correlation of the MIR ($r = 0.8$, and $r = 0.85$) with V_f,

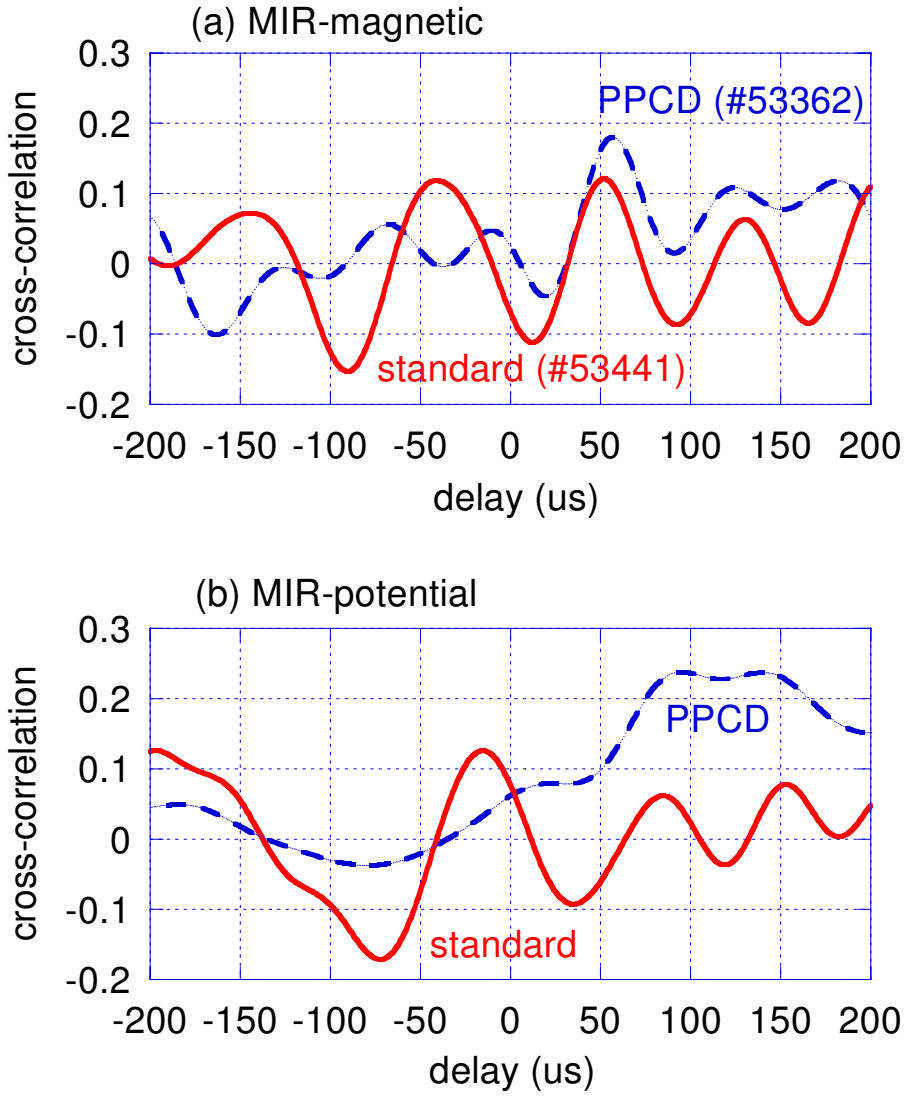

Figure 6.15: Cross-correlation functions of (a) MIR and $\widetilde{B_r}$, (b) MIR and V_f. All the signals are low-pass filtered at $f < 20$ kHz.

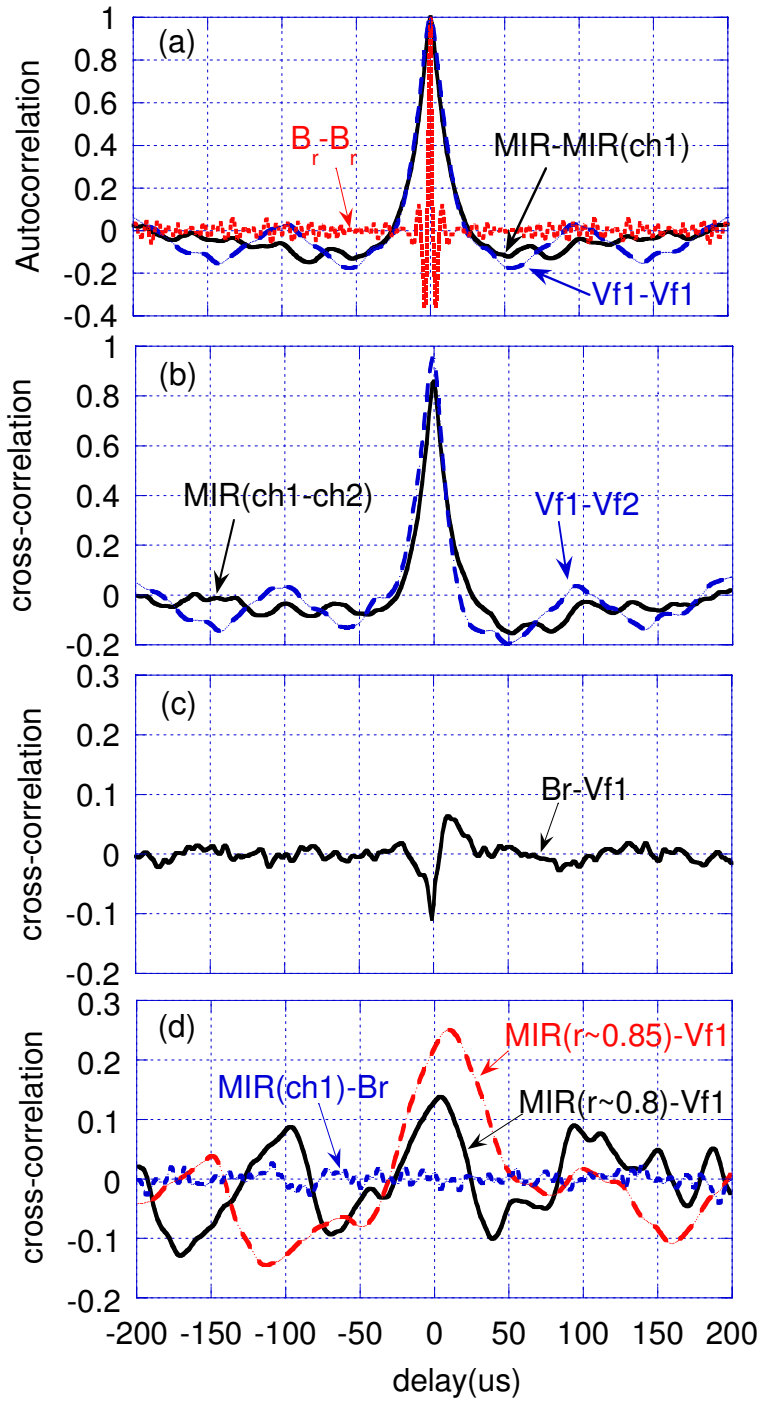

Figure 6.16: (a) Autocorrelations of MIR, V_f and $\widetilde{B_r}$, (b) toroidal cross-correlation of MIR and V_f, (c) cross-correlation between V_f and $\widetilde{B_r}$, (d) cross-correlation of MIR (ch1) with V_f and $\widetilde{B_r}$. All the signals are high-pass filtered at $f > 2$ kHz.

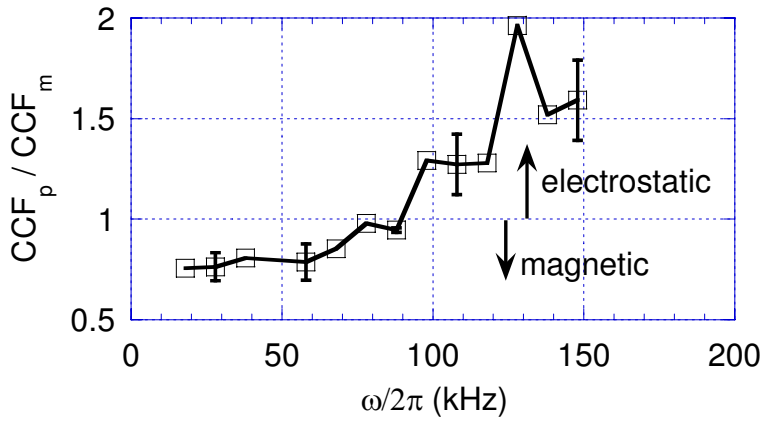

Figure 6.17: The relative correlation ratio of MIR signal with potential and magnetic fluctuations

and MIR ($r = 0.8$) with $\widetilde{B_r}$ in the standard plasma.In order to select the high frequency turbulence, the signals are high-pass filtered at 2 kHz. As a result, the possible low frequency fluctuations do not affect the analysis. The distances between the two signals used in Fig. 6.16 (b) are 3.7 cm for MIR and 0.5 cm for floating potential, respectively. The autocorrelations of MIR and floating potential are similar when the time delay is smaller than 50 μs. It gives the autocorrelation time of $\sim$ 25 μs for the density and potential fluctuations. The autocorrelation time of magnetic fluctuation is only about 10 μs. There is no correlation between magnetic and potential fluctuations (Fig. 6.16 (c)).

There are some correlations between the MIR signal and the potential, though it is very low (about $0.15 \sim 0.25$) (Fig. 6.16 (d)). The reason may be the large radial distance between MIR and electrostatic probe (about $8 \sim 10$ cm), and the short radial correlation length of the electrostatic turbulence [4]. Nevertheless, the correlation between MIR and potential is much higher than that between MIR and magnetic fluctuations in the high frequency range. The correlation between MIR and floating potential increases as the distance between MIR and electrostatic probe decreases, and the time delay between them is very small.

To understand the frequency dependence of the correlation of MIR signal with the potential and the magnetic fluctuation. A bandpass filter is used to extract the fluctuations in the bandpass domain. Figure 6.17 shows the relative cross-correlation ratio $\mathrm{CCF_p/CCF_m}$ as a function of frequency. Where, $\mathrm{CCF_p}$ denotes the cross-correlation

(standard deviation) between MIR signal and potential, $\mathrm{CCF}_{\mathtt{m}}$ denotes the cross-correlation (standard deviation) between MIR signal and magnetic signal. The signals are bandpass filtered with the bandwidth of 35kHz. The relative cross-correlation indicates that the low frequency mode has high correlation with the magnetic fluctuation, and the high frequency mode has high correlation with the electrostatic fluctuation. These results suggest that the low frequency modes are dominated by the magnetic fluctuation, and the high frequency modes are dominated by the electrostatic turbulence.

6.8 Nonlinear wave interaction

6.8.1 Toroidal spatial waves

Since we have a 2D detector array in MIR system, the spatial structures of the fluctuations can be obtained. Assume a toroidal (or poloidal) periodic condition on the fluctuation, the time evolution of the wave on the cutoff surface is obtained by the spatial Fourier transform of the MIR signals.

$$S(k,t) = \sum_{l=0}^{L-1} X(l,t) e^{i2\pi kl/L} \tag{6.5}$$

where, L is the total aligned toroidal (or poloidal) detector number. The wavenumber k is normalized by the Nyquest wavenumber $k_N = \pi/d$. $X(l,t)$ is the density fluctuation measured by MIR. The complex IQ signals $X(l,t) = I + iQ$ are used because they directly correspond to the density fluctuation and are more sensitive to the high frequency fluctuations [18; 57]. If there is a mode in the fluctuation, the spectrum of the IQ signal is asymmetric. The asymmetric power spectrum include the propagation direction of the mode. But for the amplitude signal, its spectrum is symmetric.

MIR has a (4×4) detector array. Here, we select four detectors arranged along the toroidal direction to do the spatial Fourier transform. The wavenumbers of $-0.5k_N, 0, 0.5k_N$ and k_N can be obtained. Where, the Nyquest wavenumber $k_N = 85$ m^{-1} represents the wavelength of 7.4 cm and the toroidal modenumber of $n = 146$. The half Nyquest wavenumber is $0.5k_N = 42$ m^{-1}, which represents the toroidal modenumber of $n = 73$. The minus indicates the opposite propagation direction. The wavenumbers obtained by equation 6.5 may include many spatial modes due to the poor spatial resolution.

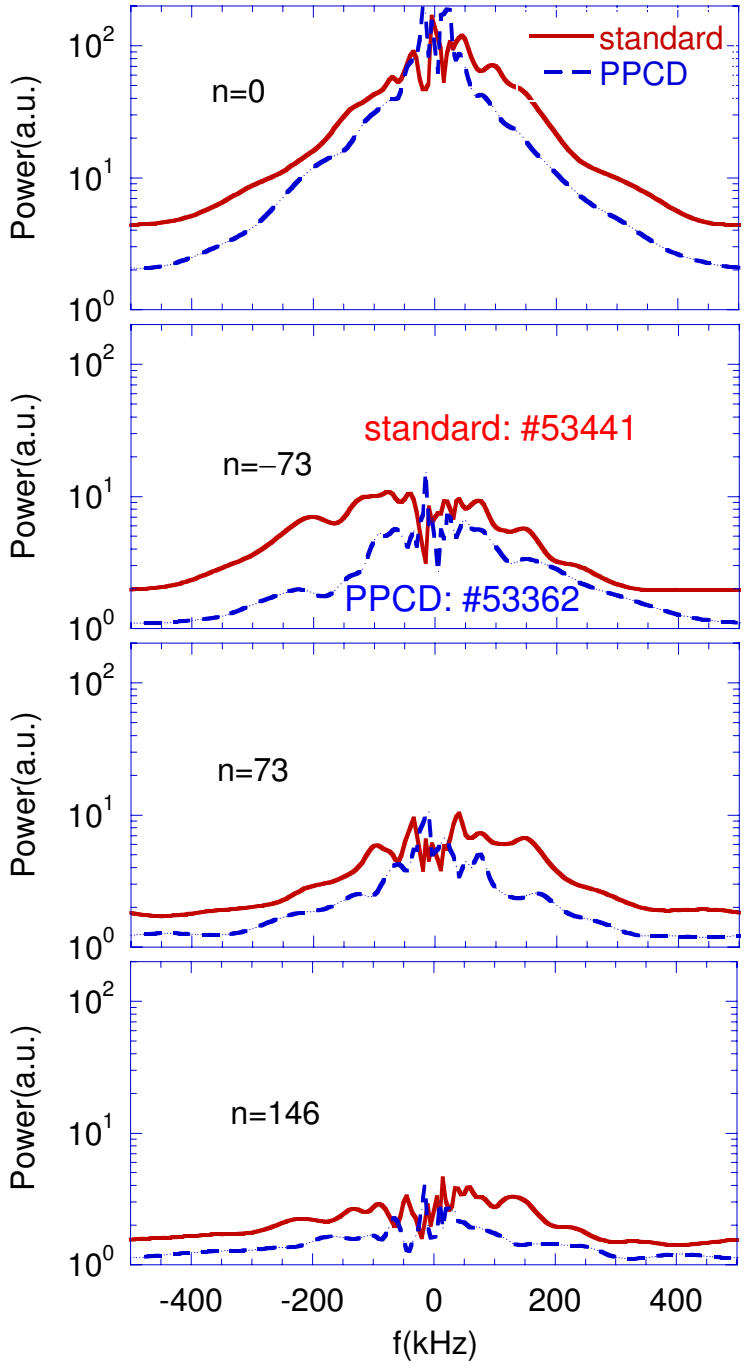

Figure 6.18: Power spectra of the waves in the standard and the PPCD plasmas.

Figure 6.18 shows the wavelet power spectra of the waves with the wavenumbers of $0, -0.5k_N, 0.5k_N, k_N$ (or modenumbers of $n = 0, -73, 73, 146$ with $\delta n = \pm 37$) in standard (shot #53441) and PPCD (shot #53362) plasmas. The power spectra are transformed from wavelet analysis method within 8 ms during the flattop of the plasma current. Some frequencies are observed in the spectra. The fluctuation energy of $k = 0$ mode is much stronger than the high k modes. The fluctuation energy is decreased as k is increased. For $k = k_N$ ($n = 146$), the fluctuation becomes the noise level.

The fluctuation energy of the standard plasma is higher than that in PPCD plasma, especially in the high modenumber and high frequency ranges. Some fluctuation frequencies are observed in the standard plasma, for example the frequencies of -200 kHz, -100 kHz, 50 kHz and 150 kHz. In PPCD plasma, the MHD mode ($k = 0$) with the frequency of $\sim$20 kHz is observed. This corresponds to the sinusoidal fluctuations shown in figure 6.1(e).

6.8.2 Nonlinear interaction

The nonlinear simulation of turbulence suggests that there is a strong mode to mode interaction when the wavenumbers satisfy the matched condition $k_1 + k_2 = k_3$. The interaction of the mismatched coupling ($k_1 + k_2 \neq k_3$) is very weak usually, and it is often considered as the noise level.

To quantify the strength of the nonlinear wave interaction, the squared wavelet bicoherence is used due to the short lived time scales ($s < 100$ μs) of the RFP turbulence [80]. It is defined as [84]

$$b^2(s_1, s_2) = \frac{| < W_{k_1}(s_1, \tau) W_{k_2}(s_2, \tau) W^*_{k_3}(s, \tau) > |^2}{< |W_{k_1}(s_1, \tau) W_{k_2}(s_2, \tau)|^2 >< |W_{k_3}(s, \tau)|^2 >} \tag{6.6}$$

where, $<>$ indicates the ensemble average over time τ. The time scales s satisfy the frequency sum rule within the frequency resolution, as

$$\frac{1}{s} = \frac{1}{s_1} + \frac{1}{s_2} \tag{6.7}$$

Since the time scales can be interpreted as inverse frequencies $\omega/2\pi = 1/s$, it is convenient to interpret the sum rule as $\omega = \omega_1 + \omega_2$. $W_k(s, \tau)$ is the Morlet wavelet transform of the waves obtained by equation 6.5, as:

$$W_k(s, \tau) = \frac{1}{\sqrt{s}} \int S(k, t) \Psi^*(s, \tau) dt \tag{6.8}$$

where, $\Psi(s,\tau) = \pi^{-1/4}\exp[-i2\pi\tau/s - (\tau/s)^2/2]$ is the Morlet function.

To compare the strength of the nonlinear interaction, it is convenient to introduce the summed bicoherence, which is defined as

$$b_s^2(\omega) = b_s^2(s) = \sum_{1/s=1/s_1+1/s_2} b^2(s_1, s_2) \tag{6.9}$$

where the sum is taken over all time scales s_1, s_2 satisfied the frequency sum rule, and the total bicoherence

$$b_{tot}^2 = \sum_{s_1,s_2} b^2(s_1, s_2) \tag{6.10}$$

where the sum is taken over all time scales s.

Since four detectors along the toroidal direction are used in the spatial Fourier transform, the wavenumbers of $k = -0.5k_N$, 0, $0.5k_N$ and k_N (or $k = -42$, 0, 42, and 85 m^{-1}) are obtained, which represents the toroidal modenumbers of $n = -73$, 0, 73 and 146. It is convenient to define the normalized wavenumbers as $k_a = -1$, 0, 1 and 2, which correspond to the wavenumbers of $k = -42$, 0, 42 and 85 m^{-1}, respectively. Here, the nonlinear wave interaction among the three waves of k_1, k_2 and k_3 is defined as $k = (k_1, k_2, k_3)$.

Some wavenumbers satisfy the matched condition of the nonlinear wave interaction, for example $k_a = (-1, 1, 0)$ and $k_a = (1, 1, 2)$. The matched couplings of $k_a = (-1, 1, 0)$ and $k_a = (1, 1, 2)$ represent the nonlinear interactions between different turbulent scales. It should be noted that the spatial modes measured by MIR include a wide mode range. $k_a = 0$ represents the low n modes ($n = 0 \pm 37$) which may be dominated by the MHD modes. $k_a = 1$ represents the $n = 73 \pm 37$ mode which may correspond to high k turbulence. The coupling of $k_a = (-1, 1, 0)$ may represent the correlation between the MHD and turbulence.

Figure 6.19 shows a typical squared wavelet bicoherence spectra among the waves of $k_a = (-1, 1, 0)$ in the standard and the PPCD plasmas. The wavelet transform is performed within 8 ms during the flattop of the plasma current. The spectrum has some high dispersed bicoherence. This is caused by the interaction between the frequency components shown in figure 6.18, for example, the high bicoherence at $\omega_1/2\pi \approx -100$ kHz and $\omega_2/2\pi \approx -100$ kHz. The bicoherence doesn't have a linear relation. It suggests that the nonlinear coupling in the standard plasma is more complicated than the linear three wave interaction. It may have a higher order interaction. The bicoherence of the

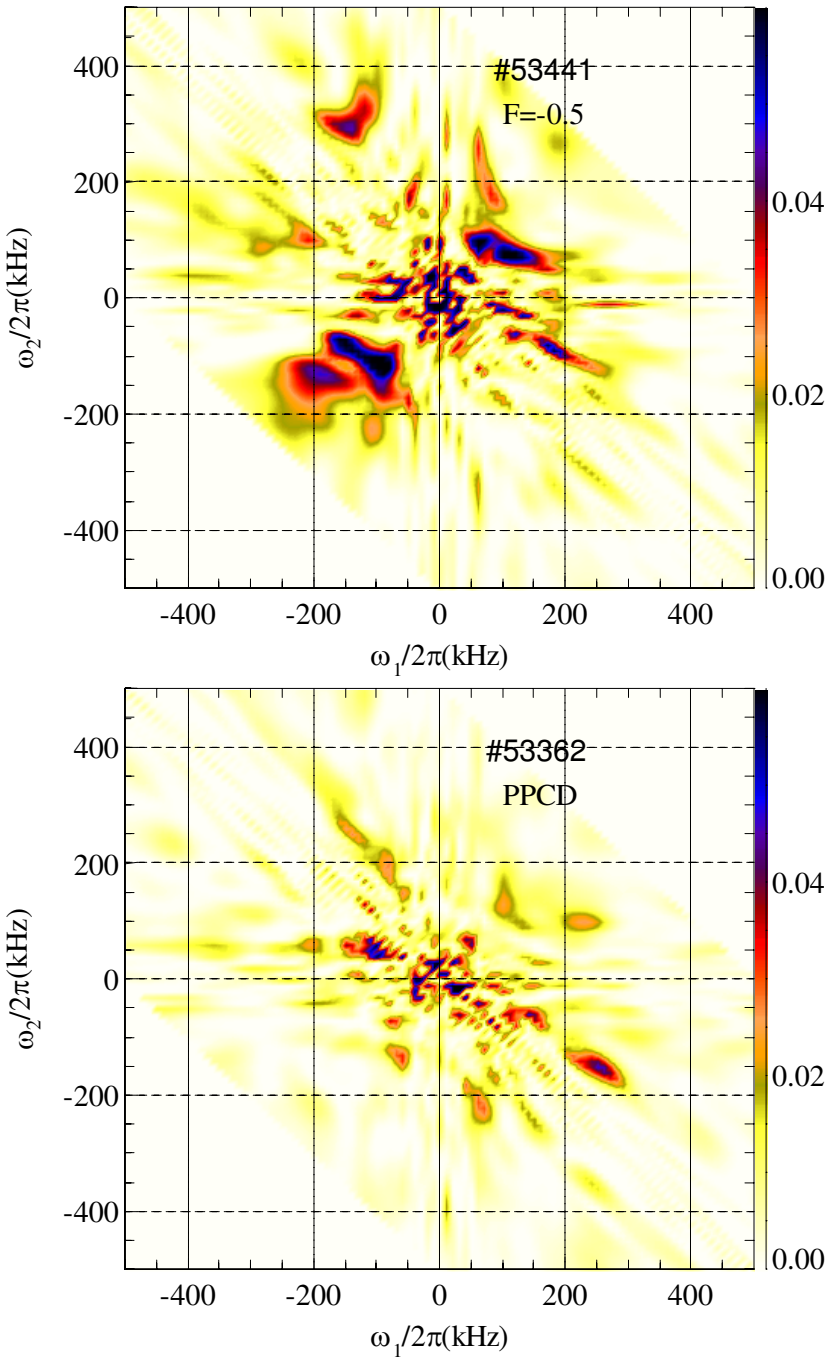

Figure 6.19: The squared wavelet bicoherence of the coupling among the modes of $k_a = (-1, 1, 0)$ in the standard ($F = -0.5$, top) and the PPCD (bottom) plasmas

standard plasma is distributed in a wide frequency range, and it is much stronger than that in the PPCD plasma.

Since the edge reversed toroidal magnetic field is mainly sustained by the fluctuations in the dynamo process, the reversal parameter F can be used to identify the strength of the nonlinear interaction in the standard RFP plasma. The deeper F corresponds to the stronger nonlinear interaction and higher turbulence. It should be noted that the pinch parameter Θ is usually high in the deeper F plasma. The explanation of high turbulence at deep F is only valid for the standard plasma. In the PPCD plasma the deep F is caused by the external driven field which may suppress the turbulence.

Figure 6.20 shows the summed wavelet bicoherence among the waves of (-1, 1, 0), (1, 1, 2) and (2, 2, 2) with (a) $F = -0.15$, (b) $F = -0.3$, (c) $F = -0.5$ in standard plasmas and (d) in PPCD plasma. The summed bicoherence is averaged over several shots with the same plasma condition. The dot-dash line represents the Milligen noise level, which is an empirical formula defined as [84]

$$b_n^2(\omega_1, \omega_2) = \frac{\omega_{samp}/2}{min(|\omega_1|, |\omega_2|, |\omega_1 + \omega_2|)} \frac{1}{N} \tag{6.11}$$

The matched coupling is distinctly stronger than the mismatched coupling of (2, 2, 2) and than the Milligen noise level. The bicoherence among the coupling of $(-1, 1, 0)$ is larger than that of (1, 1, 2) which suggests that there is strong interaction between the mid-scale and the large-scale turbulent structures in the standard plasma. PPCD plasma has low bicoherence, the reason may be the turbulence is suppressed by external driven field. The bicoherence becomes high as F decreases from -0.15 to -0.5. It is interesting to find that the increase in the bicoherence at deep F is mainly contributed by the high frequency fluctuations.

Figure 6.21 shows the total bicoherence as a function of F in the standard and the PPCD plasmas. For the PPCD plasma, we only show the coupling of $(-1, 1, 0)$ which indicated by blue filled square (Note: F in the PPCD plasma is different from the standard plasma). In the standard plasma, the bicoherence of $(-1, 1, 0)$ increases when F increases in the negative direction. It is about two times higher than the interaction of (1, 1, 2). In the PPCD plasma, the total bicoherence of $(-1, 1, 0)$ is about half of the standard plasma (deep F) which suggests that the nonlinear wave interaction is weak in the PPCD plasma.

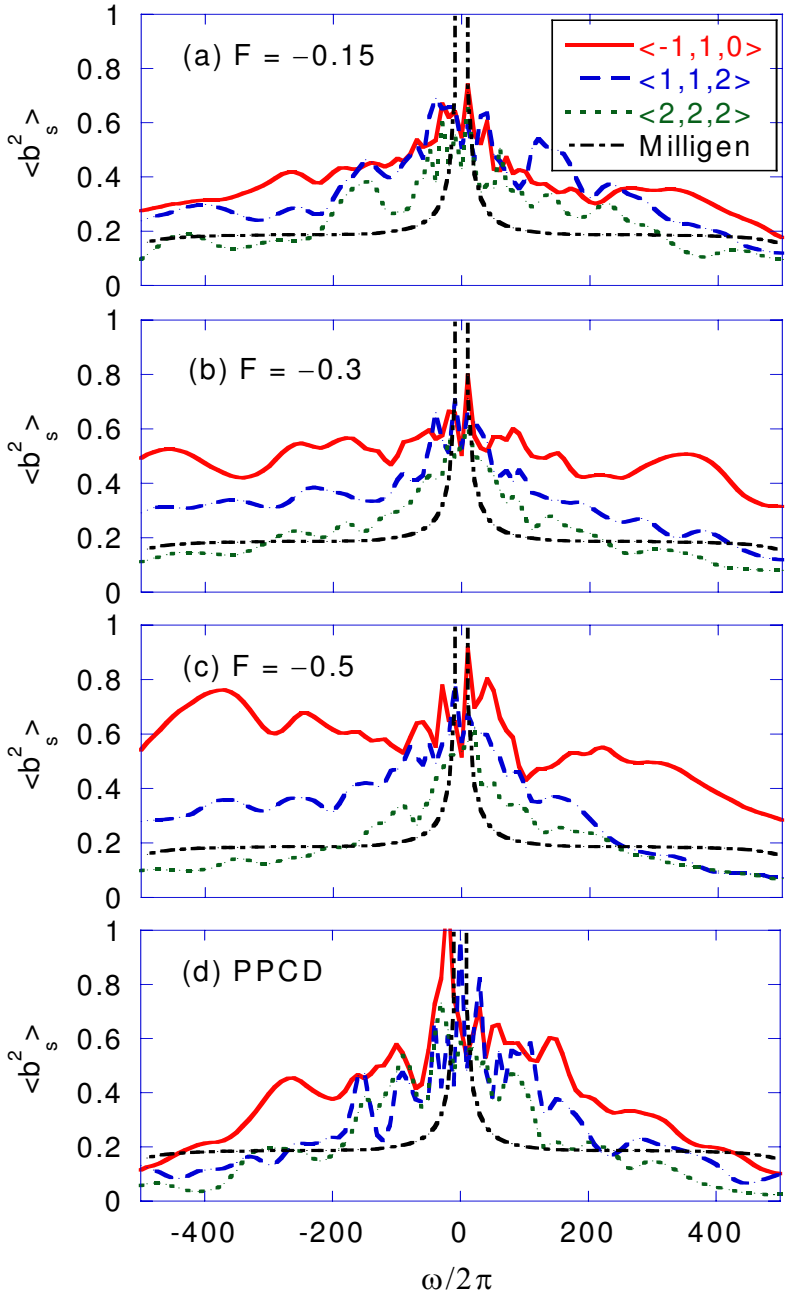

Figure 6.20: The summed wavelet bicoherence of the coupling between the waves of $(-1, 1, 0)$, (1, 1, 2) and (2, 2, 2) with (a) $F = -0.15$, (b) $F = -0.3$ and (c) $F = -0.5$ in the standard plasmas, and (d) in the PPCD plasma. The bicoherence is conditional averaged.

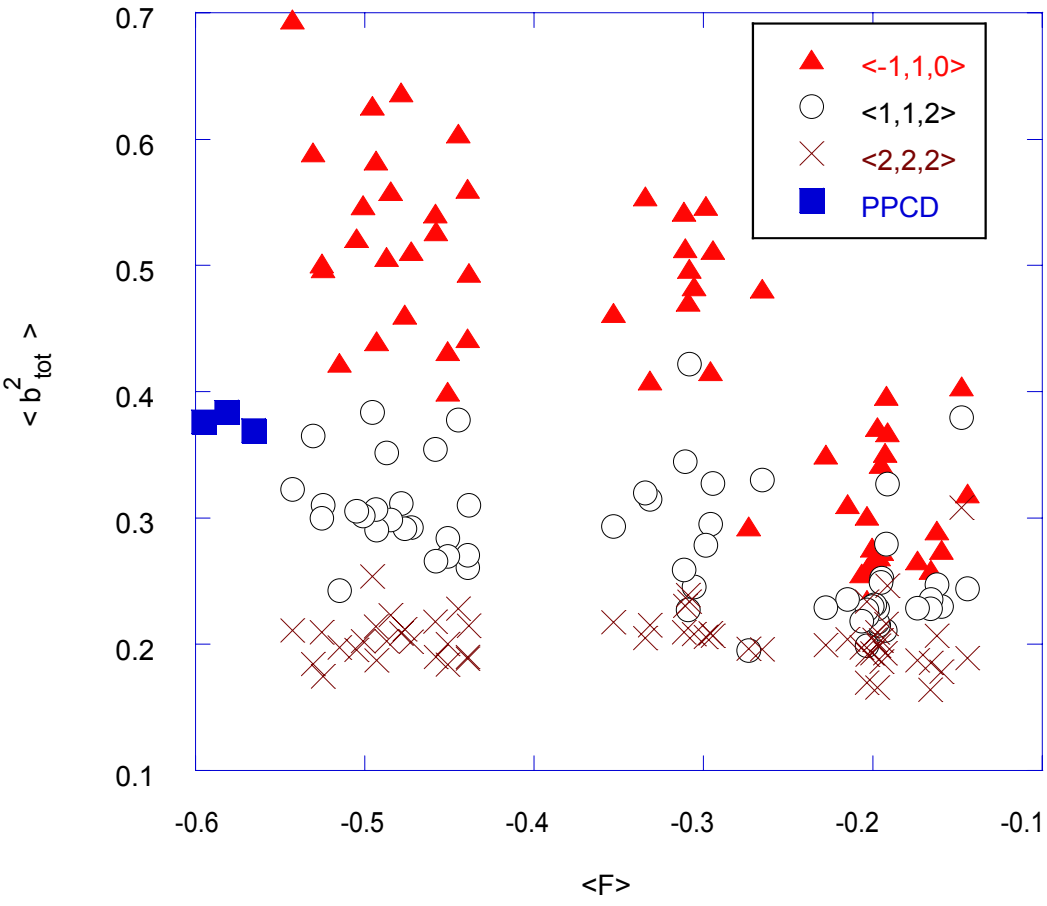

Figure 6.21: The total bicoherence as a function of F in the standard and the PPCD plasmas.

6.9 Relation with intermittent structures

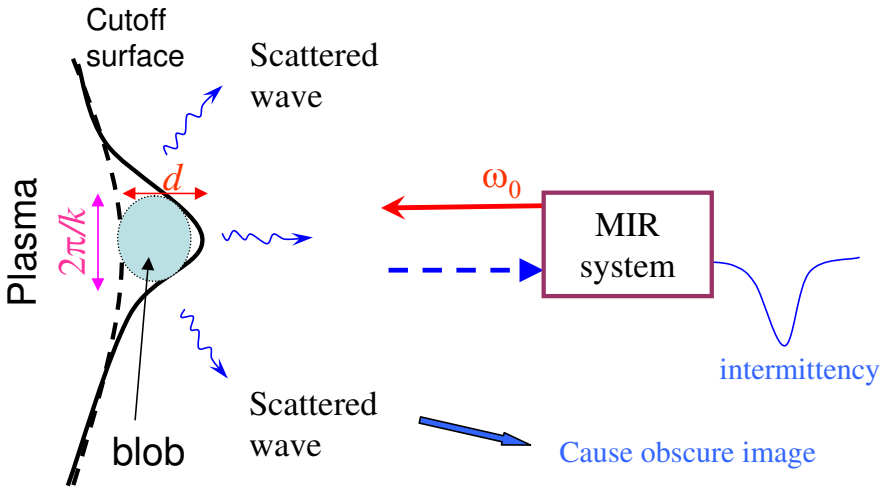

Figure 6.22: Schematic of intermittency caused by the scattering of one blob-like structure.

The presence of the large-scale turbulent structures may deform the cutoff surface. The illumination microwave of MIR is scattered. MIR optical system makes an obscure image (because of low brightness) of the cutoff surface if the scattering is very strong and MIR can't collect most of the reflected power [1; 57]. As a result, the reflection power is rapidly changing, for example, the intense bursts shown in figure 6.1(e).

Figure 6.22 shows the schematic of the intermittency caused the scattering effect of one blob-like structure. If the scale of the turbulent structure is smaller than the size of the detector array and the radial displacement of the cutoff surface is large, the scattering effect becomes strong. As an example of intermittency, we select the MIR signals at $t = 30.2 \sim 30.6$ ms in shot #53441 (see Fig. 6.23 (a)). The arrangement of the detector array is shown in Fig. 2.4. This corresponds to the long-range correlation fluctuations. At $t \approx 30.35$ ms, a strong negative burst is observed in channel 1 and 2. It is not observed in channel 3 and 6. This suggests that a localized structure with small size (about 8 cm, $k > 40$ m^{-1}) appears at channel 1 and 2. This structure is radial elongated, which causes a strong negative burst in MIR signal. At $t = 30.45 \sim 30.6$ ms, similar fluctuations are observed in all the channels. This suggests that the fluctuation is dominated by the low k mode ($k < 21$ m^{-1}).

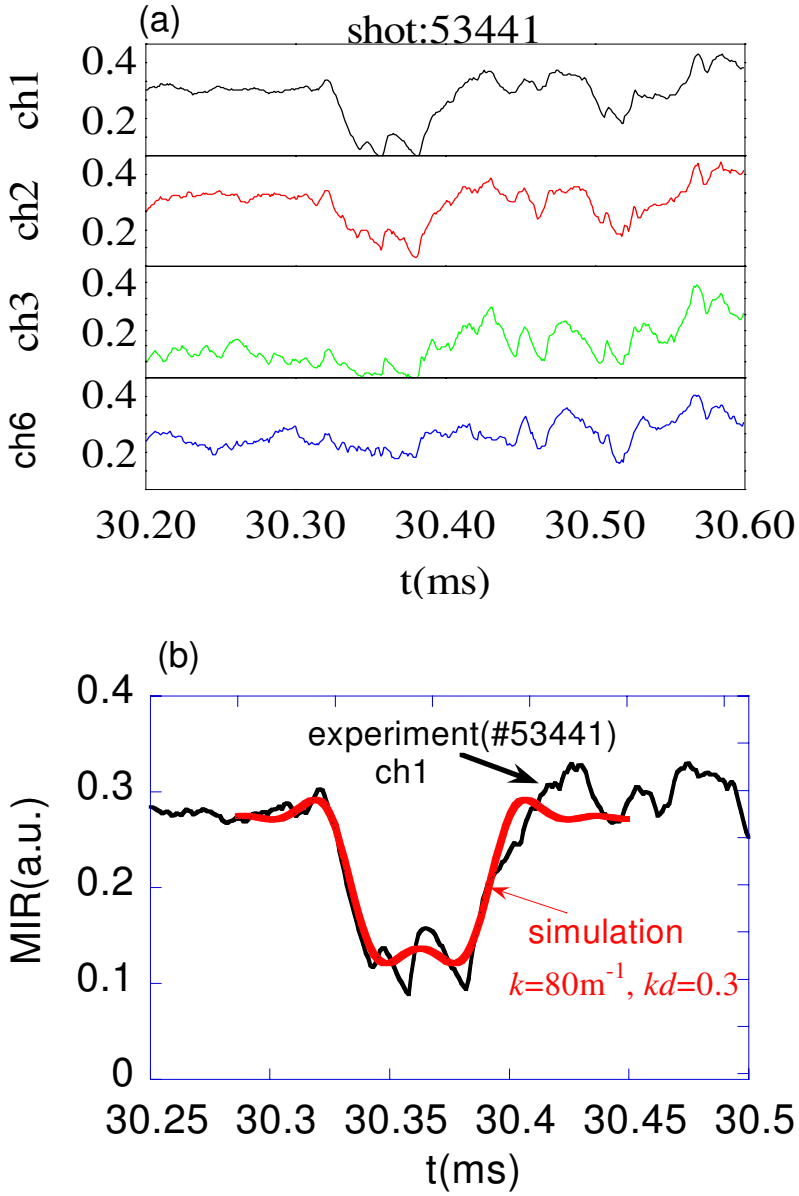

Figure 6.23: (a)Intermittency of the MIR signals, (b)Simulation of the intermittency caused by a blob-like structure ($k = 80$ m^{-1}, $d = \lambda_0/4 = 3.75$ mm). The arrangement of the detector array is shown in Fig. 2.4

In order to understand the intermittency further, we use the Huygens-Fresnel model to simulate the MIR signal. The detail of the model is explained in chapter 3. Here, we simulate the MIR signal at $t \approx 30.35$ ms in shot #53441. Assume the size of a blob-like structure is 7.8 cm on the cutoff surface, which corresponds to $k = 80$ m^{-1}. The radial displacement is $d = \lambda_0/4 = 3.75$ mm, where λ_0 is the wavelength of the microwave. The blob-like structure moves along the cutoff surface with the velocity of 3 kms^{-1}. The simulation result is shown in Fig. 6.23 (b) (red thick line). The simulation agrees with the experimental signal (ch1, #53441). Since the blob-like structure scatters the microwave power, the intermittency of MIR signal has the features of negative bursts.

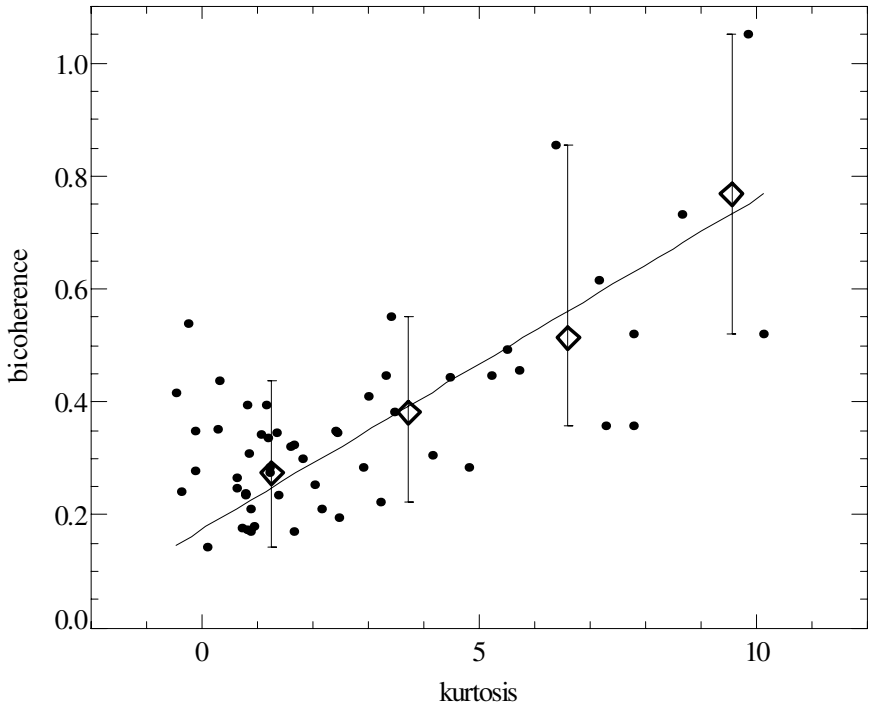

Figure 6.24: The total bicoherence as a function of kurtosis

The strong intermittency correspond to the high non-Gaussian tail. In this case, the kurtosis is increased. Figure 6.24 shows the total bicoherence among the modes $k_a = -1$, $k_a = 1$ and $k_a = 0$ as a function of kurtosis. The dots represent the experiments, and the line denotes their linear fitting. The total bicoherence is increased as the kurtosis is increased. It suggests that the nonlinear interaction contributes to the intermittent bursts of the turbulent structures.

The soft-x-ray (SXR) intensity can be used to characterize the plasma energy, since

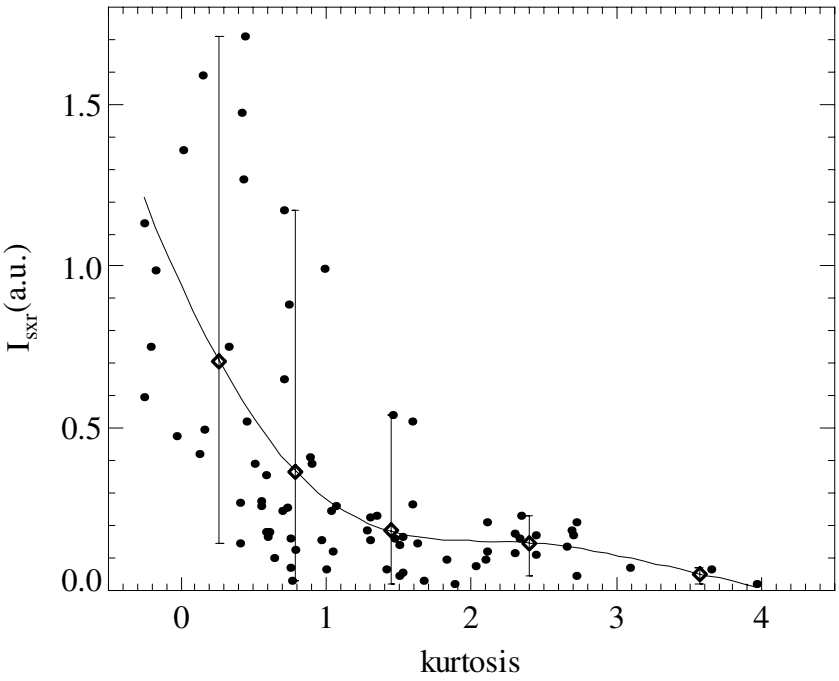

Figure 6.25: The soft-X-ray intensity versus the kurtosis

it is a function of the plasma density and temperature, as $I_{SXR} \propto n_e^{\alpha} T_e^{\beta}$ (assume Z_{eff} is constant), $\alpha \sim 2$ and $\beta \sim 2$ usually [85]. High SXR intensity denotes high plasma energy. Figure 6.25 shows the soft-x-ray (SXR) intensity as a function of kurtosis. The SXR is decreased as the kurtosis is increased. Since high kurtosis corresponds to high intermittency of the turbulence, the intermittency reduces the plasma confinement. Suppression of the intermittency can improve the confinement.

Figure 6.26 shows the skewness and kurtosis as a function of reversal parameter F. Here, the broken lines denote $S = K = 0$ which represent the Gaussian distribution. The filled squares represent PPCD plasma. The value of F is averaged at the same time range of bicoherence analysis. It should be noted that the operation of PPCD plasma is different from that of standard plasma. In PPCD operation, F is rapidly decreased due to the external driven field. In without PPCD operation, F is almost constant during the flattop of the discharge. The skewness and kurtosis have the low values at $F > -0.4$. However at $F < -0.4$, the skewness and kurtosis are suddenly increased. The high values of the skewness and kurtosis at $F < -0.4$ represent the high intermittency in no-PPCD plasma. This corresponds to the intermittent bursts in MIR signal. The high total bicoherence and high intermittency suggest that the turbulent structures are

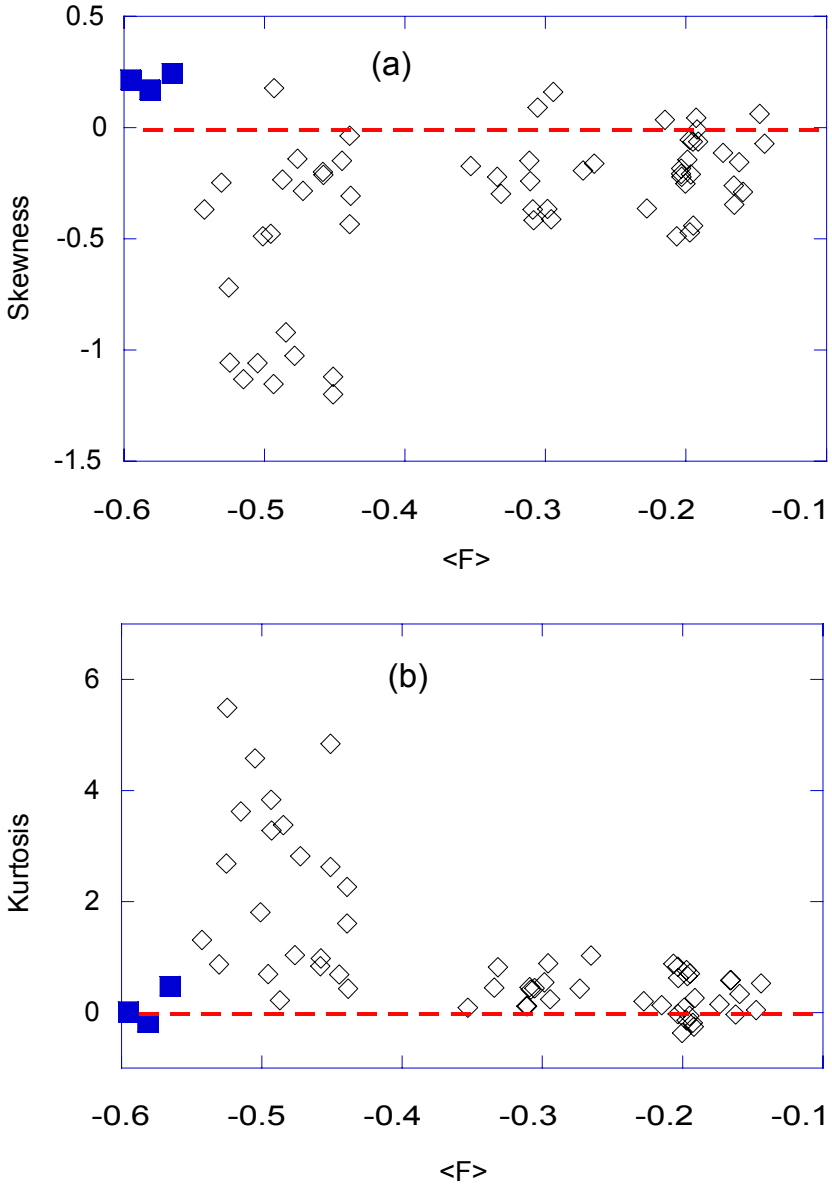

Figure 6.26: (a) skewness and (b) kurtosis as a function of F. The broken lines denote $S = K = 0$. The filled square represents the PPCD plasma.

intensely generated through nonlinear interactions. Although the total bicoherence is high at $F \approx -0.3$, the plasma is less intermittent. It suggests that $F \approx -0.4$ is the threshold for the intense generation of the turbulent structures.

Chapter 7

Summary and discussion

7.1 Summary of experimental results

This work presents the first measurement of the two-dimensional (2D) local density turbulence with microwave imaging reflectometry (MIR) in a reversed-field pinch (RFP) plasma. By using this system, 2D image of the density fluctuations around the reversal surface have been observed with the spatial resolution of 3.7 cm and the temporal resolution of 1μs.

In order to investigate the principles of MIR measurement, comparison between the simulation and a laboratory test of MIR system has been carried out. The numerical model based on the Huygens-Fresnel equation is used to simulate the fluctuations measured by MIR. In this test, we found that the phase ϕ corresponds to the displacement of the cutoff surface in the radial direction, and the amplitude A corresponds to the reflection power, which is modulated by the shape of the cutoff surface in MIR signal $A\exp(i\phi)$. The simulation agrees well with the test in the case of the weak fluctuation. In the case of the strong fluctuation, the amplitude signal is deformed, while the phase (IQ signals) is not deformed too much. The coherence length of the complex IQ signals is longer than that of the amplitude signals. From the simulation and laboratory test, MIR is valid with the condition $4k_{\perp}dL/D < 1$ to measure the motion of the cutoff surface, where, D is the diameter of the optical lens, L is the distance between the cutoff surface and the optical lens, $k_{\perp}$ and d are the perpendicular wavenumber and the

radial displacement of the fluctuation, respectively. The most measured fluctuations in TPE-RX distribute in the range of $4k_{\perp}dL/D < 0.8$.

The RFP turbulence measured by MIR around the field reversal surface in TPE-RX has been studied by comparing the plasmas with and without PPCD in this work. The features of the RFP turbulence are as follows:

(1) In the low k and low frequency ranges, MIR signals have high correlation with the magnetic fluctuations. Without PPCD operation, the $m = 0$ tearing modes (dynamo) are dominant. While in the PPCD plasma, the $m = 1$ tearing modes are dominant.

(2) In the high k and high frequency ranges, MIR signals have high correlation with the electrostatic fluctuations measured by Langmuir probe. The k spectrum of MIR is broad and shifted in the electron drift direction in the plasma without PPCD. The high nonlinear coupling between the high k modes and the low k modes is observed. While in PPCD plasma, the high k modes have not been observed.

(3) The intermittency is increased as the reversal parameter $\mid F \mid$ is increased in the case of without PPCD. Note that a deep $F(F = B_t(a)/ < B_t >)$ corresponds to a strong dynamo as the reversed toroidal magnetic field $B_t(a)$ is mainly sustained by the dynamo. The intermittency of MIR signal corresponds to the bursts in the negative direction, which has a small-scale structure with high fluctuation amplitude. Simulation of MIR signal suggests that the intermittency in MIR signal is caused by the blob-like structure, which scatters the reflection wave and leads to the rapid decrease of the reflection power (negative burst). In PPCD plasma, the intermittency is not observed and the confinement is improved as the soft-X-ray is increased by the factor of 100.

These results suggest that the high frequency fluctuations around the reversal surface in the plasma without PPCD have the features of electrostatic turbulence, while the low frequency fluctuations are the $m = 0, 1$ tearing modes. PPCD operation suppresses the m=0 tearing modes and turbulence, and the low frequency fluctuations are dominated the $m = 1$ modes.

In conclusion, this work is the first demonstration of MIR as the turbulence diagnostics. This is the first observation of the turbulence around the field reversal surface in RFP plasma. This work demonstrates how the dynamo and intermittent structures cause bad confinement.

7.2 Discussions

Various candidates for RFP turbulence have been discussed by numbers of authors [34–38]. The theories of the tearing instabilities, interchange instabilities and drift waves have been explained in chapter 1. Table 7.1 shows the possible candidates of the instabilities in RFP [34; 85; 86]. Present theories predict as follows: In RFP, the toroidal modenumbers ($m = 1$ modes) increase with radius. In the core region, the fluctuations are dominated by the long wavelength tearing instabilities, which become stable as the wavenumber k increases [34]. In the edge region, the interchange instabilities may become dominant due to their fast growth rate at high k. On the other hand, the interchange instabilities become electrostatic fluctuations for the small-scale fluctuations.

	Fluctuations	Stabilization	Driven force
Tearing modes	Magnetic: $\widetilde{B}$ Low k mode is dominant (core: m=1, edge: m=0), high k mode is stable.	Current profile	•Current gradient •Finite pressure effects (high β)
Micro-tearing modes	Magnetic and electrostatic $\widetilde{B}, \widetilde{\varphi}$ Short wavelength turbulence.	• $\eta_e = 0$ • Low collision • high collision	•∇T_e •Nonlinear effects
Resistive interchange modes	Magnetic, it becomes electrostatic at high k. $\widetilde{B}, \widetilde{n}, \widetilde{\varphi}$ Low k mode is dominant, high k mode tends to stable $\widetilde{n}/n = (\omega^*/\omega)(e\widetilde{\varphi}/T_e)$ at $k_\parallel^2 \upsilon_{T_e}^2 < \omega \nu_{ei}$ Phase difference of (n,φ) ≈ π/2 ~ π/4	•Good magnetic curvature (convex-toward: R<0) •Finite Larmor effect	•Pressure driven •Gradient B
Drift wave (η_i mode)	Electrostatic, $\widetilde{n}, \widetilde{\varphi}$ Short wavelength turbulence. $\widetilde{n}/n = e\widetilde{\varphi}/T_e$ at $k_\parallel^2 \upsilon_{T_e}^2 > \omega \nu_{ei}$ Phase difference of (n,φ) ≈ 0	•Shear flow •Finite β •Short connection length •Good magnetic curvature	Driven by η_i (low β)

Table 7.1: Candidates of the instabilities in RFP

In this work, MIR measures the density fluctuations around the reversal surface with $k \leq 85$ m^{-1} and $k\rho_i \leq 0.8$. The low frequency fluctuations in MIR signals should be the MHD mode because of the high correlation with magnetic fluctuations (see Fig. 6.15). For the high frequency fluctuation, there is no correlation between MIR and magnetic fluctuations (see Fig. 6.16). The high correlation between MIR and floating

potential supports the electrostatic turbulence in the MIR signal. Therefore, the drift waves and the high k interchange turbulence are the major candidates for the RFP turbulence around reversal surface. Here we will discuss which instability agrees with our experiment.

In the case of drift wave turbulence, the density fluctuation satisfies the approximation

$$\frac{\widetilde{n_e}}{n_e} \approx \frac{e\widetilde{\phi}}{T_e}(1-\varepsilon) \tag{7.1}$$

where, $\varepsilon \ll 1$. The small ε is due to the resistivity. The density perturbation ($\widetilde{n_e}$) is in phase with potential perturbation ($\widetilde{\phi}$) in the case of small ε. In the case of resistive interchange turbulence, the electrons behave isothermally

$$\frac{\widetilde{n_e}}{n_e} = \frac{\omega_*}{\omega}\frac{e\widetilde{\phi}}{T_e} \tag{7.2}$$

in the region of $k_\parallel^2 v_{T_e}^2 < \omega\nu_{ei}$. The fluctuations in $\widetilde{n_e}$ and $\widetilde{\phi}$ may have the phase of $\sim \pi/2$ due to the strong growth rate $\omega \simeq i\gamma$ [35]. In the weakly collisional limit, the phase difference is $\sim \pi/4$ [86].

As shown in Fig. 6.16, the phase difference between density and potential fluctuations is small ($< \pi/4$). The phase difference increases as the radial distance decreases. However, MIR and electrostatic probe measure at difference positions, and their radial distance is large. It is impossible to estimate the real phase difference near the cutoff surface from present experimental results.

Another method to compare the drift wave and interchange turbulence is the eigenfrequency and the propagation direction of the fluctuations. Theoretically, both the ideal tearing and interchange instabilities only have the purely growing. They don't have the real eigenfrequency. However, in the experiment, the low frequency ($f \sim 10$ kHz) MHD modes are often observed. It may be caused by the plasma rotation which is $v < 10$ kms^{-1} observed in TPE-RX [87; 88]. The drift wave has the diamagnetic frequency in the electron drift direction (The drift wave in the ion drift direction has very low frequency $\omega \to 0$.). The diamagnetic frequency is given by

$$\omega_* = -k_\perp \frac{\kappa T_e}{e n_e B_0}\frac{dn_e}{dr} \tag{7.3}$$

Since the magnetic field is mainly poloidal near the reversal surface, the perpendicular wavenumber $k_\perp$ should be the toroidal wavenumber k_φ.

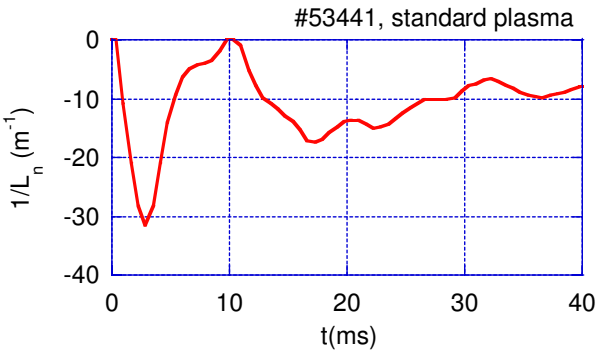

Figure 7.1: Time evolution of L_n^{-1} in shot #53441 (standard plasma, $F = -0.5$)

In TPE-RX, the magnetic field is about ~ 0.1 Tesla. The inverse density gradient length $L_n^{-1} = (dn_e/dr)/n_e$ is estimated about $(2 \sim 10)/a$ (minor radius $a = 0.45$ m) because of the high density gradient around the reversal surface. Figure 7.1 shows the time evolution of L_n^{-1} at the cutoff density ($n_e = 0.5 \times 10^{19}$ m^{-3}, $r_{cut} = 0.8$) in a standard plasma (shot #53441, $F = -0.5$). $L_n = 10 \sim 15$ m^{-1} during the flattop of the plasma ($t = 15 \sim 30$ ms). Assume $T_e = T_e(0)(1 - r^2)$ and $T_e(0) = 300$ eV, the electron temperature is about 100 eV around the cutoff $r_{cut} = 0.8$. In this measurement, we have the waves of $n = 73 \pm 37$ ($k_\varphi = 42 \pm 21$ m^{-1}). The estimated frequency is in the range of $30 \sim 150$ kHz. It is consistent with the experimental results (see Fig. 6.17). The MEM analysis gives the turbulence propagates in the electron drift direction (see Fig. 6.12 (a)). These results suggest that high frequency fluctuations observed by MIR have the features of drift wave turbulence.

However, the RFP plasma has high β and high magnetic fluctuations. The drift wave turbulence has high wavenumber, and it is valid for the low-β plasma. In this work, the k range of MIR system is $k \leq 85$ m^{-1}. The fluctuations measured by MIR are dominated by the low k modes, and the fluctuation energy decreases as the k increases. The high intermittency and the strong magnetic fluctuations suggest that the turbulence measured by MIR is affected by MHD fluctuations. So the possible candidate of the electrostatic turbulence around the reversal surface is the high k interchange turbulence. The features of the drift wave in the interchange modes may be caused by the two-fluid instabilities for electrons and ions. Therefore, the interchange effects and drift wave effects must be considered in the theoretical models.

The nonlinear coupling between the high k (or n) electrostatic turbulence and the

low n MHD modes has been studied in this work. In RFP plasma (without PPCD), the dynamo is a global phenomenon which corresponds to the $m = 0$ (usually low n) tearing modes. Without PPCD plasma, the $m = 0$ tearing modes is dominated (see Fig. 6.11). This may be as a result of strong dynamo effect. The high nonlinear coupling between the high k electrostatic-like turbulence and the low k MHD modes implies the existence of strong correlation between the electrostatic turbulence and the dynamo effect. The high intermittency and the high nonlinear coupling support this results (see Fig. 6.20). The high intermittency at the deep F plasma is expected to be partly driven by the nonlinear interaction between electrostatic-like turbulences. Simulation of the MIR signal suggests the intermittent structure may be due to the amplification effect of the initial perturbation by interchange instabilities, which enhance the transport and decrease the confinement.

In a PPCD plasma, the turbulence and dynamo ($m = 0$ modes) are suppressed, and the $m = 1$ modes are dominant (see Fig. 6.10, 6.15 and 5.6). The observed low frequency fluctuations (see Fig. 6.1) are the $m = 1$ modes. Since the PPCD plasma has high confinement, the MHD modes may be enhanced by the high pressure gradient.

Interpretations of the turbulence measured by MIR are as follows: (1) Present experiments support the electrostatic turbulence with the features of drift wave turbulence is dominant near the reversal surface. (2) Suppressing the $m = 0$ tearing mode activity and the reduction of the electrostatic turbulence in the PPCD plasma are related . (3) The strong nonlinear coupling between the high k electrostatic turbulence and the low k MHD modes suggests that the electrostatic turbulence correlates to the sustainment of the RFP configuration (dynamo) through nonlinear interaction.

In this work, although the 2D turbulence in the plasmas with and without PPCD has been measured by MIR, the spatial resolution of the observed waves is poor. The observed spatial waves include many modes. On the other hand, the signal to noise ratio (SNR) is not very high. To measure the fine structures of the turbulence, the high sensitive detector array with big size and high spatial resolution (< 1 cm) should be developed.

References

[1] E. Mazzucato. Microwave reflectometry for magnetically confined plasmas. *Rev. Sci. Instrum.*, **69**, 2201 (1998). 2, 5, 6, 37, 38, 41, 93, 125

[2] H. Park. Recent advancements in microwave imaging plasma diagnostics. *Rev. Sci. Instrum.*, **74**, 4239 (2003). 2, 3, 5, 37, 38

[3] H. A. B. Bodion. The reversed field pinch. *Nucl. Fusion*, **30**, 1717 (1990). 2, 6, 8, 9, 91

[4] V. Antoni et al. Electrostatic turbulence and transport in the velocity shear layer of a reversed field pinch plasma. *Phys. Rev. lett.*, **80**, 4185 (1998). 2, 28, 116

[5] J. S. Sarff et al. Fluctuation and transport reduction in a reversed field pinch by inductive poloidal current drive. *Phys. Rev. lett.*, **72**, 3670 (1994). 2, 9, 10, 94

[6] C. Laviron et al. Reflectometry techniques for density profile measurements on fusion plasmas. *Plasma Phys. Control. Fusion*, **38**, 905 (2008). 2

[7] R. Nazikian et al. A tutorialon the basic principles of mictrowave reflectometer applied to fluctuation measurements in fusion plasmas. *Phys. Plasmas*, **8**, 1840 (2001).

[8] N. Bretz. One-dimensional modeling of the wavelength sensitivity, localization, and correlation in reflectometry measurements of plasma fluctuations. *Phys. Fluids B*, **4**, 2414 (1992).

[9] R. Sabot et al. Recent results on turbulence and MHD activity achieved by reflectometry. *Plasma Phys. Control. Fusion*, **48**, B421–B432 (2006). 2, 37

[10] G D. Conway et al. Microwave reflectometry for fusion plasma diagnosis. *Nucl. Fusion*, **46**, S665 (2006). 5, 37

[11] S. Yamaguchi et al. Microwave imaging reflectometry in LHD. *Rev. Sci. Instrum.*, **77**, 10E930 (2006). 5, 38

[12] T. Munsat et al. Laboratory characterization of an imaging reflectometer system. *Plasma Phys. Control. Fusion*, **45**, 469 (2003). 5, 38, 58

[13] G.J. Kramer et al. Simiulation of optical and synthetic imaging using microwave reflectometry. *Plasma Phys. Control. Fusion*, **46**, 695 (2004).

[14] M. Ignatenko et al. Numerical study of microwave imaging reflectometry for measurements of density fluctuations in a tandem mirror plasma. *Nucl. Fusion*, **46**, S760 (2006). 5, 38, 58

[15] E. Mazzucato et al. Fluctuation measurements in tokamaks with microwave imaging reflectometry. *Phys. Plasmas*, **9**, 1955 (2002). 5, 38, 53

[16] S. Yamaguchi et al. Observation of MHD mode with multi-harmonics by using microwave imaging reflectometry in LHD. *proceedings of ITC/ISHW2007*, **P1**, 082 (2007). 5

[17] T. L. Rhodes et al. Signal amplitude effects on reflectometer studies of density turbulence in tokamaks. *Plasma Phys. Control. Fusion*, **40**, 493 (1998). 6

[18] G D. Conway et al. Comparison of reflectometer fluctuation measurements from experiment and two-dimensional numerical simulation. *Rev. Sci. Instrum.*, **67**, 3861 (1996). 6, 117

[19] J. Schirmer et al. Radial correlation length measurements on ASDEX Upgrade using correlation Doppler reflectometry. *Plasma Phys. Control. Fusion*, **49**, 1019 (2007). 6, 53

[20] S. C. Prager. Reversed field pinch:recent results. *Plasma Phys. Control. Fusion*, **34**, 1985 (1992). 6

[21] Thomas R Jarboe. Review of spheromak research. *Plasma Phys. Control. Fusion*, **36**, 945 (1994). 6

[22] J. B. Taylor. Relaxation and magnetic reconnection in plasmas. *Rev. Mod. Phys.*, **58**, 741 (1986). 8, 9

[23] Dieter Biskamp. *Nonlinear Magnetohydrodynamics*. Cambridge University Press, Cambridge University, United Kingdom, first edition, 1999. 8, 9, 13, 28

[24] P R. Brunsell. Edge plasma fluctuations and transport in a reversed-field pinch. *Phys. plasmas*, **1**, 2297 (1994). 8, 73

[25] S. Assadi et al. Measurement of nonlinear mode coupling of tearing fluctuations. *Phys. Rev. lett.*, **69**, 281 (1992). 9, 15

[26] T. G. Cowlling et al. The present status of dynamo theory. *Ann. Rev. of Astron. and Astrop.*, **19**, 115–135 (1981). 9

[27] Eric G. Blackman et al. Laboratory plasma dynamos, astrophysical dynamos and magnetic helicity evolution. *Mon. Not. R. Astron. Soc.*, **369**, 1837 (2006).

[28] H. Ji et al. The alfa dynamo effects in laboratory plasmas. *Magnetohydrodynamics*, **38**, 191 (2002). 94

[29] P W. Fontana et al. Spectroscopic observation of fluctuation induced dynamo in the edge of the reversed field pinch. *Phys. Rev. lett.*, **85**, 566 (2000). 9, 15, 88

[30] Y. Yagi et al. Improved confinement in the TPE-RX RFP by means of the PPCD. *Plasma Phys. Control. Fusion*, **44**, 335 (2002). 9, 10, 21, 32

[31] R. Bartiromo et al. Core transport improvement during pulsed poloidal current drive in the RFX reversed-field pinch. *Phys. Rev. lett.*, **82**, 1462 (1999). 9, 10

[32] H. Ji et al. Fluctuation and edge-current sustainment in a reversed-field pinch. *Phys. Rev. lett.*, **69**, 616 (1992). 9

[33] B.E. Chapman et al. Reduced edge instability and improved confinement in the MST reversed field pinch. *Phys. Rev. lett.*, **87**, 205001 (2001). 11

[34] Dieter Biskamp. *Magnetic reconnection in plasmas*. Cambridge University Press, Cambridge University, United Kingdom, first edition, 2000. 11, 12, 133

[35] F. Ebrahimi et al. Resistive-ideal transition of pressure-driven instabilities in current-carrying plasmas beyond the Suydam criterion. *Phys. Plasmas*, **9**, 2470 (2002). 12, 13, 134

[36] J. A. Holmes et al. Nonlinear dynamics of tearing modes in the reversed field pinch. *Phys. Fluids*, **31**, 1166 (1988). 13

[37] Jeffrey P. Freidberg. *Ideal Magnetiohydrodynamics*. Plenum Press, London UK, first edition, 1987.

[38] M. G. Rusbridge et al. *Plasma. Phys.*, **19**, 499 (1977). 11, 133

[39] Robert J Goldston. *Introduction to plasma physics*. Institute of Physics Publishing, Techno House, Redcliffe Way, Bristol BS1 6NX, UK, first edition, 1995. 15

[40] H. Ji et al. Measurement of the dynamo effect in a plasma. *Phys. Plasmas*, **3**, 1935 (1996). 15, 93

[41] R. Cavazzana et al. Investigation of plasma edge turbulence using a gas-puff imaging system in the reversed-field pinch device TPE-RX. *Plasma Phys. Control. Fusion*, **49**, 129 (2007). 61, 93, 107

[42] G.X. Li et al. Correlation between internal tearing modes and edge electrostatic fluctuations in a reversed-field pinch. *Phys. Plasmas*, **2**, 2615 (1996). 17

[43] M. Agostini et al. Electrostatic turbulence in the edge of TPE-RX and driving mechanisms. *Plasma Phys. Control. Fusion*, **50**, 095004 (2008).

[44] L. Frassinetti et al. Improved particle confinement in transition from multiple-helicity to qusi-single-helicity regimes of a reversed-field pinch. *Phys. Rev. lett.*, **97**, 175001 (2006).

[45] P R. Brunsell. Coherent magnetic field fluctuations and locked modes in a reversed-field pinch. *Phys. Fluids B*, **5**, 885 (1993). 15, 88, 91

[46] T.D. Rempel et al. Edge electrostatic fluctuations and transport in a reversed field pinch. *Phys. Rev. Lett.*, **67**, 1438 (1991). 17, 110

[47] H. Ji et al. Fluctuation and electron heat transport in a reversed-field pinch. *Phys. Rev. lett.*, **67**, 62 (1991). 17

[48] V. Antoni et al. Edge physics in reversed-field pinch and tokamak: similarities and differences. *Plasma Phys. Control. Fusion*, **39**, B223 (1997). 17, 110

[49] Y. Yagi et al. Design concept and confinement prediction of TPE-RX reversed-field pinch device. *Fusion Eng. Des.*, **45**, 409 (1999). 21

[50] L. Frassinetti et al. Performance improvement conditions and their physical origin in the pulsed poloidal current drive regime of the reversed-field pinch device TPE-RX. *Phys. Plasmas*, **11**, 5229 (2004). 21, 31

[51] L. Frassinetti et al. Turbulence and particle confinement in a reversed-field pinch plasma. *Plasma Phys. Control. Fusion*, **49**, 199–209 (2007). 21, 22

[52] Y. Nagayama et al. Development of MIR in TPE-RX. *Plasma and Fusion Res.*, **3**, 053 (2008). 22, 24, 28, 96

[53] Y. Yagi et al. Extensive magnetic measurement system in TEP-RX. *Fusion Eng. Des.*, **46**, 47 (1999). 22, 107

[54] K. Yambe et al. Measurement of fast magnetic fluctuations in eldge region of TPE-RX reversed-field pinch plasma. *Jpn. J. Appl. Phys.*, **46**, 6831–6833 (2007). 22, 96

[55] H. Koguchi et al. High beta and high density operation in TPE-RX. *Plasma and Fusion Res.*, **4**, 022 (2009). 31, 32

[56] A. Ejiri et al. The response of microwave reflectometry under generalized configuration. *Plasma Phys. Control. Fusion*, **50**, 065003 (2008). 34, 37, 38

[57] Z. B. Shi et al. 2D numerical simulation of MIR. *J. Plasma and Fusion Res., 14th International Congress on Plasma Physics* (2008). 34, 117, 125

[58] T. Estrada et al. Turbulence and beam size effects on reflectometry measurements. *Phys. Plasmas*, **8**, 2657 (2001). 37, 53

[59] Y. Lin et al. Plasma curvature effects on microwave reflectometry fluctuation measurements. *Plasma Phys. Control. Fusion*, **43**, L1 (2001). 38, 39

[60] D. Kuwahara et al. Development of 2D antenna array for microwave imaging reflectometry in LHD. *J. Plasma and Fusion Res., 14th International Congress on Plasma Physics* (2008). 47

[61] E.B. Hooper et al. Correlation techniques in experimental plasma physics. *Plasma Phys.*, **13**, 1 (1971). 63

[62] Ch P. Ritz et al. Advanced plasma fluctuation analysis techniques and their impact on fusion research. *Rev. Sci. Instrum.*, **59**, 1739 (1988). 68, 80

[63] G. S. Xu et al. Multiscale coherent structures in tokamak plasma turbulence. *Phys. Plasmas*, **13**, 102509 (2006). 63

[64] V. P. Budaev et al. The effect of the rotating helical fields on the plasma edge in the Hybtok-II tokamak. *Nucl. Fusion*, **46**, 561 (2006). 68

[65] C. Torrence et al. A practical guid to wavelet analysis. *Bulletin of the American Meteorological Society*, **76**, 61 (1998). 73

[66] D. Maraun et al. Cross wavelet analysis: significance testing and pitfalls. *Nonlinear Processes in Geophysics*, **11**, 505 (2004). 68, 72

[67] D. S. Bloomfield et al. Wavelet phase coherence analysis: application to a quiet-sun magnetic element. *The Astrophysical Journal*, **617**, 623 (2004). 72

[68] Y. Hirano et al. Improved confinement in a high pinch parameter region of the reversed field pinch plasma. *Nucl. Fusion*, **36**, 721 (1996). 73, 88, 91

[69] Z. B. Shi et al. MEM analysis of the 2D density fluctutation by MIR in TPE-RX. *Plasma and Fusion Res., proceedings of 18th International Toki Conference* (2008). 79, 110

[70] Jae S. Lim et al. A new algorithm for two-dimensional maximum entropy power spectrum estimation. *IEEE trans. on acoustics, speech, and signal proc.*, **Assp-29**, 401 (1981). 85

[71] C. Michael et al. Interpretation of Line-Integrated Signals from 2-D Phase Contrast Imaging on LHD. *Plasma and Fusion Res.*, **2**, S1034 (2007). 87

[72] K. Tanaka et al. Two-dimensional phase contrast imaging for local turbulence measurements in large helical device. *Rev. Sci. Instrum.*, **79**, 10E702 (2009). 85

[73] J. Skilling et al. Maximum entropy image reconstruction: general algorithm. *Mon. Not. R. astr. Soc.*, **211**, 111 (1984). 85, 110

[74] C. Michael et al. Detection of high k turbulence using two dimensional phase contrast imaging on LHD. *Rev. Sci. Instrum.*, **79**, 10E724 (2008). 87

[75] H. Ji et al. Time-resolved observation of discrete and continuous magnetohydrodynamic dynamo in the reversed field pinch edge. *Phys. Rev. lett.*, **73**, 668 (1994). 88, 93

[76] Dieter Biskamp. *Magnetohydrodynamic turbulence*. Cambridge University Press, Cambridge University, United Kingdom, first edition, 2003. 93

[77] Marcel Lesieur. *Turbulence in Fluids*. Kluwer Academic Publishers, P.O.Box 17, 3300 AA Dordrecht, Netherlands, third edition, 1997. 93

[78] Z. B. Shi et al. Observation of the Turbulent Structures Generation in RFP Plasma by Microwave Imaging Reflectometry in TPE-RX. *submitted to Phys. Rev. lett.* (2009). 94

[79] A. Fujisawa et al. A review of zonal flow experiments. *Nucl. Fusion*, **49**, 013001 (2009). 99

[80] Z. B. Shi et al. Data analysis techniques for microwave imaging reflectometry. *Plasma and Fusion Res.*, **3**, S1045 (2008). 99, 104, 119

[81] Y. H. Xu et al. On the properties of turbulence intermittency in the boundary of the TEXTOR tokamak. *Plasma Phys. Control. Fusion*, **47**, 1841 (2005). 101

[82] L. W. Yan et al. Three-dimensional features of GAM zonal flows in the HL-2A. *Nuclear Fusion*, **47**, 1673–1681 (2007). 101

[83] B. J. Carreras et al. Characterization of the frequency ranges of the plasma edge fluctuation spectra. *Phys. Plasmas*, **6**, 4615 (1999). 104

[84] B. Ph. van. Milligen et al. Nonlinear phenomena and intermittency in plasma turbulence. *Phys. Rev. lett.*, **74**, 395 (1995). 119, 122

[85] John Wesson. *Tokamaks*. Oxford, London UK, third edition, 2004. 128, 133

[86] H. Sugama et al. Study of resistive drift and resistive interchange modes in a cylindrical plasma with magnetic shear. *Phys. Fluids*, **31**, 1601 (1988). 133, 134

[87] H. Sakakita et al. The first plasma rotation measurement in a large reversed-field pinch device, TPE-RX. *J. Phys. Soc. Jpn.*, **69**, 635 (2000). 134

[88] N. Ohno et al. Low frequency fluctuations near relaxed state of reversed field pinch in the presence of stationary plasma flow. *J. Phys. Soc. Jpn.*, **70**, 988 (2001). 134